

1 PREPARED FOR SUBMISSION TO JINST

2 Design, construction and operation of the ProtoDUNE-SP 3 Liquid Argon TPC

4 The DUNE Collaboration

5 A. Abed Abud^{125 25} B. Abi¹⁵¹ R. Acciarri⁶⁵ M. A. Acero¹¹ M. R. Adames¹⁸⁵ G. Adamov⁷⁰
6 D. Adams²¹ M. Adinolfi²⁰ A. Aduszkiewicz⁷⁹ J. Aguilar¹²⁴ Z. Ahmad¹⁹⁷ J. Ahmed²⁰⁰
7 B. Ali-Mohammadzadeh^{85 37} T. Alion¹⁸³ K. Allison⁴⁴ S. Alonso Monsalve^{25 57} M. Alrashed¹¹⁸
8 C. Alt⁵⁷ A. Alton¹² P. Amedo⁸³ J. Anderson⁷ C. Andreopoulos^{170 125} M. Andreotti^{86 66}
9 M. P. Andrews⁶⁵ F. Andrianala⁵ S. Andringa¹²² N. Anfimov¹¹⁰ A. Ankowski¹⁷¹
10 M. Antoniaassi¹⁸⁵ M. Antonova⁸² A. Antoshkin¹¹⁰ S. Antusch¹⁴ A. Aranda-Fernandez⁴³
11 A. Ariga¹⁵ L. O. Arnold⁴⁶ M. A. Arroyave⁵⁶ J. Asaadi¹⁸⁹ L. Asquith¹⁸³ A. Aurisano⁴¹
12 V. Aushev¹²¹ D. Autiero⁹⁶ M. Ayala-Torres⁴² F. Azfar¹⁵¹ A. Back¹⁰⁴ H. Back¹⁵² J. J. Back²⁰⁰
13 C. Backhouse¹⁹⁵ P. Baesso²⁰ I. Bagaturia⁷⁰ L. Bagby⁶⁵ N. Balashov¹¹⁰ S. Balasubramanian⁶⁵
14 P. Baldi³⁰ B. Baller⁶⁵ B. Bambah⁸⁰ F. Barao^{122 98} G. Barenboim⁸² G. J. Barker²⁰⁰
15 W. Barkhouse¹⁴⁴ C. Barnes¹³⁴ G. Barr¹⁵¹ J. Barranco Monarca⁷⁵ A. Barros¹⁸⁵ N. Barros^{122 59}
16 J. L. Barrow^{186 65} A. Basharina-Freshville¹⁹⁵ A. Bashyal¹⁵⁰ V. Basque¹³⁰ E. Belchior³⁶
17 J.B.R. Battat²⁰¹ F. Battisti¹⁵¹ F. Bay⁴ J. L. Bazo Alba¹⁶² J. F. Beacom¹⁴⁹ E. Bechetoille⁹⁶
18 B. Behera⁴⁵ L. Bellantoni⁶⁵ G. Bellettini¹⁶⁰ V. Bellini^{85 37} O. Beltramello²⁵ D. Belver²⁶
19 N. Benekos²⁵ C. Benitez Montiel⁹ F. Bento Neves¹²² J. Berger⁴⁵ S. Berkman⁶⁵
20 P. Bernardini^{88 173} R. M. Berner¹⁵ H. Berns²⁹ S. Bertolucci^{84 18} M. Betancourt⁶⁵ A. Betancur
21 Rodríguez⁵⁶ A. Bevan¹⁶⁵ T.J.C. Bezerra¹⁸³ M. Bhattacharjee¹⁰² S. Bhuller²⁰ B. Bhuyan¹⁰²
22 S. Biagi⁹⁴ J. Bian³⁰ M. Biassoni⁸⁹ K. Biery⁶⁵ B. Bilki^{16 107} M. Bishai²¹ A. Bitadze¹³⁰
23 A. Blake¹²³ F. D. M. Blaszczyk⁶⁵ G. C. Blazey¹⁴⁵ E. Blucher³⁹ J. Boissevain¹²⁶ S. Bolognesi²⁴
24 T. Bolton¹¹⁸ L. Bomben^{89 106} M. Bonesini^{89 136} M. Bongrand¹⁵⁴ F. Bonini²¹ A. Booth¹⁶⁵
25 C. Booth¹⁷⁶ F. Boran¹⁶ S. Bordini²⁵ A. Borkum¹⁸³ T. Boschi⁵⁵ N. Bostan^{107 147} P. Bour⁴⁸
26 C. Bourgeois¹⁵⁴ S. B. Boyd²⁰⁰ D. Boyden¹⁴⁵ J. Bracinik¹⁷ D. Braga⁶⁵ D. Brailsford¹²³
27 A. Branca⁸⁹ A. Brandt¹⁸⁹ J. Bremer²⁵ C. Brew¹⁷⁰ E. Brianne¹³⁰ S. J. Brice⁶⁵ C. Brizzolari^{89 136}
28 C. Bromberg¹³⁵ G. Brooijmans⁴⁶ J. Brooke²⁰ A. Bross⁶⁵ G. Brunetti^{89 136} M. Brunetti²⁰⁰
29 N. Buchanan⁴⁵ H. Budd¹⁶⁷ I. Butorov¹¹⁰ I. Cagnoli^{84 18} D. Caiulo⁹⁶ R. Calabrese^{86 66}
30 P. Calafiura¹²⁴ J. Calcutt¹³⁵ M. Calin²² S. Calvez⁴⁵ E. Calvo²⁶ A. Caminata⁸⁷ M. Campanelli¹⁹⁵
31 K. Cankocak¹⁰⁷ D. Caratelli⁶⁵ G. Carini²¹ B. Carlus⁹⁶ M. F. Carneiro²¹ P. Carniti⁸⁹ I. Caro
32 Terrazas⁴⁵ H. Carranza¹⁸⁹ T. Carroll²⁰⁴ J. F. Casta⁶ A. Castillo¹⁷⁵ C. Castromonte¹⁰⁵
33 E. Catano-Mur²⁰³ C. Cattadori⁸⁹ F. Cavalier¹⁵⁴ F. Cavanna⁶⁵ S. Centro¹⁵³ G. Cerati⁶⁵
34 A. Cervelli⁸⁴ A. Cervera Villanueva⁸² M. Chalifour²⁵ A. Chappell²⁰⁰ E. Chardonnet¹⁵⁵
35 N. Charitonidis²⁵ A. Chatterjee¹⁶¹ S. Chattopadhyay¹⁹⁷ H. Chen²¹ K. Chen²¹ M. Chen³⁰
36 Y. Chen¹⁵ Z. Chen¹⁸¹ Y. Cheon¹⁹³ D. Cherdack⁷⁹ C. Chi⁴⁶ S. Childress⁶⁵ A. Chiriacescu²²
37 G. Chisnall¹⁸³ K. Cho¹¹⁶ S. Choate¹⁴⁵ D. Chokheli⁷⁰ P. S. Chong¹⁵⁷ S. Choubey⁷⁶

38 A. Christensen⁴⁵ D. Christian⁶⁵ G. Christodoulou²⁵ A. Chukanov¹¹⁰ M. Chung¹⁹³
39 E. Church¹⁵² V. Cicero^{84 18} P. Clarke⁵⁸ T. E. Coan¹⁸⁰ A. G. Cocco⁹¹ J. A. B. Coelho¹⁵⁵
40 E. Conley⁵⁴ R. Conley¹⁷¹ J. M. Conrad¹³¹ M. Convery¹⁷¹ S. Copello⁸⁷ L. Corwin¹⁷⁷
41 R. Valentim¹⁹⁴ L. Cremaldi¹⁴⁰ L. Cremonesi¹⁶⁵ J. I. Crespo-Anadón²⁶ M. Crisler⁶⁵
42 E. Cristaldo⁹ R. Cross¹²³ A. Cudd⁴⁴ C. Cuesta²⁶ Y. Cui³² D. Cussans²⁰ M. Dabrowski²¹
43 O. Dalager³⁰ H. da Motta²³ L. Da Silva Peres⁶⁴ C. David^{207 65} Q. David⁹⁶ G. S. Davies¹⁴⁰
44 S. Davini⁸⁷ J. Dawson¹⁵⁵ K. De¹⁸⁹ R. M. De Almeida⁶⁸ P. Debbins¹⁰⁷ I. De Bonis⁵¹
45 M. P. Decowski^{143 3} A. de Gouvêa¹⁴⁶ P. C. De Holanda³⁶ I. L. De Icaza Astiz¹⁸³ A. Deisting¹⁶⁸
46 P. De Jong^{143 3} A. Delbart²⁴ D. Delepine⁷⁵ M. Delgado⁶ A. Dell'Acqua²⁵ P. De Lurgio⁷
47 J. R. T. de Mello Neto⁶⁴ D. M. DeMuth¹⁹⁶ S. Dennis³⁵ C. Densham¹⁷⁰ G. W. Deptuch²¹ A. De
48 Roeck²⁵ V. De Romeri⁸² G. De Souza³⁶ R. Devi¹¹¹ R. Dharmapalan⁷⁸ M. Dias¹⁹⁴ F. Diaz¹⁶²
49 J. S. Díaz¹⁰⁴ S. Di Domizio^{87 69} L. Di Giulio²⁵ P. Ding⁶⁵ L. Di Noto^{87 69} C. Distefano⁹⁴
50 R. Diurba¹³⁹ M. Diwan²¹ Z. Djurcic⁷ D. Doering¹⁷¹ S. Dolan²⁵ F. Dolek¹⁶ M. J. Dolinski⁵³
51 L. Domine¹⁷¹ D. Douglas¹³⁵ D. Douillet¹⁵⁴ G. Drake⁶⁵ F. Drielsma¹⁷¹ L. Duarte¹⁹⁴
52 D. Duchesneau⁵¹ K. Duffy⁶⁵ P. Dunne¹⁰¹ T. Durkin¹⁷⁰ H. Duyang¹⁷⁹ O. Dvornikov⁷⁸
53 D. A. Dwyer¹²⁴ A. S. Dyshkant¹⁴⁵ M. Eads¹⁴⁵ A. Earle¹⁸³ D. Edmunds¹³⁵ J. Eisch¹⁰⁸
54 L. Emberger^{130 132} S. Emery²⁴ A. Ereditato²⁰⁵ T. Erjavec²⁹ C. O. Escobar⁶⁵ G. Eurin²⁴
55 J. J. Evans¹³⁰ E. Ewart¹⁰⁴ A. C. Ezeribe¹⁷⁶ K. Fahey⁶⁵ A. Falcone^{89 136} M. Fani¹²⁶
56 C. Farnese⁹² Y. Farzan⁹⁷ D. Fedoseev¹¹⁰ J. Felix⁷⁵ Y. Feng¹⁰⁸ E. Fernandez-Martinez¹²⁹
57 P. Fernandez Menendez⁸² M. Fernandez Morales⁸³ F. Ferraro^{87 69} L. Fields¹⁴⁷ P. Filip⁴⁷
58 F. Filthaut^{143 166} A. Fiorentini¹⁷⁷ M. Fiorini^{86 66} R. S. Fitzpatrick¹³⁴ W. Flanagan⁵⁰
59 B. Fleming²⁰⁵ R. Flight¹⁶⁷ D. V. Forero¹³³ J. Fowler⁵⁴ W. Fox¹⁰⁴ J. Franc⁴⁸ K. Francis¹⁴⁵
60 D. Franco²⁰⁵ J. Freeman⁶⁵ J. Freestone¹³⁰ J. Fried²¹ A. Friedland¹⁷¹ F. Fuentes Robayo²⁰
61 S. Fuess⁶⁵ I. Furic⁶⁷ A. P. Furmanski¹³⁹ A. Gabrielli⁸⁴ A. Gago¹⁶² H. Gallagher¹⁹² A. Gallas¹⁵⁴
62 A. Gallego-Ros²⁶ N. Gallice^{90 137} V. Galymov⁹⁶ E. Gamberini²⁵ T. Gamble¹⁷⁶ F. Ganacim¹⁸⁵
63 R. Gandhi⁷⁶ R. Gandrajula¹³⁵ F. Gao¹⁶¹ S. Gao²¹ A. C. Garcia B.³⁶ D. Garcia-Gamez⁷³
64 M. Á. García-Peris⁸² S. Gardiner⁶⁵ D. Gastler¹⁹ J. Gauvreau¹⁴⁸ G. Ge⁴⁶ B. Gelli³⁶ A. Gendotti⁵⁷
65 S. Gent¹⁷⁸ Z. Ghorbani-Moghaddam⁸⁷ P. Giammaria³⁶ T. Giammaria^{86 66} D. Gibin¹⁵³
66 I. Gil-Botella²⁶ S. Gilligan¹⁵⁰ C. Girerd⁹⁶ A. K. Giri¹⁰³ D. Gnani¹²⁴ O. Gogota¹²¹ M. Gold¹⁴¹
67 S. Gollapinni¹²⁶ K. Gollwitzer⁶⁵ R. A. Gomes⁶¹ L. V. Gomez Bermeo¹⁷⁵ L. S. Gomez
68 Fajardo¹⁷⁵ F. Gonnella¹⁷ J. A. Gonzalez-Cuevas⁹ D. Gonzalez Diaz⁸³ M. Gonzalez-Lopez¹²⁹
69 M. C. Goodman⁷ O. Goodwin¹³⁰ S. Goswami¹⁵⁹ C. Gotti⁸⁹ E. Goudzovski¹⁷ C. Grace¹²⁴
70 M. Graham¹⁷¹ R. Gran¹³⁸ E. Granados⁷⁵ P. Granger²⁴ A. Grant⁵² C. Grant¹⁹ D. Gratieri⁶⁸
71 P. Green¹³⁰ L. Greenler²⁰⁴ J. Greer²⁰ J. Grenard²⁵ W. C. Griffith¹⁸³ M. Groh⁴⁵ J. Grudzinski⁷
72 K. Grzelak¹⁹⁹ W. Gu²¹ E. Guardincerri¹²⁶ V. Guarino⁷ M. Guarise^{86 66} R. Guenette⁷⁷
73 E. Guerard¹⁵⁴ M. Guerzoni⁸⁴ A. Guglielmi⁹² B. Guo¹⁷⁹ K. K. Guthikonda¹¹⁷ R. Gutierrez⁶
74 P. Guzowski¹³⁰ M. M. Guzzo³⁶ S. Gwon⁴⁰ C. Ha⁴⁰ A. Habig¹³⁸ H. Hadavand¹⁸⁹ R. Haenni¹⁵
75 A. Hahn⁶⁵ J. Haiston¹⁷⁷ P. Hamacher-Baumann¹⁵¹ T. Hamernik⁶⁵ P. Hamilton¹⁰¹ J. Han¹⁶¹
76 D. A. Harris^{207 65} J. Hartnell¹⁸³ J. Harton⁴⁵ T. Hasegawa¹¹⁵ C. Hasnip¹⁵¹ R. Hatcher⁶⁵
77 K. W. Hatfield³⁰ A. Hatzikoutelis¹⁷⁴ C. Hayes¹⁰⁴ K. Hayrapetyan¹⁶⁵ J. Hays¹⁶⁵ E. Hazen¹⁹
78 M. He⁷⁹ A. Heavey⁶⁵ K. M. Heeger²⁰⁵ J. Heise¹⁷² K. Hennessy¹²⁵ S. Henry¹⁶⁷ M. A. Hernandez
79 Morquecho¹⁰⁰ K. Herner⁶⁵ L. Hertel³⁰ J. Hewes⁴¹ A. Higuera⁷⁹ T. Hill⁹⁹ S. J. Hillier¹⁷
80 A. Himmel⁶⁵ L.R. Hirsch¹⁸⁵ J. Ho⁷⁷ J. Hoff⁶⁵ A. Holin¹⁷⁰ E. Hoppe¹⁵² G. A. Horton-Smith¹¹⁸

81 M. Hostert⁵⁵ A. Hourlier¹³¹ B. Howard⁶⁵ R. Howell¹⁶⁷ I. Hristova¹⁷⁰ M. S. Hronek⁶⁵ J. Huang¹⁹⁰
82 J. Huang²⁹ J. Hugon¹²⁷ G. Iles¹⁰¹ N. Ilic¹⁹¹ A. M. Iliescu⁸⁴ R. Illingworth⁶⁵ G. Ingratta^{84 18}
83 A. Ioannisian²⁰⁶ L. Isenhower¹ R. Itay¹⁷¹ A. Izmaylov⁸² C.M. Jackson¹⁵² V. Jain² E. James⁶⁵
84 W. Jang¹⁸⁹ B. Jargowsky³⁰ F. Jediny⁴⁸ D. Jena⁶⁵ Y. S. Jeong^{40 107} C. Jesús-Valls⁸¹ X. Ji²¹
85 L. Jiang¹⁹⁸ S. Jiménez²⁶ A. Jipa²² R. Johnson⁴¹ N. Johnston¹⁰⁴ B. Jones¹⁸⁹ S. B. Jones¹⁹⁵
86 M. Judah¹⁶¹ C. K. Jung¹⁸¹ T. Junk⁶⁵ Y. Jwa⁴⁶ M. Kabirnezhad¹⁵¹ A. Kaboth^{168 170}
87 I. Kadenko¹²¹ D. Kalra⁴⁶ I. Kakorin¹¹⁰ A. Kalitkina¹¹⁰ F. Kamiya⁶³ N. Kaneshige³³
88 G. Karagiorgi¹⁴⁶ G. Karaman¹⁰⁷ A. Karcher¹²⁴ M. Karolak²⁴ Y. Karyotakis⁵¹ S. Kasai¹²⁰
89 S. P. Kasetti¹²⁷ L. Kashur⁴⁵ N. Kazaryan²⁰⁶ E. Kearns¹⁹ P. Keener¹⁵⁷ K.J. Kelly⁶⁵ E. Kemp³⁶
90 O. Kemularia⁷⁰ W. Ketchum⁶⁵ S. H. Kettell²¹ M. Khabibullin⁹⁵ A. Khotjantsev⁹⁵
91 A. Khvedelidze⁷⁰ D. Kim¹⁸⁷ B. King⁶⁵ B. Kirby²¹ M. Kirby⁶⁵ J. Klein¹⁵⁷ K. Koehler²⁰⁴
92 L. W. Koerner⁷⁹ S. Kohn^{28 124} P. P. Koller¹⁵ L. Kolupaeva¹¹⁰ D. Korablev¹¹⁰ M. Kordosky²⁰³
93 T. Kosc⁹⁶ U. Kose²⁵ V. A. Kostelecký¹⁰⁴ K. Kotheke²⁰ F. Krennrich¹⁰⁸ I. Kreslo¹⁵ W. Kropp³⁰
94 Y. Kudenko⁹⁵ V. A. Kudryavtsev¹⁷⁶ S. Kulagin⁹⁵ J. Kumar⁷⁸ P. Kumar¹⁷⁶ P. Kunze⁵¹
95 C. Kuruppu¹⁷⁹ V. Kus⁴⁸ T. Kutter¹²⁷ J. Kvasnicka⁴⁷ D. Kwak¹⁹³ A. Lambert¹²⁴ B. J. Land¹⁵⁷
96 K. Lande¹⁵⁷ C. E. Lane⁵³ K. Lang¹⁹⁰ T. Langford²⁰⁵ M. Langstaff¹³⁰ J. Larkin²¹ P. Lasorak¹⁸³
97 D. Last¹⁵⁷ C. Lastoria²⁶ A. Laundrie²⁰⁴ G. Laurenti⁸⁴ A. Lawrence¹²⁴ I. Lazanu²² R. LaZur⁴⁵
98 M. Lazzaroni^{90 137} T. Le¹⁹² S. Leardini⁸³ J. Learned⁷⁸ P. LeBrun⁹⁶ T. LeCompte⁷ C. Lee⁶⁵
99 S. Y. Lee¹¹³ G. Lehmann Miotto²⁵ R. Lehnert¹⁰⁴ M. A. Leigui de Oliveira⁶³ M. Leitner¹²⁴
100 L. M. Lepin¹³⁰ L. Li³⁰ S. W. Li¹⁷¹ T. Li⁵⁸ Y. Li²¹ H. Liao¹¹⁸ C. S. Lin¹²⁴ Q. Lin¹⁷¹ S. Lin¹²⁷
101 J. Ling¹⁸² A. Lister²⁰⁴ B. R. Littlejohn¹⁰⁰ J. Liu³⁰ S. Lockwitz⁶⁵ T. Loew¹²⁴ M. Lokajicek⁴⁷
102 I. Lomidze⁷⁰ K. Long¹⁰¹ K. Loo¹¹⁴ T. Lord²⁰⁰ J. M. LoSecco¹⁴⁷ W. C. Louis¹²⁶ X.-G. Lu¹⁵¹
103 K.B. Luk^{28 124} X. Luo³³ E. Luppi^{86 66} N. Lurkin¹⁷ T. Lux⁸¹ V. P. Luzio⁶³ D. MacFarlane¹⁷¹
104 A. A. Machado³⁶ P. Machado⁶⁵ C. T. Macias¹⁰⁴ J. R. Macier⁶⁵ A. Maddalena⁷² A. Madera²⁵
105 P. Madigan^{28 124} S. Magill⁷ K. Mahn¹³⁵ A. Maio^{122 59} A. Major⁵⁴ J. A. Maloney⁴⁹ G. Mandrioli⁸⁴
106 R. C. Mandujano³⁰ J. Maneira^{122 59} L. Manenti¹⁹⁵ S. Manly¹⁶⁷ A. Mann¹⁹² K. Manolopoulos¹⁷⁰
107 M. Manrique Plata¹⁰⁴ V. N. Manyam²¹ L. Manzanillas¹⁵⁴ M. Marchan⁶⁵ A. Marchionni⁶⁵
108 W. Marciano²¹ D. Marfatia⁷⁸ C. Mariani¹⁹⁸ J. Maricic⁷⁸ R. Marie¹⁵⁴ F. Marinho⁶² A. D. Marino⁴⁴
109 D. Marsden¹³⁰ M. Marshak¹³⁹ C. M. Marshall¹⁶⁷ J. Marshall²⁰⁰ J. Marteau⁹⁶ J. Martin-Albo⁸²
110 N. Martinez¹¹⁸ D.A. Martinez Caicedo¹⁷⁷ S. Martynenko¹⁸¹ V. Mascagna^{89 106} K. Mason¹⁹²
111 A. Mastbaum¹⁶⁹ M. Masud⁸² F. Matichard¹²⁴ S. Matsuno⁷⁸ J. Matthews¹²⁷ C. Mauger¹⁵⁷
112 N. Mauri^{84 18} K. Mavrokoridis¹²⁵ I. Mawby²⁰⁰ R. Mazza⁸⁹ A. Mazzacane⁶⁵ E. Mazzucato²⁴
113 T. McAskill²⁰¹ E. McCluskey⁶⁵ N. McConkey¹³⁰ K. S. McFarland¹⁶⁷ C. McGrew¹⁸¹ A. McNab¹³⁰
114 A. Mefodiev⁹⁵ P. Mehta¹¹² P. Melas¹⁰ O. Mena⁸² S. Menary²⁰⁷ H. Mendez¹⁶³ P. Mendez²⁵
115 D. P. M²¹ A. Menegolli^{93 156} G. Meng⁹² M. D. Messier¹⁰⁴ W. Metcalf¹²⁷ T. Mettler¹⁵ M. Mewes¹⁰⁴
116 H. Meyer²⁰² T. Miao⁶⁵ G. Michna¹⁷⁸ T. Miedema^{143 166} V. Mikola¹⁹⁵ R. Milincic⁷⁸ G. Miller¹³⁰
117 W. Miller¹³⁹ J. Mills¹⁹² C. Milne⁹⁹ O. Mineev⁹⁵ O. G. Miranda⁴² S. Miryala²¹ C. S. Mishra⁶⁵
118 S. R. Mishra¹⁷⁹ A. Mislivec¹³⁹ D. Mladenov²⁵ I. Mocioiu¹⁵⁸ K. Moffat⁵⁵ N. Moggi^{84 18}
119 R. Mohanta⁸⁰ T. A. Mohaya⁶⁵ N. Mokhov⁶⁵ J. Molina⁹ L. Molina Bueno⁸² E. Montagna^{84 18}
120 A. Montanari⁸⁴ C. Montanari^{93 65 156} D. Montanari⁶⁵ L. M. Montano Zetina⁴² J. Moon¹³¹
121 S. H. Moon¹⁹³ M. Mooney⁴⁵ A. F. Moor³⁵ D. Moreno⁶ C. Morris⁷⁹ C. Mossey⁶⁵ E. Motuk¹⁹⁵
122 C. A. Moura⁶³ J. Mousseau¹³⁴ G. Mouster¹²³ W. Mu⁶⁵ L. Muallem³⁴ J. Mueller⁴⁵ M. Muether²⁰²
123 S. Mufson¹⁰⁴ F. Muheim⁵⁸ A. Muir⁵² M. Mulhearn²⁹ D. Munford⁷⁹ H. Muramatsu¹³⁹

124 S. Murphy⁵⁷ J. Musser¹⁰⁴ J. Nachtman¹⁰⁷ S. Nagu¹²⁸ M. Nalbandyan²⁰⁶ R. Nandakumar¹⁷⁰
125 D. Naples¹⁶¹ S. Narita¹⁰⁹ A. Nath¹⁰² D. Navas-Nicolás²⁶ A. Navrer-Agasson¹³⁰ N. Nayak³⁰
126 M. Nebot-Guinot⁵⁸ K. Negishi¹⁰⁹ J. K. Nelson²⁰³ J. Nesbit²⁰⁴ M. Nessi²⁵ D. Newbold¹⁷⁰
127 M. Newcomer¹⁵⁷ D. Newhart⁶⁵ H. Newton⁵² R. Nichol¹⁹⁵ F. Nicolas-Arnaldos⁷³ E. Niner⁶⁵
128 K. Nishimura⁷⁸ A. Norman⁶⁵ A. Norrick⁶⁵ R. Northrop³⁹ P. Novella⁸² J. A. Nowak¹²³
129 M. Oberling⁷ J. P. Ochoa-Ricoux³⁰ A. Olivares Del Campo⁵⁵ A. Olivier¹⁶⁷ A. Olshevskiy¹¹⁰
130 Y. Onel¹⁰⁷ Y. Onishchuk¹²¹ J. Ott³⁰ L. Pagani²⁹ S. Pakvasa⁷⁸ G. Palacio⁵⁶ O. Palamara⁶⁵
131 S. Palestini²⁵ J. M. Paley⁶⁵ M. Pallavicini^{87 69} C. Palomares²⁶ J. L. Palomino-Gallo¹⁸¹
132 W. Panduro Vazquez¹⁶⁸ E. Pantic²⁹ V. Paolone¹⁶¹ V. Papadimitriou⁶⁵ R. Papaleo⁹⁴
133 A. Papanestis¹⁷⁰ S. Paramesvaran²⁰ S. Parke⁶⁵ E. Parozzi^{89 136} Z. Parsa²¹ M. Parvu²²
134 S. Pascoli^{55 18} L. Pasqualini^{84 18} J. Pasternak¹⁰¹ J. Pater¹³⁰ C. Patrick¹⁹⁵ L. Patrizii⁸⁴
135 R. B. Patterson³⁴ S. J. Patton¹²⁴ T. Patzak¹⁵⁵ A. Paudel¹¹⁸ B. Paulos²⁰⁴ L. Paulucci⁶³
136 Z. Pavlovic⁶⁵ G. Pawloski¹³⁹ D. Payne¹²⁵ V. Pec¹⁷⁶ S. J. M. Peeters¹⁸³ E. Pennacchio⁹⁶
137 A. Penzo¹⁰⁷ O. L. G. Peres³⁶ J. Perry⁵⁸ D. Pershey⁵⁴ G. Pessina⁸⁹ G. Petrillo¹⁷¹ C. Petta^{85 37}
138 R. Petti¹⁷⁹ F. Piastra¹⁵ L. Pickering¹³⁵ F. Pietropaolo^{25 92} R. Plunkett⁶⁵ R. Poling¹³⁹ X. Pons²⁵
139 N. Poonthottathil¹⁰⁸ F. Poppi^{84 18} S. Pordes⁶⁵ J. Porter¹⁸³ M. Potekhin²¹ R. Potenza^{85 37}
140 B. V. K. S. Potukuchi¹¹¹ J. Pozimski¹⁰¹ M. Pozzato^{84 18} S. Prakash³⁶ T. Prakash¹²⁴ M. Prest⁸⁹
141 S. Prince⁷⁷ F. Psihas⁶⁵ D. Pugnere⁹⁶ X. Qian²¹ M. C. Queiroga Bazetto³⁶ J. L. Raaf⁶⁵
142 V. Radeka²¹ J. Rademacker²⁰ B. Radics⁵⁷ A. Rafique⁷ E. Raguzin²¹ M. Rai²⁰⁰
143 M. Rajaoalisoa⁴¹ I. Rakhno⁶⁵ A. Rakotonandrasana⁵ L. Rakotondravohitra⁵
144 Y. A. Ramachers²⁰⁰ R. Rameika⁶⁵ M. A. Ramirez Delgado⁷⁵ B. Ramson⁶⁵ A. Rappoldi^{93 156}
145 G. Raselli^{93 156} P. Ratoff¹²³ S. Raut¹⁸¹ R. F. Razakamiandra⁵ E. Rea¹³⁹ J.S. Real⁷⁴
146 B. Rebel^{204 65} M. Reggiani-Guzzo¹³⁰ T. Rehak⁵³ J. Reichenbacher¹⁷⁷ S. D. Reitzner⁶⁵ H. Rejeb
147 Sfar²⁵ A. Renshaw⁷⁹ S. Rescia²¹ F. Resnati²⁵ A. Reynolds¹⁵¹ M. Ribas¹⁸⁵ S. Riboldi⁹⁰
148 C. Riccio¹⁸¹ G. Riccobene⁹⁴ L. C. J. Rice¹⁶¹ J. Ricol⁷⁴ A. Rigamonti²⁵ Y. Rigaut⁵⁷ D. Rivera¹⁵⁷
149 A. Robert⁷⁴ L. Rochester¹⁷¹ M. Roda¹²⁵ P. Rodrigues¹⁵¹ M. J. Rodriguez Alonso²⁵
150 E. Rodriguez Bonilla⁶ J. Rodriguez Rondon¹⁷⁷ L. A. Romo Villa¹⁸⁹ S. Rosauero-Alcaraz¹²⁹
151 M. Rosenberg¹⁶¹ P. Rosier¹⁵⁴ B. Roskovec³⁰ M. Rossella^{93 156} M. Rossi²⁵ J. Rout¹¹² P. Roy²⁰²
152 S. Roy⁷⁶ A. Rubbia⁵⁷ C. Rubbia⁷¹ F. C. Rubio⁸² B. Russell¹²⁴ D. Ruterbories¹⁶⁷
153 A. Rybnikov¹¹⁰ A. Saa-Hernandez⁸³ R. Saakyan¹⁹⁵ S. Sacerdoti¹⁵⁵ T. Safford¹³⁵ N. Sahu¹⁰³
154 P. Sala^{90 25} N. Samios²¹ O. Samoylov¹¹⁰ M. C. Sanchez¹⁰⁸ V. Sandberg¹²⁶ D. A. Sanders¹⁴⁰
155 D. Sankey¹⁷⁰ S. Santana¹⁶³ M. Santos-Maldonado¹⁶³ N. Saoulidou¹⁰ P. Sapienza⁹⁴
156 C. Sarasty⁴¹ I. Sarcevic⁸ G. Savage⁶⁵ V. Savinov¹⁶¹ A. Scaramelli⁹³ A. Scarff¹⁷⁶ A. Scarpelli²¹
157 T. Schaffer¹³⁸ H. Schellman^{150 65} S. Schifano^{86 66} P. Schlabach⁶⁵ D. Schmitz³⁹ K. Scholberg⁵⁴
158 A. Schukraft⁶⁵ E. Segreto³⁶ A. Selyunin¹¹⁰ C. R. Senise¹⁹⁴ J. Sensenig¹⁵⁷ M. Seoane⁸³
159 I. Seong³⁰ A. Sergi¹⁷ D. Sgalaberna⁵⁷ M. H. Shaevitz⁴⁶ S. Shafaq¹¹² M. Shamma³²
160 R. Sharankova¹⁹² H. R. Sharma¹¹¹ R. Sharma²¹ R. Kumar¹⁶⁴ T. Shaw⁶⁵
161 C. Shepherd-Themistocleous¹⁷⁰ A. Sheshukov¹¹⁰ S. Shin¹¹³ I. Shoemaker¹⁹⁸ D. Shooltz¹³⁵
162 R. Shrock¹⁸¹ H. Siegel⁴⁶ L. Simard¹⁵⁴ F. Simon^{65 132} N. Simos²¹ J. Sinclair¹⁵ G. Sinev¹⁷⁷
163 J. Singh¹²⁸ J. Singh¹²⁸ L. Singh²⁷ V. Singh^{27 13} R. Sipes²⁵ F. W. Sippach⁴⁶ G. Sirri⁸⁴
164 A. Sitrika¹⁷⁷ K. Siyeon⁴⁰ K. Skarpaas¹⁷¹ A. Smith³⁵ E. Smith¹⁰⁴ P. Smith¹⁰⁴ J. Smolik⁴⁸
165 M. Smy³⁰ E.L. Snider⁶⁵ P. Snopok¹⁰⁰ D. Snowden-Ifft¹⁴⁸ M. Soares Nunes¹⁸⁴ H. Sobel³⁰
166 M. Soderberg¹⁸⁴ S. Sokolov¹¹⁰ C. J. Solano Salinas¹⁰⁵ S. Söldner-Rembold¹³⁰ S.R. Soleti¹²⁴

167 **N. Solomey**²⁰² **V. Solovov**¹²² **W. E. Sondheim**¹²⁶ **M. Sorel**⁸² **A. Sotnikov**¹¹⁰ **J. Soto-Oton**²⁶
 168 **A. Sousa**⁴¹ **K. Soustruznik**³⁸ **F. Spagliardi**¹⁵¹ **M. Spanu**^{89 136} **J. Spitz**¹³⁴ **N. J. C. Spooner**¹⁷⁶
 169 **K. Spurgeon**¹⁸⁴ **R. Staley**¹⁷ **M. Stancari**⁶⁵ **L. Stanco**^{92 153} **R. Stanley**²⁰ **R. Stein**²⁰
 170 **H. M. Steiner**¹²⁴ **A. F. Steklain Lisboa**¹⁸⁵ **J. Stewart**²¹ **B. Stillwell**³⁹ **J. Stock**¹⁷⁷ **F. Stocker**²⁵
 171 **T. Stokes**¹²⁷ **M. Strait**¹³⁹ **T. Strauss**⁶⁵ **S. Striganov**⁶⁵ **A. Stuart**⁴³ **J. G. Suarez**⁵⁶ **H. Sullivan**¹⁸⁹
 172 **D. Summers**¹⁴⁰ **A. Surdo**⁸⁸ **V. Susic**¹⁴ **L. Suter**⁶⁵ **C. M. Sutura**^{85 37} **R. Svoboda**²⁹
 173 **B. Szczerbinska**¹⁸⁸ **A. M. Szelc**⁵⁸ **H. A. Tanaka**¹⁷¹ **B. Tapia Oregui**¹⁹⁰ **A. Tapper**¹⁰¹ **S. Tariq**⁶⁵
 174 **E. Tatar**⁹⁹ **R. Tayloe**¹⁰⁴ **A. M. Teklu**¹⁸¹ **M. Tenti**⁸⁴ **K. Terao**¹⁷¹ **C. A. Ternes**⁸² **F. Terranova**^{89 136}
 175 **G. Testera**⁸⁷ **T. Thakore**⁴¹ **A. Thea**¹⁷⁰ **J. L. Thompson**¹⁷⁶ **C. Thorn**²¹ **S. C. Timm**⁶⁵
 176 **V. Tishchenko**²¹ **J. Todd**⁴¹ **L. Tomassetti**^{86 66} **A. Tonazzo**¹⁵⁵ **D. Torbunov**¹³⁹ **M. Torti**^{89 136}
 177 **M. Tortola**⁸² **F. Tortorici**^{85 37} **N. Tosi**⁸⁴ **D. Totani**³³ **M. Touns**⁶⁵ **C. Touramanis**¹²⁵ **R. Travaglini**⁸⁴
 178 **J. Trevor**³⁴ **S. Trilov**²⁰ **W. H. Trzaska**¹¹⁴ **Y. Tsai**⁶⁵ **Y.-T. Tsai**¹⁷¹ **Z. Tsamalaidze**⁷⁰ **K. V. Tsang**¹⁷¹
 179 **N. Tsverava**⁷⁰ **S. Tufanli**²⁵ **C. Tull**¹²⁴ **E. Tyley**¹⁷⁶ **M. Tzanov**¹²⁷ **L. Uboldi**²⁵ **M. A. Uchida**³⁵
 180 **J. Urheim**¹⁰⁴ **T. Usher**¹⁷¹ **S. Uzunyan**¹⁴⁵ **M. R. Vagins**¹¹⁹ **P. Vahle**²⁰³ **G. A. Valdivieso**⁶⁰
 181 **E. Valencia**²⁰³ **V. Pia**^{84 18} **Z. Vallari**³⁴ **E. Vallazza**⁸⁹ **J. W. F. Valle**⁸² **S. Vallecorsa**²⁵ **R. Van**
 182 **Berg**¹⁵⁷ **R. G. Van de Water**¹²⁶ **F. Varanini**⁹² **D. Vargas**⁸¹ **G. Varner**⁷⁸ **J. Vasei**¹⁰⁴ **S. Vasina**¹¹⁰
 183 **G. Vasseur**²⁴ **N. Vaughan**¹⁵⁰ **K. Vaziri**⁶⁵ **S. Ventura**⁹² **A. Verdugo**²⁶ **S. Vergani**³⁵
 184 **M. A. Vermeulen**¹⁴³ **M. Verzocchi**⁶⁵ **M. Vicenzi**^{87 69} **H. Vieira de Souza**³⁶ **C. Vignoli**⁷²
 185 **C. Vilela**²⁵ **B. Viren**²¹ **T. Vrba**⁴⁸ **T. Wachala**¹⁴² **A. V. Waldron**¹⁰¹ **M. Wallbank**⁴¹ **C. Wallis**⁴⁵
 186 **H. Wang**³¹ **J. Wang**¹⁷⁷ **L. Wang**¹²⁴ **M.H.L.S. Wang**⁶⁵ **Y. Wang**³¹ **Y. Wang**¹⁸¹ **K. Warburton**¹⁰⁸
 187 **D. Warner**⁴⁵ **M.O. Wascko**¹⁰¹ **D. Waters**¹⁹⁵ **A. Watson**¹⁷ **P. Weatherly**⁵³ **A. Weber**^{170 151}
 188 **M. Weber**¹⁵ **H. Wei**²¹ **A. Weinstein**¹⁰⁸ **D. Wenman**²⁰⁴ **M. Wetstein**¹⁰⁸ **A. White**¹⁸⁹
 189 **L. H. Whitehead**³⁵ **D. Whittington**¹⁸⁴ **M. J. Wilking**¹⁸¹ **C. Wilkinson**¹²⁴ **Z. Williams**¹⁸⁹
 190 **F. Wilson**¹⁷⁰ **R. J. Wilson**⁴⁵ **W. Wisniewski**¹⁷¹ **J. Wolcott**¹⁹² **T. Wongjirad**¹⁹² **A. Wood**⁷⁹
 191 **K. Wood**¹⁸¹ **E. Worcester**²¹ **M. Worcester**²¹ **C. Wret**¹⁶⁷ **W. Wu**⁶⁵ **W. Wu**³⁰ **Y. Xiao**³⁰ **F. Xie**¹⁸³
 192 **E. Yandel**³³ **G. Yang**¹⁸¹ **K. Yang**¹⁵¹ **S. Yang**⁴¹ **T. Yang**⁶⁵ **A. Yankelevich**³⁰ **N. Yershov**⁹⁵
 193 **K. Yonehara**⁶⁵ **T. Young**¹⁴⁴ **B. Yu**²¹ **H. Yu**²¹ **H. Yu**¹⁸² **J. Yu**¹⁸⁹ **W. Yuan**⁵⁸ **R. Zaki**²⁰⁷ **J. Zalesak**⁴⁷
 194 **L. Zambelli**⁵¹ **B. Zamorano**⁷³ **A. Zani**⁹⁰ **L. Zazueta**²⁰³ **G. P. Zeller**⁶⁵ **J. Zennamo**⁶⁵ **K. Zeug**²⁰⁴
 195 **C. Zhang**²¹ **M. Zhao**²¹ **E. Zhivun**²¹ **G. Zhu**¹⁴⁹ **P. Zilberman**¹⁸¹ **E. D. Zimmerman**⁴⁴ **M. Zito**²⁴
 196 **S. Zucchelli**^{84 18} **J. Zuklin**⁴⁷ **V. Zutshi**¹⁴⁵ **R. Zwaska**⁶⁵

197 ¹*Abilene Christian University, Abilene, TX 79601, USA*

198 ²*University of Albany, SUNY, Albany, NY 12222, USA*

199 ³*University of Amsterdam, NL-1098 XG Amsterdam, The Netherlands*

200 ⁴*Antalya Bilim University, 07190 Döşemealtı/Antalya, Turkey*

201 ⁵*University of Antananarivo, Antananarivo 101, Madagascar*

202 ⁶*Universidad Antonio Nariño, Bogotá, Colombia*

203 ⁷*Argonne National Laboratory, Argonne, IL 60439, USA*

204 ⁸*University of Arizona, Tucson, AZ 85721, USA*

205 ⁹*Universidad Nacional de Asunción, San Lorenzo, Paraguay*

206 ¹⁰*University of Athens, Zografou GR 157 84, Greece*

207 ¹¹*Universidad del Atlántico, Barranquilla, Atlántico, Colombia*

208 ¹²*Augustana University, Sioux Falls, SD 57197, USA*

209 ¹³*Banaras Hindu University, Varanasi - 221 005, India*

210 ¹⁴University of Basel, CH-4056 Basel, Switzerland
211 ¹⁵University of Bern, CH-3012 Bern, Switzerland
212 ¹⁶Beykent University, Istanbul, Turkey
213 ¹⁷University of Birmingham, Birmingham B15 2TT, United Kingdom
214 ¹⁸Università del Bologna, 40127 Bologna, Italy
215 ¹⁹Boston University, Boston, MA 02215, USA
216 ²⁰University of Bristol, Bristol BS8 1TL, United Kingdom
217 ²¹Brookhaven National Laboratory, Upton, NY 11973, USA
218 ²²University of Bucharest, Bucharest, Romania
219 ²³Centro Brasileiro de Pesquisas Físicas, Rio de Janeiro, RJ 22290-180, Brazil
220 ²⁴IRFU, CEA, Université Paris-Saclay, F-91191 Gif-sur-Yvette, France
221 ²⁵CERN, The European Organization for Nuclear Research, 1211 Meyrin, Switzerland
222 ²⁶CIEMAT, Centro de Investigaciones Energéticas, Medioambientales y Tecnológicas, E-28040 Madrid,
223 Spain
224 ²⁷Central University of South Bihar, Gaya, 824236, India
225 ²⁸University of California Berkeley, Berkeley, CA 94720, USA
226 ²⁹University of California Davis, Davis, CA 95616, USA
227 ³⁰University of California Irvine, Irvine, CA 92697, USA
228 ³¹University of California Los Angeles, Los Angeles, CA 90095, USA
229 ³²University of California Riverside, Riverside CA 92521, USA
230 ³³University of California Santa Barbara, Santa Barbara, California 93106 USA
231 ³⁴California Institute of Technology, Pasadena, CA 91125, USA
232 ³⁵University of Cambridge, Cambridge CB3 0HE, United Kingdom
233 ³⁶Universidade Estadual de Campinas, Campinas - SP, 13083-970, Brazil
234 ³⁷Università di Catania, 2 - 95131 Catania, Italy
235 ³⁸Institute of Particle and Nuclear Physics of the Faculty of Mathematics and Physics of the Charles University,
236 180 00 Prague 8, Czech Republic
237 ³⁹University of Chicago, Chicago, IL 60637, USA
238 ⁴⁰Chung-Ang University, Seoul 06974, South Korea
239 ⁴¹University of Cincinnati, Cincinnati, OH 45221, USA
240 ⁴²Centro de Investigación y de Estudios Avanzados del Instituto Politécnico Nacional (Cinvestav), Mexico
241 City, Mexico
242 ⁴³Universidad de Colima, Colima, Mexico
243 ⁴⁴University of Colorado Boulder, Boulder, CO 80309, USA
244 ⁴⁵Colorado State University, Fort Collins, CO 80523, USA
245 ⁴⁶Columbia University, New York, NY 10027, USA
246 ⁴⁷Institute of Physics, Czech Academy of Sciences, 182 00 Prague 8, Czech Republic
247 ⁴⁸Czech Technical University, 115 19 Prague 1, Czech Republic
248 ⁴⁹Dakota State University, Madison, SD 57042, USA
249 ⁵⁰University of Dallas, Irving, TX 75062-4736, USA
250 ⁵¹Laboratoire d'Annecy de Physique des Particules, Univ. Grenoble Alpes, Univ. Savoie Mont Blanc, CNRS,
251 LAPP-IN2P3, 74000 Annecy, France
252 ⁵²Daresbury Laboratory, Cheshire WA4 4AD, United Kingdom
253 ⁵³Drexel University, Philadelphia, PA 19104, USA

- 254 ⁵⁴*Duke University, Durham, NC 27708, USA*
- 255 ⁵⁵*Durham University, Durham DH1 3LE, United Kingdom*
- 256 ⁵⁶*Universidad EIA, Envigado, Antioquia, Colombia*
- 257 ⁵⁷*ETH Zurich, Zurich, Switzerland*
- 258 ⁵⁸*University of Edinburgh, Edinburgh EH8 9YL, United Kingdom*
- 259 ⁵⁹*Faculdade de Ciências da Universidade de Lisboa - FCUL, 1749-016 Lisboa, Portugal*
- 260 ⁶⁰*Universidade Federal de Alfenas, Poços de Caldas - MG, 37715-400, Brazil*
- 261 ⁶¹*Universidade Federal de Goiás, Goiania, GO 74690-900, Brazil*
- 262 ⁶²*Universidade Federal de São Carlos, Araras - SP, 13604-900, Brazil*
- 263 ⁶³*Universidade Federal do ABC, Santo André - SP, 09210-580, Brazil*
- 264 ⁶⁴*Universidade Federal do Rio de Janeiro, Rio de Janeiro - RJ, 21941-901, Brazil*
- 265 ⁶⁵*Fermi National Accelerator Laboratory, Batavia, IL 60510, USA*
- 266 ⁶⁶*University of Ferrara, Ferrara, Italy*
- 267 ⁶⁷*University of Florida, Gainesville, FL 32611-8440, USA*
- 268 ⁶⁸*Fluminense Federal University, 9 Icaraí Niterói - RJ, 24220-900, Brazil*
- 269 ⁶⁹*Università degli Studi di Genova, Genova, Italy*
- 270 ⁷⁰*Georgian Technical University, Tbilisi, Georgia*
- 271 ⁷¹*Gran Sasso Science Institute, L'Aquila, Italy*
- 272 ⁷²*Laboratori Nazionali del Gran Sasso, L'Aquila AQ, Italy*
- 273 ⁷³*University of Granada & CAFPE, 18002 Granada, Spain*
- 274 ⁷⁴*University Grenoble Alpes, CNRS, Grenoble INP, LPSC-IN2P3, 38000 Grenoble, France*
- 275 ⁷⁵*Universidad de Guanajuato, Guanajuato, C.P. 37000, Mexico*
- 276 ⁷⁶*Harish-Chandra Research Institute, Jhansi, Allahabad 211 019, India*
- 277 ⁷⁷*Harvard University, Cambridge, MA 02138, USA*
- 278 ⁷⁸*University of Hawaii, Honolulu, HI 96822, USA*
- 279 ⁷⁹*University of Houston, Houston, TX 77204, USA*
- 280 ⁸⁰*University of Hyderabad, Gachibowli, Hyderabad - 500 046, India*
- 281 ⁸¹*Institut de Física d'Altes Energies (IFAE)—Barcelona Institute of Science and Technology (BIST), Barcelona,*
282 *Spain*
- 283 ⁸²*Instituto de Física Corpuscular, CSIC and Universitat de València, 46980 Paterna, Valencia, Spain*
- 284 ⁸³*Instituto Galego de Física de Altas Enerxias, A Coruña, Spain*
- 285 ⁸⁴*Istituto Nazionale di Fisica Nucleare Sezione di Bologna, 40127 Bologna BO, Italy*
- 286 ⁸⁵*Istituto Nazionale di Fisica Nucleare Sezione di Catania, I-95123 Catania, Italy*
- 287 ⁸⁶*Istituto Nazionale di Fisica Nucleare Sezione di Ferrara, I-44122 Ferrara, Italy*
- 288 ⁸⁷*Istituto Nazionale di Fisica Nucleare Sezione di Genova, 16146 Genova GE, Italy*
- 289 ⁸⁸*Istituto Nazionale di Fisica Nucleare Sezione di Lecce, 73100 - Lecce, Italy*
- 290 ⁸⁹*Istituto Nazionale di Fisica Nucleare Sezione di Milano Bicocca, 3 - I-20126 Milano, Italy*
- 291 ⁹⁰*Istituto Nazionale di Fisica Nucleare Sezione di Milano, 20133 Milano, Italy*
- 292 ⁹¹*Istituto Nazionale di Fisica Nucleare Sezione di Napoli, I-80126 Napoli, Italy*
- 293 ⁹²*Istituto Nazionale di Fisica Nucleare Sezione di Padova, 35131 Padova, Italy*
- 294 ⁹³*Istituto Nazionale di Fisica Nucleare Sezione di Pavia, I-27100 Pavia, Italy*
- 295 ⁹⁴*Istituto Nazionale di Fisica Nucleare Laboratori Nazionali del Sud, 95123 Catania, Italy*
- 296 ⁹⁵*Institute for Nuclear Research of the Russian Academy of Sciences, Moscow 117312, Russia*
- 297 ⁹⁶*Institut de Physique des 2 Infinis de Lyon, 69622 Villeurbanne, France*

298 ⁹⁷*Institute for Research in Fundamental Sciences, Tehran, Iran*
299 ⁹⁸*Instituto Superior Técnico - IST, Universidade de Lisboa, Portugal*
300 ⁹⁹*Idaho State University, Pocatello, ID 83209, USA*
301 ¹⁰⁰*Illinois Institute of Technology, Chicago, IL 60616, USA*
302 ¹⁰¹*Imperial College of Science Technology and Medicine, London SW7 2BZ, United Kingdom*
303 ¹⁰²*Indian Institute of Technology Guwahati, Guwahati, 781 039, India*
304 ¹⁰³*Indian Institute of Technology Hyderabad, Hyderabad, 502285, India*
305 ¹⁰⁴*Indiana University, Bloomington, IN 47405, USA*
306 ¹⁰⁵*Universidad Nacional de Ingeniería, Lima 25, Perú*
307 ¹⁰⁶*University of Insubria, Via Ravasi, 2, 21100 Varese VA, Italy*
308 ¹⁰⁷*University of Iowa, Iowa City, IA 52242, USA*
309 ¹⁰⁸*Iowa State University, Ames, Iowa 50011, USA*
310 ¹⁰⁹*Iwate University, Morioka, Iwate 020-8551, Japan*
311 ¹¹⁰*Joint Institute for Nuclear Research, Dzhelepov Laboratory of Nuclear Problems 6 Joliot-Curie, Dubna,*
312 *Moscow Region, 141980 RU*
313 ¹¹¹*University of Jammu, Jammu-180006, India*
314 ¹¹²*Jawaharlal Nehru University, New Delhi 110067, India*
315 ¹¹³*Jeonbuk National University, Jeonrabuk-do 54896, South Korea*
316 ¹¹⁴*University of Jyväskylä, FI-40014, Finland*
317 ¹¹⁵*High Energy Accelerator Research Organization (KEK), Ibaraki, 305-0801, Japan*
318 ¹¹⁶*Korea Institute of Science and Technology Information, Daejeon, 34141, South Korea*
319 ¹¹⁷*K L University, Vaddeswaram, Andhra Pradesh 522502, India*
320 ¹¹⁸*Kansas State University, Manhattan, KS 66506, USA*
321 ¹¹⁹*Kavli Institute for the Physics and Mathematics of the Universe, Kashiwa, Chiba 277-8583, Japan*
322 ¹²⁰*National Institute of Technology, Kure College, Hiroshima, 737-8506, Japan*
323 ¹²¹*Taras Shevchenko National University of Kyiv, 01601 Kyiv, Ukraine*
324 ¹²²*Laboratório de Instrumentação e Física Experimental de Partículas, 1649-003 Lisboa and 3004-516*
325 *Coimbra, Portugal*
326 ¹²³*Lancaster University, Lancaster LA1 4YB, United Kingdom*
327 ¹²⁴*Lawrence Berkeley National Laboratory, Berkeley, CA 94720, USA*
328 ¹²⁵*University of Liverpool, L69 7ZE, Liverpool, United Kingdom*
329 ¹²⁶*Los Alamos National Laboratory, Los Alamos, NM 87545, USA*
330 ¹²⁷*Louisiana State University, Baton Rouge, LA 70803, USA*
331 ¹²⁸*University of Lucknow, Uttar Pradesh 226007, India*
332 ¹²⁹*Madrid Autonoma University and IFT UAM/CSIC, 28049 Madrid, Spain*
333 ¹³⁰*University of Manchester, Manchester M13 9PL, United Kingdom*
334 ¹³¹*Massachusetts Institute of Technology, Cambridge, MA 02139, USA*
335 ¹³²*Max-Planck-Institut, Munich, 80805, Germany*
336 ¹³³*University of Medellín, Medellín, 050026 Colombia*
337 ¹³⁴*University of Michigan, Ann Arbor, MI 48109, USA*
338 ¹³⁵*Michigan State University, East Lansing, MI 48824, USA*
339 ¹³⁶*Università del Milano-Bicocca, 20126 Milano, Italy*
340 ¹³⁷*Università degli Studi di Milano, I-20133 Milano, Italy*
341 ¹³⁸*University of Minnesota Duluth, Duluth, MN 55812, USA*

342 ¹³⁹*University of Minnesota Twin Cities, Minneapolis, MN 55455, USA*
343 ¹⁴⁰*University of Mississippi, University, MS 38677 USA*
344 ¹⁴¹*University of New Mexico, Albuquerque, NM 87131, USA*
345 ¹⁴²*H. Niewodniczański Institute of Nuclear Physics, Polish Academy of Sciences, Cracow, Poland*
346 ¹⁴³*Nikhef National Institute of Subatomic Physics, 1098 XG Amsterdam, Netherlands*
347 ¹⁴⁴*University of North Dakota, Grand Forks, ND 58202-8357, USA*
348 ¹⁴⁵*Northern Illinois University, DeKalb, IL 60115, USA*
349 ¹⁴⁶*Northwestern University, Evanston, IL 60208, USA*
350 ¹⁴⁷*University of Notre Dame, Notre Dame, IN 46556, USA*
351 ¹⁴⁸*Occidental College, Los Angeles, CA 90041*
352 ¹⁴⁹*Ohio State University, Columbus, OH 43210, USA*
353 ¹⁵⁰*Oregon State University, Corvallis, OR 97331, USA*
354 ¹⁵¹*University of Oxford, Oxford, OX1 3RH, United Kingdom*
355 ¹⁵²*Pacific Northwest National Laboratory, Richland, WA 99352, USA*
356 ¹⁵³*Universtà degli Studi di Padova, I-35131 Padova, Italy*
357 ¹⁵⁴*Université Paris-Saclay, CNRS/IN2P3, IJCLab, 91405 Orsay, France*
358 ¹⁵⁵*Université de Paris, CNRS, Astroparticule et Cosmologie, F-75006, Paris, France*
359 ¹⁵⁶*Università degli Studi di Pavia, 27100 Pavia PV, Italy*
360 ¹⁵⁷*University of Pennsylvania, Philadelphia, PA 19104, USA*
361 ¹⁵⁸*Pennsylvania State University, University Park, PA 16802, USA*
362 ¹⁵⁹*Physical Research Laboratory, Ahmedabad 380 009, India*
363 ¹⁶⁰*Università di Pisa, I-56127 Pisa, Italy*
364 ¹⁶¹*University of Pittsburgh, Pittsburgh, PA 15260, USA*
365 ¹⁶²*Pontificia Universidad Católica del Perú, Lima, Perú*
366 ¹⁶³*University of Puerto Rico, Mayaguez 00681, Puerto Rico, USA*
367 ¹⁶⁴*Punjab Agricultural University, Ludhiana 141004, India*
368 ¹⁶⁵*Queen Mary University of London, London E1 4NS, United Kingdom*
369 ¹⁶⁶*Radboud University, NL-6525 AJ Nijmegen, Netherlands*
370 ¹⁶⁷*University of Rochester, Rochester, NY 14627, USA*
371 ¹⁶⁸*Royal Holloway College London, TW20 0EX, United Kingdom*
372 ¹⁶⁹*Rutgers University, Piscataway, NJ, 08854, USA*
373 ¹⁷⁰*STFC Rutherford Appleton Laboratory, Didcot OX11 0QX, United Kingdom*
374 ¹⁷¹*SLAC National Accelerator Laboratory, Menlo Park, CA 94025, USA*
375 ¹⁷²*Sanford Underground Research Facility, Lead, SD, 57754, USA*
376 ¹⁷³*Università del Salento, 73100 Lecce, Italy*
377 ¹⁷⁴*San Jose State University, San José, CA 95192-0106, USA*
378 ¹⁷⁵*Universidad Sergio Arboleda, 11022 Bogotá, Colombia*
379 ¹⁷⁶*University of Sheffield, Sheffield S3 7RH, United Kingdom*
380 ¹⁷⁷*South Dakota School of Mines and Technology, Rapid City, SD 57701, USA*
381 ¹⁷⁸*South Dakota State University, Brookings, SD 57007, USA*
382 ¹⁷⁹*University of South Carolina, Columbia, SC 29208, USA*
383 ¹⁸⁰*Southern Methodist University, Dallas, TX 75275, USA*
384 ¹⁸¹*Stony Brook University, SUNY, Stony Brook, NY 11794, USA*
385 ¹⁸²*Sun Yat-Sen University, Guangzhou, 510275*

- 386 ¹⁸³ *University of Sussex, Brighton, BN1 9RH, United Kingdom*
387 ¹⁸⁴ *Syracuse University, Syracuse, NY 13244, USA*
388 ¹⁸⁵ *Universidade Tecnológica Federal do Paraná, Curitiba, Brazil*
389 ¹⁸⁶ *University of Tennessee at Knoxville, TN, 37996, USA*
390 ¹⁸⁷ *Texas A&M University, College Station, Texas 77840*
391 ¹⁸⁸ *Texas A&M University - Corpus Christi, Corpus Christi, TX 78412, USA*
392 ¹⁸⁹ *University of Texas at Arlington, Arlington, TX 76019, USA*
393 ¹⁹⁰ *University of Texas at Austin, Austin, TX 78712, USA*
394 ¹⁹¹ *University of Toronto, Toronto, Ontario M5S 1A1, Canada*
395 ¹⁹² *Tufts University, Medford, MA 02155, USA*
396 ¹⁹³ *Ulsan National Institute of Science and Technology, Ulsan 689-798, South Korea*
397 ¹⁹⁴ *Universidade Federal de São Paulo, 09913-030, São Paulo, Brazil*
398 ¹⁹⁵ *University College London, London, WC1E 6BT, United Kingdom*
399 ¹⁹⁶ *Valley City State University, Valley City, ND 58072, USA*
400 ¹⁹⁷ *Variable Energy Cyclotron Centre, 700 064 West Bengal, India*
401 ¹⁹⁸ *Virginia Tech, Blacksburg, VA 24060, USA*
402 ¹⁹⁹ *University of Warsaw, 02-093 Warsaw, Poland*
403 ²⁰⁰ *University of Warwick, Coventry CV4 7AL, United Kingdom*
404 ²⁰¹ *Wellesley College, Wellesley, MA 02481, USA*
405 ²⁰² *Wichita State University, Wichita, KS 67260, USA*
406 ²⁰³ *William and Mary, Williamsburg, VA 23187, USA*
407 ²⁰⁴ *University of Wisconsin Madison, Madison, WI 53706, USA*
408 ²⁰⁵ *Yale University, New Haven, CT 06520, USA*
409 ²⁰⁶ *Yerevan Institute for Theoretical Physics and Modeling, Yerevan 0036, Armenia*
410 ²⁰⁷ *York University, Toronto M3J 1P3, Canada*

411 **ABSTRACT:** The ProtoDUNE-SP detector is a single-phase liquid argon time projection chamber
412 (LArTPC) that was constructed and operated in the CERN North Area at the end of the H4
413 beamline. This detector is a prototype for the first far detector module of the Deep Underground
414 Neutrino Experiment (DUNE), which will be constructed at the Sanford Underground Research
415 Facility (SURF) in Lead, South Dakota, USA. The ProtoDUNE-SP detector incorporates full-size
416 components as designed for DUNE and has an active volume of 7.672 m^3 . The H4 beam
417 delivers incident particles with well-measured momenta and high-purity particle identification.
418 ProtoDUNE-SP's successful operation between 2018 and 2020 demonstrates the effectiveness of
419 the single-phase far detector design. This paper describes the design, construction, assembly and
420 operation of the detector components.

421 **KEYWORDS:** Noble liquid detectors (scintillation, ionization, single-phase), Time projection cham-
422 bers, Large detector systems for particle and astroparticle physics, Scintillators, scintillation and
423 light emission processes (solid, gas and liquid scintillators), Photon detectors for UV, visible and IR
424 photons (solid-state) (PIN diodes, APDs, Si-PMTs, G-APDs, CCDs, EBCCDs, EMCCDs, CMOS
425 imagers, etc)

426 **ARXIV EPRINT:** [1234.56789](https://arxiv.org/abs/1234.56789)

427 **Contents**

428	1 Introduction	1
429	1.1 ProtoDUNE-SP in the Context of DUNE	1
430	1.2 Cryostat and Cryogenics	2
431	1.3 Detector Components	2
432	1.4 Data Acquisition and Detector Control	3
433	2 The Neutrino Platform at CERN	3
434	3 Cryostat and Cryogenics	7
435	3.1 Cryostat Assembly: Design, Installation and Validation	7
436	3.1.1 Cryostat Outer Structure	7
437	3.1.2 Insulation and Cold Membrane	8
438	3.1.3 Signal and Service Penetrations	9
439	3.1.4 Cryostat Assembly Procedure	11
440	3.2 Cryostat Structure Validation and Testing Campaigns	12
441	3.2.1 Cryostat Tightness Verification	12
442	3.2.2 Cryostat Mechanical Performance and Test Campaign	13
443	3.3 Cryogenics, Cooling and Purification System	15
444	3.3.1 Overview	16
445	3.3.2 Phases of Operation	19
446	3.3.3 Cryostat Pressure Control	21
447	3.3.4 Cryogenics Control System	22
448	3.3.5 Cryogenics Commissioning	23
449	4 Detector Components	24
450	4.1 Inner Detector: High Voltage	24
451	4.1.1 Cathode Plane Assembly (CPA)	24
452	4.1.2 Field Cage (FC)	27
453	4.1.3 Beam Plug	31
454	4.1.4 High Voltage (HV) Components	32
455	4.2 Inner Detector: Anode Plane Assemblies and Front-end Electronics	38
456	4.2.1 Anode Plane Assemblies (APA)	38
457	4.2.2 TPC Front-end Cold Electronics (CE)	43
458	4.2.3 TPC Front-end Warm Electronics	46
459	4.3 Inner Detector: Photon Detection System	52
460	4.3.1 Photon Collector: Dip-coated Wavelength-shifting Light Guides	53
461	4.3.2 Photon Collector: Double-shift Wavelength-shifting Light Guides	54
462	4.3.3 Photon Collector: ARAPUCA Light Trap	55
463	4.3.4 Photosensors	58
464	4.3.5 Photon Detector Readout Electronics	58

465	4.3.6	PDS Quality Control and Installation at CERN	60
466	4.3.7	Photon Detector UV-Light Calibration System	61
467	4.3.8	Full PDS Performance	63
468	4.4	Cosmic Ray Tagger (CRT)	65
469	4.5	Cryogenics Instrumentation	69
470	4.5.1	Purity Monitor	69
471	4.5.2	Temperature Sensors	72
472	4.5.3	Cameras	77
473	5	Detector Assembly, Testing and Installation	83
474	5.1	Detector Assembly	83
475	5.1.1	APA Preparation and Integration	84
476	5.1.2	CPA, Field Cage Preparation and Integration	85
477	5.2	Detector Installation	86
478	5.3	Cold Box Tests	87
479	5.4	Grounding and Shielding	90
480	6	Detector Readout and Control	92
481	6.1	Data Acquisition	92
482	6.2	Detector Control System	97
483	6.2.1	DCS Overview	98
484	6.2.2	DCS Architecture	100
485	7	Conclusions	103

486 **1 Introduction**

487 **1.1 ProtoDUNE-SP in the Context of DUNE**

488 The Deep Underground Neutrino Experiment (DUNE) will be a world-class neutrino observatory
489 and nucleon decay detector designed to answer fundamental questions about elementary particles
490 and their role in the universe. The international DUNE experiment, hosted by the U.S. Department
491 of Energy’s Fermilab, uses a near detector located at Fermilab and a far detector, 1300 km away,
492 located approximately 1.5 km underground at the Sanford Underground Research Facility (SURF)
493 in South Dakota, USA. The far detector will be a very large LArTPC with a fiducial mass of
494 40 kt (total mass 68 kt) of liquid argon (LAr), split into four modules. DUNE has been pursuing
495 two LArTPC technologies, single-phase (liquid only) and dual-phase (liquid and gas); this paper
496 describes ProtoDUNE-SP, a prototype for a single-phase (SP) detector module.

497 Construction of ProtoDUNE-SP was proposed to the CERN Super Proton Synchrotron Com-
498 mittee (SPSC) in June 2015 [1] and, following positive recommendations by SPSC and the CERN
499 Research Board in December 2015, was approved at CERN as experiment NP-04. ProtoDUNE-SP

500 has since been constructed and successfully operated at the CERN Neutrino Platform (NP). The
501 design of the ProtoDUNE-SP detector has been documented in a Technical Design Report [2].

502 ProtoDUNE-SP prototypes most of the components of a DUNE single-phase far detector
503 module at 1:1 scale, with an extrapolation of about 1:20 in total LAr mass. With a total LAr mass
504 of 0.77 kt, it represents the largest monolithic single-phase LArTPC detector built to date, and is a
505 significant experiment in its own right.

506 The ProtoDUNE-SP detector elements, the time projection chamber (TPC), the cold electronics
507 (CE), and the photon detection system (PDS), are immersed in a cryostat filled with the LAr target
508 material. The TPC consists of two vertical anode planes, one vertical cathode plane, and a
509 surrounding field cage. A cryogenics system maintains the LAr at a stable temperature of about
510 87 K and at the required purity level through a closed-loop process that recovers the evaporated
511 argon, recondenses, filters, and returns it to the cryostat.

512 ProtoDUNE-SP is located in an extension to the EHN1 hall in CERN's North Area, where a
513 new, dedicated charged-particle test beamline was constructed as part of the CERN NP program.
514 Construction and installation of ProtoDUNE-SP was completed in early July 2018. Filling with
515 LAr and commissioning took place in July and August of that year. First beam was delivered to
516 EHN1 on August 29, 2018 and the beam run was completed on November 11, 2018. The detector
517 continued to operate through July 19, 2020, collecting data to test and validate the technologies for
518 the future DUNE far detector modules, demonstrate operational stability, and explore operational
519 parameters.

520 The construction, installation, and operation of the ProtoDUNE-SP detector, as described in
521 this paper, has validated the design elements of the single-phase technology, the membrane cryostat
522 technology and associated cryogenics systems, as well as instrumentation, data acquisition, and
523 detector control. First performance results are presented in a separate paper [3].

524 **1.2 Cryostat and Cryogenics**

525 ProtoDUNE-SP implements the first large-dimension prototype cryostat built for a particle physics
526 detector based on the technology used for liquefied natural gas (LNG) storage and transport. Its
527 construction and operation serves as a validation of the membrane cryostat technology and associ-
528 ated cryogenics. The ProtoDUNE-SP cryostat was constructed in EHN1 without any mechanical
529 attachment to the floor or the building side walls. Its internal dimensions are 8.5 m in width and
530 length and 7.9 m in height. The cryostat and the cryogenics systems are described in detail in
531 Section 3.

532 **1.3 Detector Components**

533 The far detector DUNE-SP TPC components are designed in a modular way so that they can be
534 transported underground. The ProtoDUNE-SP components are therefore also modular. Six Anode
535 Plane Assemblies (APAs) are arranged into the two APA planes in ProtoDUNE-SP, each consisting
536 of three side-by-side APAs. Between them, a central cathode plane, composed of 18 Cathode
537 Plane Assembly (CPA) modules, splits the TPC volume into two electron-drift regions, one on
538 each side of the cathode plane. High voltage (HV) is delivered to the cathode plane by the HV
539 feedthrough. A field cage (FC) completely surrounds the four open sides of the two drift regions to

540 ensure that the electric field within is uniform and unaffected by the presence of the cryostat walls
541 and other nearby conductive structures. The detector dimensions are 7 m along the beam direction
542 (x coordinate), 7.2 m wide in the drift direction (y coordinate), and 6.1 m high (z coordinate). The
543 detector elements are suspended from the cryostat roof by the Detector Support Structure (DSS). The
544 Photon Detection System (PDS) modules are embedded in the APAs. They will collect scintillation
545 light from ionized LAr. Ten bar-shaped photon detectors with dimensions of 8.6 cm (height) 2.2 m
546 (length) and 0.6 cm (thickness) are installed at equally spaced heights within each APA. Three
547 different designs of photon-detector technologies are implemented in ProtoDUNE-SP, all based
548 on light readout by silicon photomultipliers (SiPM). Figure 1 illustrates how these components
549 fit together. Cryogenic instrumentation, including a purity monitor, temperature sensors, and
550 cameras, are located in the space between the cryostat walls and the detector elements. The detector
551 components are described in detail in Section 4, and Section 5 presents a description of how those
552 components were assembled together inside the cryostat.

553 **1.4 Data Acquisition and Detector Control**

554 The Data Acquisition (DAQ) system, a central element of ProtoDUNE-SP, interfaces with the
555 detector’s readout electronics, with external devices used for triggering (e.g., beam instrumentation),
556 with the Detector Control System (DCS), and with the offline computing. The DCS (known
557 historically as “slow control”) is in charge of the monitoring and control of the detector and includes
558 hardware and software elements that give information and access to the detector subcomponents.
559 The DAQ and DCS are described in Section 6 of this paper.

560 **2 The Neutrino Platform at CERN**

561 Following the recommendation issued by the 2013 European Strategy for Particle Physics [4]
562 the Neutrino Platform was established at CERN to foster the European contribution to the next
563 generation of long-baseline neutrino experiments. Use of this new and versatile facility is regulated
564 through Memorandum of Understanding (MOU) agreements, making it easy to welcome contribu-
565 tions from new collaborators and new projects within the facility. Since its establishment, several
566 new projects have been included and extensions of existing ones have been approved.

567 The CERN NP is located at the Prévessin site, in an extension of Building 887 (Experimental
568 Hall North 1 - EHN1) built explicitly for housing the two large-scale ProtoDUNEs, ProtoDUNE-SP
569 and the dual-phase ProtoDUNE-DP, where they can be exposed to charged particle beams. The
570 Neutrino Platform provides the infrastructure needed to safely construct, install, and operate the two
571 large LArTPCs, e.g., storage space for large components, dedicated overhead cranes for the handling
572 of heavy equipment by trained personnel, logistics and transport services coherently integrated with
573 the CERN global transport service, and mobile elevating working platform devices.

574 Each of the ProtoDUNEs is installed inside a cryostat located in an open trench in EHN1 12 m
575 deep. The building also houses prefabricated experimental control rooms and a cryogenics control
576 room, as well as rooms dedicated to data acquisition and computing/storage facilities. Figure 2
577 shows a layout of the experimental area.

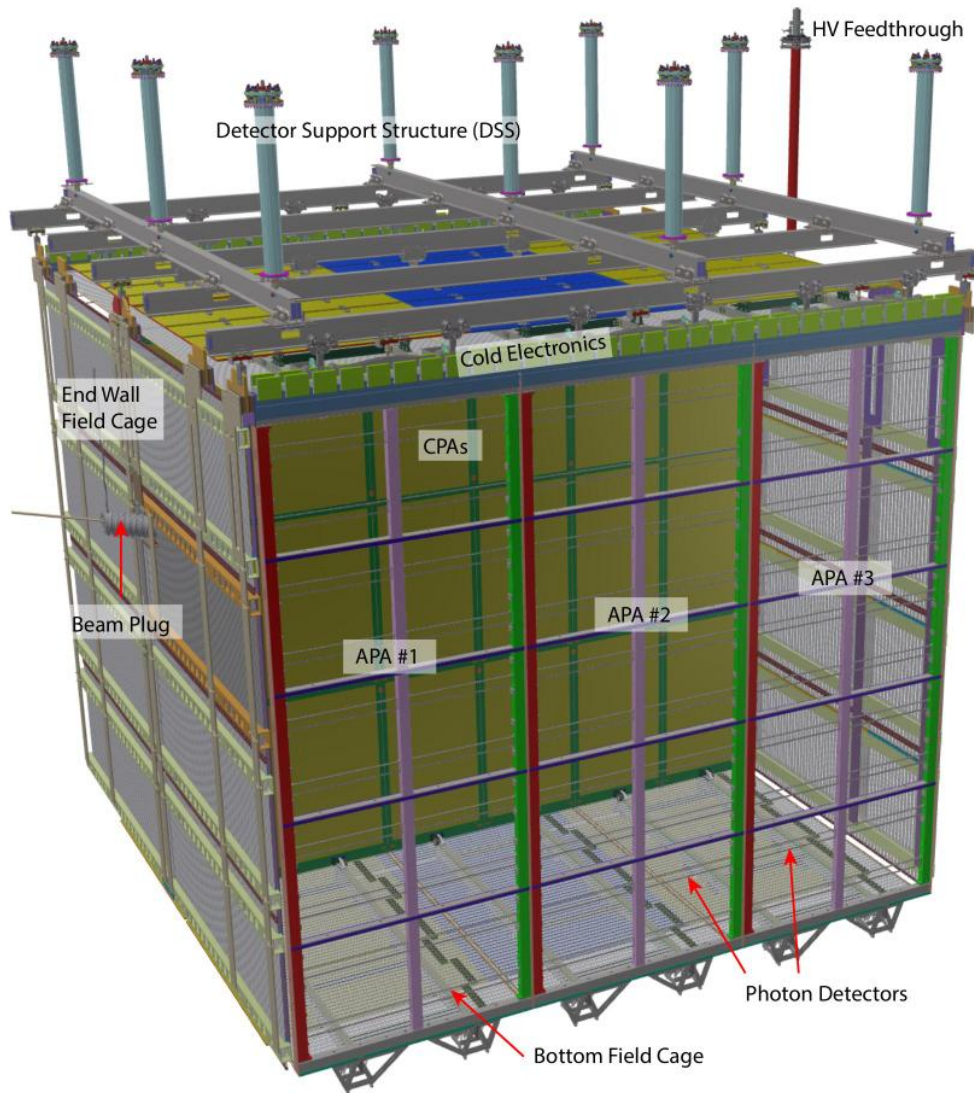


Figure 1: ProtoDUNE-SP Internal Components

578 A specialised piece of infrastructure is the so-called NP-04 cold box and its cryogenics sys-
 579 tem. Built for characterisation of the APAs at low temperature prior to their installation into the
 580 ProtoDUNE-SP cryostat, it is a tall, thin cryostat filled with cold nitrogen gas.

581 Two newly designed Very Low Energy (VLE) beamlines, H2 and H4, serve the two detectors
 582 [5]. Protons from the Super Proton Synchrotron (SPS) strike the T2 target about 600 m upstream of
 583 the detectors, generating secondary particles that collide with secondary targets that in turn produce
 584 particles of momenta in the region of 0.3-7 GeV/c [6]. The H4 beam is directed to ProtoDUNE-
 585 SP and the H2 beam to ProtoDUNE-DP. The beam lines and the beam instrumentation were
 586 commissioned in the summer of 2018 and the H4 beam extension was operated until the beginning
 587 of CERN's Long Shutdown 2 in November 2018 [7].

588 Two large clean rooms next to each cryostat were used to construct, assemble, and manipu-
 589 late the delicate detector components using procedures developed to ensure the required level of



Figure 2: Layout of the EHN1 experimental area. The Dual Phase cryostat is on the left, and the Single Phase cryostat is on the right.

590 cleanliness of the atmosphere and equipment.

591 Each cryostat has its own cryogenics system that comprises (1) the inner cryogenics and (2)
 592 the proximity cryogenics. These systems together provide and control the flow of the liquid and
 593 gases, and monitor and act to preserve both the thermodynamic conditions inside the cryostat and
 594 the liquid argon purity. The cryogenics system also has equipment external to the building that is
 595 used by both cryostats. This external system stores and delivers the liquid argon for the cryogenics
 596 operations as described in Section 3.3.

597 A very tight schedule and rigorous safety requirements led to very challenging installation and
 598 commissioning periods for the ProtoDUNE-SP cryostat and detector. A dedicated team and a set of
 599 tools and protocols were established to ensure that safety requirements were met and to coordinate
 600 parallel activities.

601 During the installation phase, mechanical and structural hazards posed the most significant
 602 safety concerns, and during the operational phase, cryogenics and radiation hazards were the
 603 prominent concerns. The facility was fully equipped to ensure safety of the personnel and the
 604 equipment at all times. Systems and procedures were put in place to mitigate risks associated
 605 with these hazards, including personnel training, specific risk analyses for non-standard activities,
 606 systems for oxygen deficiency hazard (ODH) monitoring and for fire detection, both linked to the
 607 hall ventilation and to the evacuation sirens and the CERN Fire Brigade. During beam operations,
 608 protocols were put in place to avoid accidental exposure to beam, e.g., access to the beam area
 609 and the trenches was controlled and interlocked with the beam. The radiation level in the hall
 610 was monitored with a series of strategically positioned radiation monitors integrated into the beam
 611 interlock system.

612 The CERN NP has approved Phase II of ProtoDUNE-SP, the most significant of its new
 613 projects and extensions. Starting in 2022, once the DUNE-SP detector component designs have
 614 implemented all the improvements of the past few years and are final, the components will be

615 installed in the same cryostat used for Phase I and tested.

616 3 Cryostat and Cryogenics

617 The cryostat consists of a free-standing warm steel outer structure, layers of insulation, and a cold
618 inner membrane. Its design is based on the technology used for liquefied natural gas (LNG) storage
619 and transport. The outer structure, which provides the mechanical support for the membrane and
620 its insulation, consists of vertical beams that alternate with a web of metal frames. It is designed to
621 withstand the hydrostatic pressure of the liquid argon and the pressure of the gas volumes, and to
622 satisfy the external constraints.

623 3.1 Cryostat Assembly: Design, Installation and Validation

624 The LBNF/DUNE far detector membrane cryostats are required to be constructed of modular
625 components that can be transported to the underground caverns at SURF via a 1.4 m × 3.8 m cross
626 section shaft for assembly *in situ*. The ProtoDUNE-SP cryostat, which is intended to validate the
627 far detector design, was constructed of modular components of the same design and size. The
628 maximum dimensions and weight of the cryostat components were optimized to work in both the
629 SURF and CERN locations.

630 The ProtoDUNE-SP cryostat design builds on similar technologies used for liquefied natural
631 gas (LNG) storage and transport tanker ships. A 1.2 mm thick corrugated stainless steel membrane
632 forms a sealed container for the liquid argon, with surrounding layers of thermal insulation and
633 vapor barriers. Outside these layers, a steel frame forms the outer (warm) vessel. The roof of the
634 cryostat supports most of the components and equipment within the cryostat, e.g., the time projection
635 chamber (TPC) and photon detection system (PDS) components, electronics, and sensors.

636 The ProtoDUNE-SP cryostat holds approximately 550 m³ of LAr, assuming an ullage of 5%,
637 at a temperature between 86.9 K and 88.2 K with an absolute pressure inside the volume in the
638 range 970–1100 mbar¹. The maximum design gauge pressure is 350 mbarg. The average heat leak
639 is tightly controlled and kept around 8 W/m² to avoid rapid boiling of the LAr and therefore limit
640 the consumption of liquid nitrogen (LN₂) which is used during normal operations to recondense
641 the boiled off argon via a heat exchanger.

642 The ProtoDUNE-SP cryostat and associated cryogenics have successfully validated the designs
643 for use in large-scale LArTPC experiments and in particular for the DUNE far detector.

644 3.1.1 Cryostat Outer Structure

645 The cryostat is a free-standing, electrically isolated structure assembled in the EHN1 hall at the
646 CERN Prévessin site. The room-temperature outer structure provides the structural integrity of the
647 entire setup, being capable of withstanding the hydrostatic pressure of the LAr, the pressure of the
648 argon vapor, the detector weight, and gravitational and seismic forces. The overall nominal outer
649 dimensions are: 11.4 m × 11.4 m × 10.8 m (W × L × H) and the nominal inner cryostat dimensions
650 are: 8.5 m × 8.5 m × 7.9 m.

651 These dimensions are dictated by several constraints: the required active volumes of LAr and
652 ullage, the layout of the penetrations, installation needs, distances from the active volume to the
653 cryostat inner walls, and insulation thicknesses.

¹the quoted pressure are referring to the pressure in the ullage, if not specified otherwise.

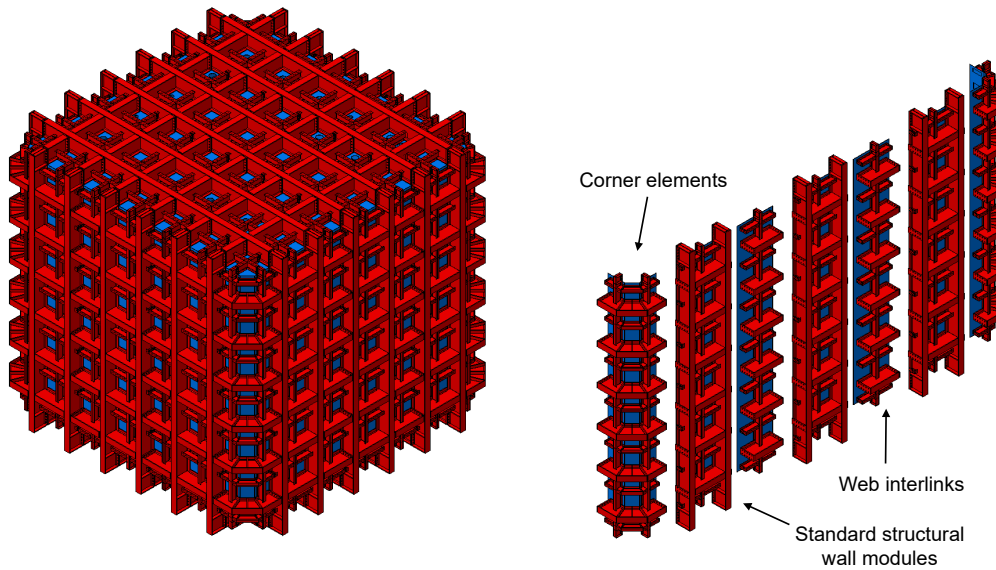


Figure 3: Left: diagram of the ProtoDUNE-SP warm vessel. Right: exploded view of one cryostat face showing the corner elements at each end, with standard structural modules, and the web interlinks used to assemble each face.

654 The outer structure consists of an assembly of prefabricated S460ML [8] steel modules of three
 655 configurations: standard structural modules used to construct the walls and floor, corner elements
 656 and a web of metallic frames to interconnect the modules. The complete structure and the modules
 657 used to assemble each face of the cryostat are shown in Figure 3. The modules are assembled using
 658 standard hot-rolled profiles welded together with bolted connections.

659 Three of the four cryostat outer walls are identical. The front wall, through which the beam
 660 enters, has a beam window (Section 4.1.3) and a separate wall section that is sealed in place over a
 661 Temporary Construction Opening (TCO), a 7.3 m high and 1.2 m wide entrance used for installing
 662 detector components.

663 3.1.2 Insulation and Cold Membrane

664 The inner vessel design, installed inside the warm support structure, is based on the LNG transport
 665 membrane technology developed by the firm GTT (Gaztransport & Technigaz) [9]. The overall
 666 thickness of the inner vessel is 800 mm. The design fulfills the requirement that thermal fluxes
 667 not exceed $5\text{-}6 \text{ W/m}^2$ ². The outermost layer of the inner vessel is a 10 mm thick stainless steel
 668 membrane [10] (the tertiary membrane) that provides an effective gas enclosure and allows for
 669 control of the nitrogen atmosphere inside the insulation volume, which prevents condensation in
 670 the insulation layer.

²This value also accounts for the aging properties of the insulation material (20 years of operation).

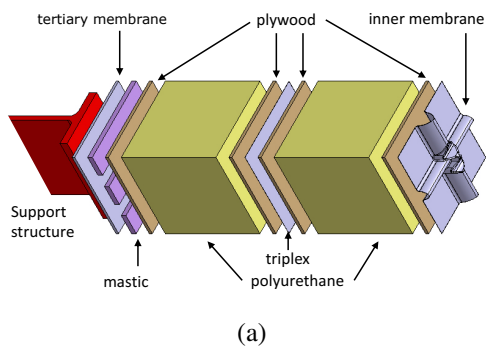


Figure 4: Left: the GTT inner vessel layers. Right: view of the inside of the cryostat ProtoDUNE-SP just after the finalisation of the primary membrane installation. The gold hue visible in the picture is an artifact of the lighting used during the installation, to protect the PDS.

671 Moving inward, just inside that membrane is the insulation layer that consists of two 390 mm
 672 thick layers of a foam specially developed for this purpose, supported by plywood plates of 9 mm
 673 and 12 mm thickness. The foam material is expanded polyurethane of density 90 kg/m^3 . The outer
 674 insulation layer is attached to the tertiary membrane by a set of rods and special mastic. Between
 675 the two insulation layers is a secondary LAr containment layer made of GTT-proprietary Triplex,
 676 a composite material consisting of a thin sheet of aluminum laminated on both sides by a layer
 677 of glass cloth and resin. In contact with the innermost side of the foam insulation is the 304L
 678 stainless steel 1.2 mm thick primary membrane that holds the LAr. The primary membrane can
 679 expand or shrink in two dimensions as a function of the temperature, thanks to a special corrugation
 680 configuration that allows it to respond like a bi-dimensional spring. A cross sectional view of the
 681 insulation and membrane layers is shown in Figure 4a. Figure 4b shows a view of the interior of the
 682 ProtoDUNE-SP cryostat before the insertion of the detector modules and the closure of the TCO.
 683 The corrugations of the primary membrane are visible.

684 Once all the large detector components have been installed inside the cryostat, the TCO is
 685 closed. The sealing is done in two steps since the entire length of the TCO is divided along the
 686 horizontal axis, into two parts. First the top part is bolted and sealed with the standard outer
 687 structure section. The layers of insulation are installed from inside the cryostat, following the
 688 standard sequence presented above. Once the primary membrane of the top part of the TCO is also
 689 installed, all the material needed for the bottom part is brought inside the cryostat and the sequence
 690 done for the top part is repeated. Since the sealing of the TCO involves welding activities inside the
 691 inner volume, a temporary “dirty room” was built to protect the detector components during those
 692 operations.

693 Figure 5 shows the TCO. The circular opening for the beam entrance is also visible.

694 3.1.3 Signal and Service Penetrations

695 The penetrations into the cryostat are installed on the roof of the warm structure, with a couple
 696 of exceptions. To keep the high level of purity required, LAr is extracted from a point as low as

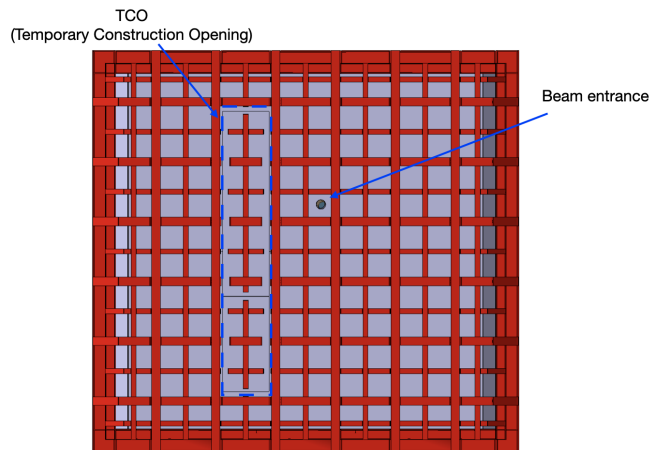


Figure 5: Front view of the ProtoDUNE-SP cryostat model. The Temporary Construction Opening and the cut-away for the beam entrance are shown.

697 possible in the cryostat and pushed by cryo-pumps to the external filtering system through the liquid
 698 recirculation circuit (see Section 3.3). A special penetration is thus required low on one of the
 699 cryostat's side walls to connect to the LAr pumps. This penetration has a dedicated system of safety
 700 valves and involves local modifications to the insulation panels and the primary membrane.

701 Since ProtoDUNE-SP was designed for exposure to a charged particle beam from CERN's
 702 SPS, a second modification to the cryostat was made to accommodate a beam window. The window
 703 minimises energy loss and scattering, which would be much higher if the beam were to pass through
 704 all the cryostat layers (see Section 4.1.3). The installation of the beam entrance window does not
 705 require any particular modification of the warm support structure. The tertiary membrane has been
 706 perforated with a hole where the beam entrance window is installed. The beam entrance window
 707 is composed of 175 μm -thick Mylar foil and a gate valve that opens when the beam is present
 708 and closes for safety reasons when the beam is off. The insulation between the secondary and the
 709 tertiary membrane is removed in the region around the beam window and the foam between the
 710 secondary and the primary membrane is replaced with a lower density foam (9 kg/m^3). Finally
 711 the plywood supporting the primary membrane in the vicinity of the beam window penetration is
 712 replaced with a Nomex honeycomb plate sandwiched between thin G10 layers. Nomex is a polymer
 713 material with high thermal resistance and Nomex sandwiches are well known for their structural
 714 resistance. Thermal and stress analyses to validate the design were conducted in collaboration with
 715 GTT. The total amount of material, including the (unaffected) primary membrane, given a 0.3 mm
 716 G10 thickness and a 0.3-mm-thick steel beam window, is equivalent to 10% of a radiation length.

717 The other penetrations, all on the cryostat roof, are grouped by position, diameter, and function.
 718 They provide feedthroughs for the TPC detector power and signals, support for the argon instru-
 719 mentation devices, and feedthroughs for the instrumentation signals. Of the 55 penetrations, 43 go
 720 through to the liquid of which seven are dedicated to the cryogenics system, nine to the detector
 721 support system, six to detector charge and light readout, and one to the cathode HV feedthrough.
 722 One is for the beamplug services, one for the diffuser fibre, 11 for the monitoring system (cameras,



Figure 6: Cryostat warm outer structure assembly sequence, left to right.

723 temperature and pressure sensors, purity monitors). There are also two manholes and five spares.
 724 The remaining 12 penetrations are limited to the insulation volume and are dedicated to either
 725 input/output of nitrogen gas or temperature and pressure sensors.

726 3.1.4 Cryostat Assembly Procedure

727 Figure 6 shows steps in the assembly sequence of the outer support structure. Installation starts with
 728 a planarity survey of the floor and the positioning of the elastomer pads and G10 strips (for seismic
 729 protection and electrical isolation) on which the cryostat will be placed. Three pre-assembled large
 730 wall pieces are positioned horizontally on temporary concrete supports, then three web interlink
 731 modules are positioned between them and connected together as shown in Figure 3 (right). The
 732 stainless-steel plates of the outermost (tertiary) membrane are then welded together and a helium
 733 leak test is performed to qualify the welds (see Section 3.2.1). To ensure the planarity of each
 734 completed wall, a detailed survey is carried out before it is lifted and installed in its final position
 735 on the elastometer pads. Wherever needed, temporary stabilisers are added to the experimental pit
 736 concrete walls to ensure safety during this process. Once the four walls are in place, the four pre-
 737 assembled cryostat corners are installed and the stabilisers are removed. Finally, the roof modules
 738 are assembled and the roof is installed. A final helium check of the SS plate welding is performed,
 739 and a global three-dimensional scan is done to verify the internal dimensions.

740 Once the outer structure and the tertiary membrane are installed, the pre-cut inner layer sections
 741 that come pre-assembled with mastic and fasteners are installed. After each layer is completed,
 742 all voids are filled to minimise any circulation paths. At the end, helium leak tests are performed

743 once again (see Section 3.2.1). The installation proceeds by layers (see Figure 4a) with the inner
744 membrane installed last. Installation of the ProtoDUNE-SP warm structure took about 12 weeks.

745 **3.2 Cryostat Structure Validation and Testing Campaigns**

746 Validation and certification of the cryostat structure has two aspects. The first, leak checking, is
747 performed at various stages of the cryostat construction. A description of these tests is given in
748 Section 3.2.1. The second concerns the mechanical behaviour of the cryostat in terms of compliance
749 with engineering safety standards and regulations. This validation is also performed multiple times
750 throughout the course of construction, and also includes a test campaign done during and after filling
751 with LAr. The structural and mechanical performance validation is described in Section 3.2.2.

752 **3.2.1 Cryostat Tightness Verification**

753 Leak testing is performed on the external warm structure, the inner membrane, and all the penetra-
754 tions. The tests are generally done using helium and a leak detector in *sniffing mode*. A deviation
755 from the environmental background ($2.3 \cdot 10^{-6}$ mbar l/s) is considered a possible leak.

756 **Warm Structure**

757 The walls of the cryostat outer structure (see Section 3.1.1), despite their separation from the LAr
758 volume, are required to be leak-tight for two main reasons: they are the last barrier between the
759 LAr volume and the external world; and any leaks on the outer surface would be sources of
760 localised heat and humidity injection. The latter would produce water that would freeze inside the
761 insulation volume, weakening it and making it less effective. The checks were performed during
762 the assembly of ProtoDUNE-SP and no leaks were found.

763 **Inner membrane**

764 The cryostat inner membrane (see Section 3.1.2) was tested twice for leaks. The first test, upon
765 completion of the membrane installation, was the official qualification for leak-tightness by the
766 vendor, and was performed on all welding seams. In this test, the insulation volume, normally
767 flushed with N₂ gas, undergoes a few cycles of evacuation (down to roughly 550 mbar), then is
768 filled with helium to match the external pressure. This allows a uniform fill of the insulation with
769 helium. Two test holes in the lower inner membrane are intentionally not welded at this stage,
770 but simply closed with mastic to allow occasional checks for the continued presence of helium in
771 the volume under test. The few small leaks found were swiftly repaired. These test conditions
772 also allowed for continuous monitoring of the insulation space internal pressure stability (Primary
773 Barrier Global Test).

774 The second leak test involved pulling vacuum around localised sections of welding lines and
775 testing them one by one. The test measures the leak rate from the helium-rich atmosphere, through
776 the welds of the primary membrane, to a local volume evacuated by means of a vacuum box
777 (Figure 7). The vacuum boxes come in a variety of shapes to fit corrugations, corners, and flat
778 welded regions. Overall, about 80% of the total length of welding lines on the inner membrane was
779 tested and no leaks were found. It is worth mentioning that a similar double-test procedure was
780 performed on the ProtoDUNE-DP cryostat's inner membrane and yielded the same result. This

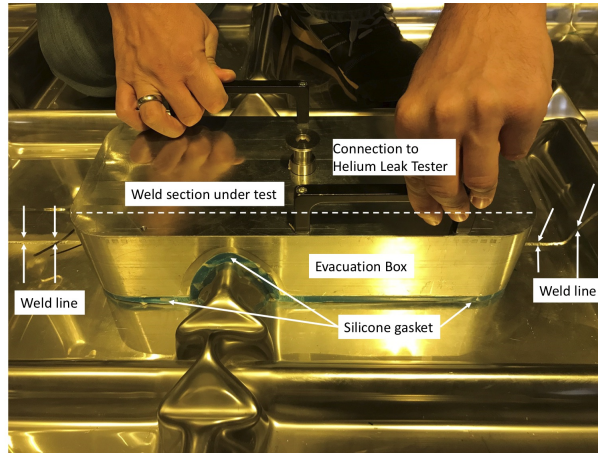


Figure 7: Example of vacuum box constructed for tests on flat walls. Two classes of such boxes were produced, in SS and in Plexiglas (lighter) for upside-down use on ceiling welding lines. The silicon-based gasket was produced by the CERN polymer lab.

781 gives confidence that the helium leak-check performed by the vendor can be fully trusted when it
 782 comes time to verify the cryostat inner membranes for the far detector, and that performing the
 783 second test will be unnecessary. Retesting single welded lines on a DUNE-scale cryostat would
 784 require months.

785 **Roof penetrations**

786 The leak-tightness of all feedthrough flanges was verified. This was done to avoid the potential
 787 formation of argon gas (GAr) pockets on the cryostat roof, a working area during operation, and also
 788 to prevent air leaks that could pollute the LAr volume. Each penetration was tested after closing
 789 the corresponding flanged connections.

790 The test procedure changed slightly depending on the stage of the detector preparation: the
 791 helium was injected into the penetration under test either from the inside (cryostat volume still
 792 accessible) or using the argon gas exhaust lines present in every penetration (detector installation
 793 completed).

794 All flanges except one were certified to be leak-tight; the chimney of one temperature profiler
 795 (see Section 4.5.2) was found to be faulty. None of the actions taken fixed the leak entirely, therefore
 796 an enclosure was constructed and installed around the leaky flange, defining a buffer volume in
 797 which argon gas circulated continuously.

798 **3.2.2 Cryostat Mechanical Performance and Test Campaign**

799 The cryostat inner and outer structures must satisfy European regulations and standards, as the
 800 ProtoDUNE-SP cryostat was installed and operated in Europe. In addition, since the design and the
 801 construction methods and technologies are prototypes for the larger DUNE cryostats, compliance
 802 with U.S. standards and regulations is also required.

803 Rigorous quality assurance and control procedures were carried out on all materials and
 804 techniques used for the construction of the ProtoDUNE-SP cryostat. The cryostat outer structure is

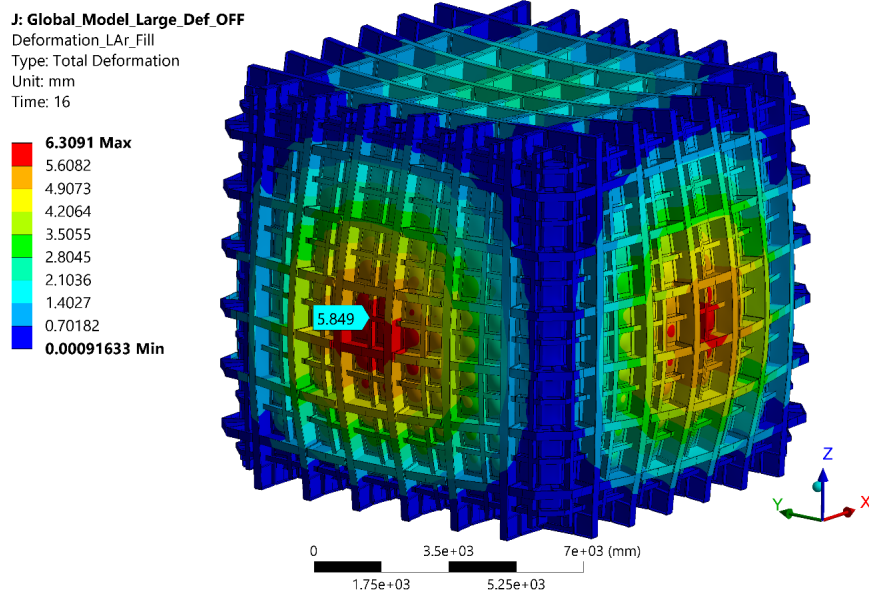


Figure 8: Expected deformation (using an exaggerated scale) of the cryostat during standard operations (liquid argon level of 7.4 m and 57 mbarg). Predictions are obtained using the *shell* FEA model (see text).

805 instrumented with strain gauges and displacement sensors for making the required measurements.
 806 To fully validate the mechanical performance of the cryostat, a careful stress analysis of each
 807 structural component was done, together with pressure tests before and after filling with LAr.

808 Two Finite Element Analysis (FEA) models were developed to evaluate the cryostat design
 809 against the required codes and regulations. Predictions from the models were compared to the
 810 experimental data collected during the commissioning phase and operation. A relatively simple
 811 *beam model* includes simulations only of the cryostat outer structure and is used to study the
 812 moments and forces acting on the cryostat. This model was developed for the relative ease of
 813 obtaining reliable verification studies. The *shell model* is a more complex simulation that includes
 814 the entire inner vessel, which contributes to the overall stiffness of the structure. This model was
 815 developed to provide detailed predictions of structural deformations as well as stresses on the frame
 816 and outer membrane. Its results are compared against the measured stresses to validate the cryostat
 817 behaviour for the sizing case (i.e., the cryostat full of LAr and at 350 mbarg over-pressure). It can
 818 predict strain and deformation during the three main phases: commissioning, filling with LAr, and
 819 operation. Figure 8 illustrates a possible deformation during standard operation. Note that the
 820 image vastly exaggerates the actual deformation.

821 Strain gauges and displacement sensors are installed at the positions where the simulation
 822 predicts the highest stresses. All sides of the cryostat are instrumented in similar locations to check
 823 the symmetrical behaviour of the structure.

824 Four displacement sensors, commonly known as *Linear Variable Differential Transformers*
 825 (LVDTs), are installed to monitor the symmetry and magnitude of the cryostat's global deformation.
 826 A total of 55 strain gauges (SGs) are used to measure local deformation of the structure under stress.

827 A detailed description of the instrumentation can be found in [11].

828 The sensors are read out continuously during cryogenics commissioning, in order to check
829 whether the maximum stresses and strains are exceeded in the most loaded areas and whether
830 the structure demonstrates elastic behaviour; monitor the maximum deformations and their
831 symmetry; serve as a secondary safety indicator of abnormal cryostat behaviour during com-
832 missioning.

833 The ProtoDUNE-SP monitoring system is complemented by a pressure gauge to measure the
834 pressure difference between the cryostat and the local atmospheric pressure, and four temperature
835 sensors to monitor variations in the pit where the cryostat is installed and on the surface of its outer
836 structure.

837 Pressure tests validate the safety of the cryostat under pressure so that work activities can
838 proceed in and around it, and they provide a final leak check on the cryostat roof penetrations. The
839 success of these tests is a fundamental prerequisite for the cryogenics safety permit approval, which
840 is required for the start of the cryogenics commissioning.

841 In a first pressure test, with the cryostat still empty, the over-pressure is increased to 200 mbarg,
842 then decreased in steps of 50 mbarg. The maximum value is that which allows testing of the overall
843 structure while keeping the most stressed areas within the elastic range. This value must also be
844 far below safety valve maximum pressure, which is set at 350 mbarg. A second pressure test is
845 performed at the end of the cryogenics commissioning, before starting operations, with the cryostat
846 96% full of LAr. The cryostat pressure is increased up to an over-pressure of 280 mbarg, again
847 in steps of 50 mbarg. When performed on ProtoDUNE-SP each test lasted a few hours and the
848 maximal over-pressure remained stable for about an hour.

849 All tests performed during the validation campaign were successful and the FEA model repro-
850 duced the cryostat behaviour in all cases. The pressure tests demonstrated the elastic behaviour of
851 the cryostat structure: strain gauges showed a clear linear relation with the pressure and returned to
852 zero at the end of the cycle (see Figure 9). Identically instrumented locations on the different walls
853 showed symmetric readings, with the exception of the wall with the closed TCO, where differences
854 are expected.

855 The values of the displacement and strain gauges measured during the fill were compared to
856 the FEA predictions and found to fulfill the safety requirements. This comparison also validated
857 the FEA model itself, which was then used to predict the cryostat behaviour at the sizing case. The
858 outcome of the simulation was compatible with both EU and U.S. standards, thus providing the
859 final qualification of the inner and outer cryostat mechanical structures.

860 **3.3 Cryogenics, Cooling and Purification System**

861 The cryogenics system provides the equipment and controls for receiving the argon, for purging,
862 cooling down, and filling the cryostat, for maintaining the LAr in the cryostat at the desired
863 temperature, pressure and level, and for purifying the argon and maintaining the required operational
864 purity. This system has been developed jointly by Fermilab and CERN, building on experience
865 at Fermilab from the Liquid Argon Purity Demonstrator (LAPD) [12], the 35t prototype, and
866 MicroBooNE, and at CERN from the WA105 1 1 3 Dual Phase prototype and the design and
867 operation of large-volume noble liquid detectors. The designed system described in this section is
868 or will be applied to both ProtoDUNEs, the Short-Baseline Neutrino Near Detector (SBND), and

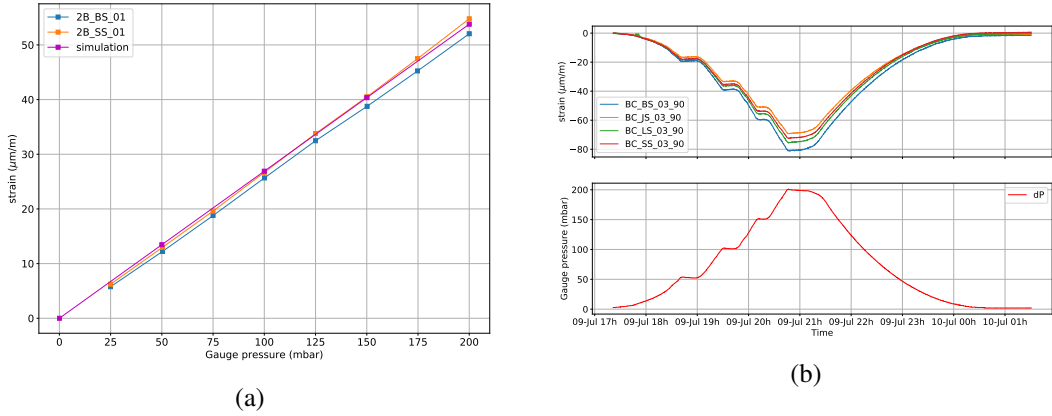


Figure 9: Sampled results from the first pressure test. Left: strain-vs-pressure plot of two uni-axial gauges on the I-beams compared against the FEA simulation. Right: four bi-axial gauges in the same positions on the different detector walls (top) are compared to the time-trend for the pressure (bottom).

869 the DUNE Far Detector [13]. The Far Detector implementation will differ in that it will generate
 870 the liquid nitrogen locally in the underground area.

871 3.3.1 Overview

872 The Process Flow Diagram for the ProtoDUNE cryogenics system is shown in Figure 10. The
 873 cryogenics infrastructure is divided into three main parts: the external cryogenics located outside
 874 the building housing the detector, the proximity cryogenics located next to the cryostat, and the
 875 internal cryogenics located inside the cryostat. The external cryogenics facility includes the systems
 876 used for the receipt and storage of the cryogens used in the cryogenics system. Designed to serve
 877 both ProtoDUNE detectors, separate lines take LAr, GAr, and LN₂ to both installations. A 50 m³
 878 (70 t LAr capacity) vertical dewar was used to receive the LAr deliveries for the ProtoDUNE-SP
 879 initial filling period. The specifications for the oxygen, water, and nitrogen contamination in the
 880 delivered argon are 2, 1, and 2 ppm, respectively. An analyzer rack near the dewar was used to
 881 check the levels of these impurities in the delivered LAr batches and a 55 kW vaporizer was used
 882 to deliver the gaseous argon to the cryostat. LN₂ deliveries were received and stored in a second
 883 50 m³ vertical dewar (40 t LN₂ capacity); the LN₂ is used in cool-down and normal operations,
 884 as explained below. A 0.5 m mechanical filter is located on the LAr feed line to prevent any
 885 impurities in the LAr supply from entering the purification system and the cryostat. Since a GAr/H₂
 886 mixture (2% H₂) is used to regenerate the LAr and GAr purification filters, a separate 10 m³ storage
 887 dewar dedicated to this function connects to a cylinder of hydrogen (H₂) and a GAr line.

888 To fulfill the LAr purity requirements, the LAr and the liquid boil-off needs to be collected,
 889 purified, and reintroduced into the system. The proximity cryogenics takes care of all actions
 890 during the recirculation of both in liquid and gas phase. The system comprises the argon condenser,
 891 the purification system for the LAr and GAr, the LAr circulation pumps, and the LAr/LN₂ phase
 892 separators.

893 The recirculation done at the liquid phase represents the major flow. During normal operations,
894 the continuous re-circulation rate was 7.0 t/h, giving a full volume turnover time of 4.6 days, which
895 kept the impurity concentration below 20 ppt oxygen equivalent. The LAr is transferred to the liquid
896 purification system via external pumps located on one side of the cryostat more than 5 m below
897 the liquid level to avoid cavitation or vapor-entrapment. This purification system further reduces
898 the initial impurity levels. The system has two pumps available to ensure continuous operation
899 during maintenance. Only one pump is in service at a time. The purification system consists of
900 three filter vessels; the first contains molecular sieve (4 Å) to remove water, and the others contain
901 alumina porous granules covered by highly active metallic copper for catalytic removal of O₂ by
902 Cu oxidization. In addition, 15 m mechanical filters are installed at the exit of the chemical
903 filters. Saturation of the chemical filter occurs when the trapped/reacted impurity budget exceeds
904 the removal capacity of the filter material. At this point the LAr flow is brought directly to the
905 mechanical filter and the regeneration of the saturated chemical filter can start. Filter regeneration
906 typically takes two days, after which the system returns to nominal operation.

907 The second main flow is given by the recirculation of the gas boil-off. The LAr in the cryostat
908 continuously evaporates at a slow rate due to unavoidable heat ingress. Therefore the boil-off is
909 collected, condensed, purified, and reintroduced into the system. The main part of the argon vapour,
910 roughly corresponding to 75% of the total boil-off, is collected via a dedicated penetration in the
911 cryostat roof. The vapor is then directed towards the argon condenser, which is a heat exchanger
912 that uses the vaporization of LN₂ to provide the cooling power to condense the GAR. The newly
913 condensed argon is then injected into the main liquid flow where it follows the liquid purification
914 path carried out by means of the cold filters. About 15% of the argon boil-off is removed through
915 purge pipes connected to each penetration on the roof. This portion of gas is driven towards a
916 purification system at RT that is composed of chemical filters similar to those used for the liquid.
917 The design has a diaphragm pump to raise the pressure of the gas and a pressure-control valve to
918 continuously monitor the gas flow to the condenser and maintain the pressure within the cryostat.
919 The standard operating pressure is 1050 mbar (absolute); on occasion the pressure was regulated
920 on gauge from a minimum of 10 mbar above ambient to a maximum of 250 mbar. Under standard
921 conditions the pressure regulation remains better than 1 mbar.

922 The diaphragm pump failed at some point during operations. While this pump was bypassed,
923 the flow of the argon gas was instead controlled by adjusting the pressure. This demonstrated that
924 the diaphragm pump was not essential and highlights the importance of designing flexibility into the
925 cryogenics system.

926 The internal cryogenics encompasses all the cryogenics equipment located inside the cryostat,
927 including manifolds for the cool-down operation and for the distribution of the liquid and gaseous
928 argon. The pipes for LAr distribution are positioned on the bottom of the cryostat and the outlets are
929 at the end of the pipes, roughly opposite to the side penetration from which the purification system
930 extracts the LAr (see Figure 11). The LAr entering the tank is warmer than the ambient by 0.4 K.
931 This is a consequence of the isentropic efficiency of the LAr pump and the total heat load going to
932 the transfer lines and valve boxes involved in the LAr circulation and purification processes. This
933 temperature difference is crucial in that it induces an upward flow of the newly purified argon from
934 its entry point at the bottom of the cryostat.

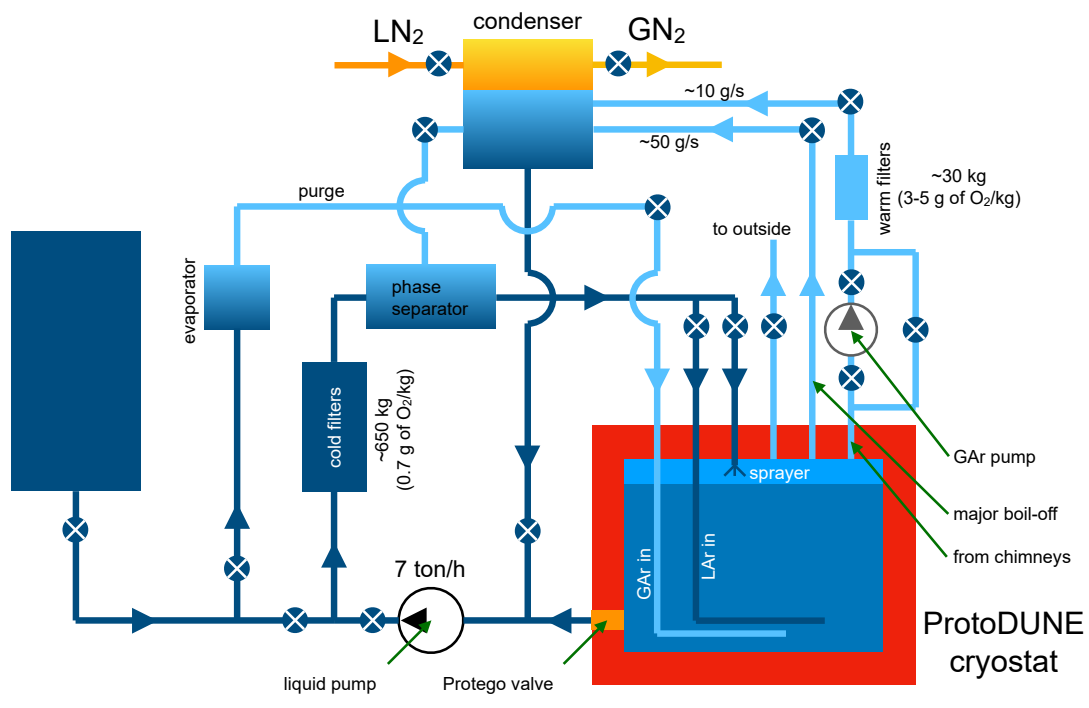


Figure 10: Cryogenics process flow diagram. Light and dark blue lines show the path of the argon gas and liquid, respectively. The yellow line shows the nitrogen line used to re-condense the gas argon via a condenser before being injected into the purification chain.

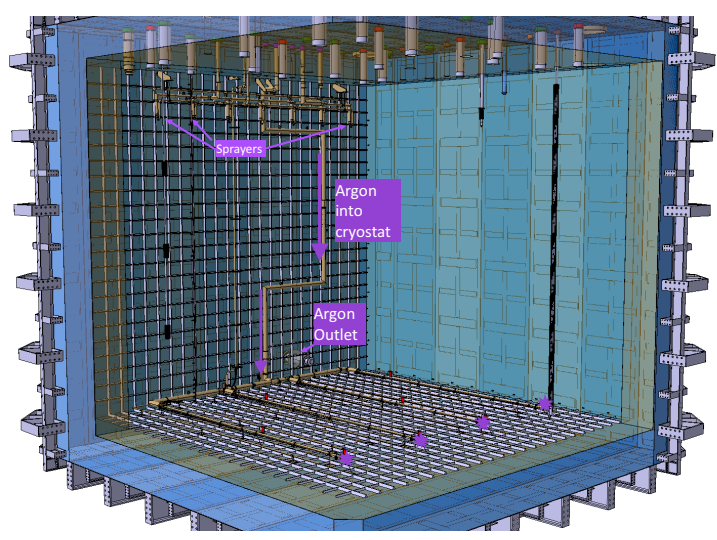


Figure 11: Cryogenics internal pipes and services.

935 3.3.2 Phases of Operation

936 Once the cryostat construction and the installation of all scientific equipment is complete, the
937 cryostat is cleaned (dust removal) in preparation for cool-down and fill. The first step is the purge
938 in open loop (also called piston-purge) in which the atmosphere in the cryostat is replaced with
939 argon gas. To ensure the purity of the input argon, the argon pipings are isolated, evacuated to less
940 than 0.1 mbar absolute pressure, and back-filled with high-purity argon gas. This cycle is repeated
941 several times to reduce contamination levels in the piping to the ppm level. The argon gas is then
942 injected into the cryostat through a set of pipes at the bottom of the cryostat. The flow nozzles are
943 directed downward to spread the gas across the bottom of the tank and produce a stable, upwardly
944 advancing argon wave front. The exhaust is removed from the top using the main GAR outlet and
945 vented outside of the building. A control valve regulates the pressure in the cryostat during this
946 entire operation. The side purge lines located on each roof penetration are also used to evacuate
947 the exhaust gas, ensuring that all volumes (especially trapped volumes) are properly purged. The
948 vertical flow velocity of the advancing GAR is set to 1.2 m/h, which is twice the diffusion rate of the
949 air downward. This causes the advancing pure argon-gas wave front to displace the air rather than
950 just dilute it. After 44 hours (seven volume changes), the purge process is complete with residual
951 air reduced to a few ppm.

952 The second stage of the purge process is done in "closed loop" for one week. During this stage
953 the GAR is recirculated through the GAR purifier and sent back to the bottom of the cryostat. The gas
954 purification system further removed the water-vapor outgassing from the FR4 circuit-board material
955 and the plastic-jacketed power and signal cables present inside the cryostat. This closed-loop purge
956 process further reduced the oxygen and water contamination inside the cryostat to sub-ppm and
957 ppm-levels, respectively, at which point the cool-down could start. It also allowed assessment of
958 the residual leak rate to atmosphere and the nitrogen content before cool-down.

959 The cool-down of the cryostat and detector is performed by flowing LAr and GAR into the
960 cryostat through a manifold located near the top. Sprayers deliver a mix of LAr and GAR in
961 atomised form that is distributed inside the cryostat by another set of GAR-only sprayers. During
962 this operation the gas is exhausted using the pressure control valve, keeping the cryostat pressure
963 at 70 mbarg. The sprayers guarantee a flat profile of the fluid (LAr and GAR) coming out, so as to
964 meet the cool-down requirements of the cryostat and in particular those of the detector, which are
965 more stringent. The maximum cool-down rate for the TPC is 40 K/h with a maximum temperature
966 difference between any two points in the detector volume of 50 K.

967 Once the cryostat and the TPC are cold, the fill starts. LAr is transferred through the cryostat-
968 filling pipework from the 70 t LAr storage tank via the filtration system for purification and the
969 LAr phase separator, which allow for the injection in the cryostat of argon in both liquid and gas
970 phases. The ProtoDUNE-SP filling process took about six weeks. Figure 12 shows the liquid level,
971 pressure, and temperature trends observed during the filling of the cryostat.

972 Once the cryostat is filled, the system can enter steady-state operation. During operation, as
973 shown in Figure 10, the boil-off that passes through the purge pipes on the signal feedthroughs
974 is filtered directly at room temperature and then condensed with the main boil off. Before being
975 reintroduced in the cryostat as liquid, it is purified and mixed with the bulk of the LAr coming from
976 the cryostat.

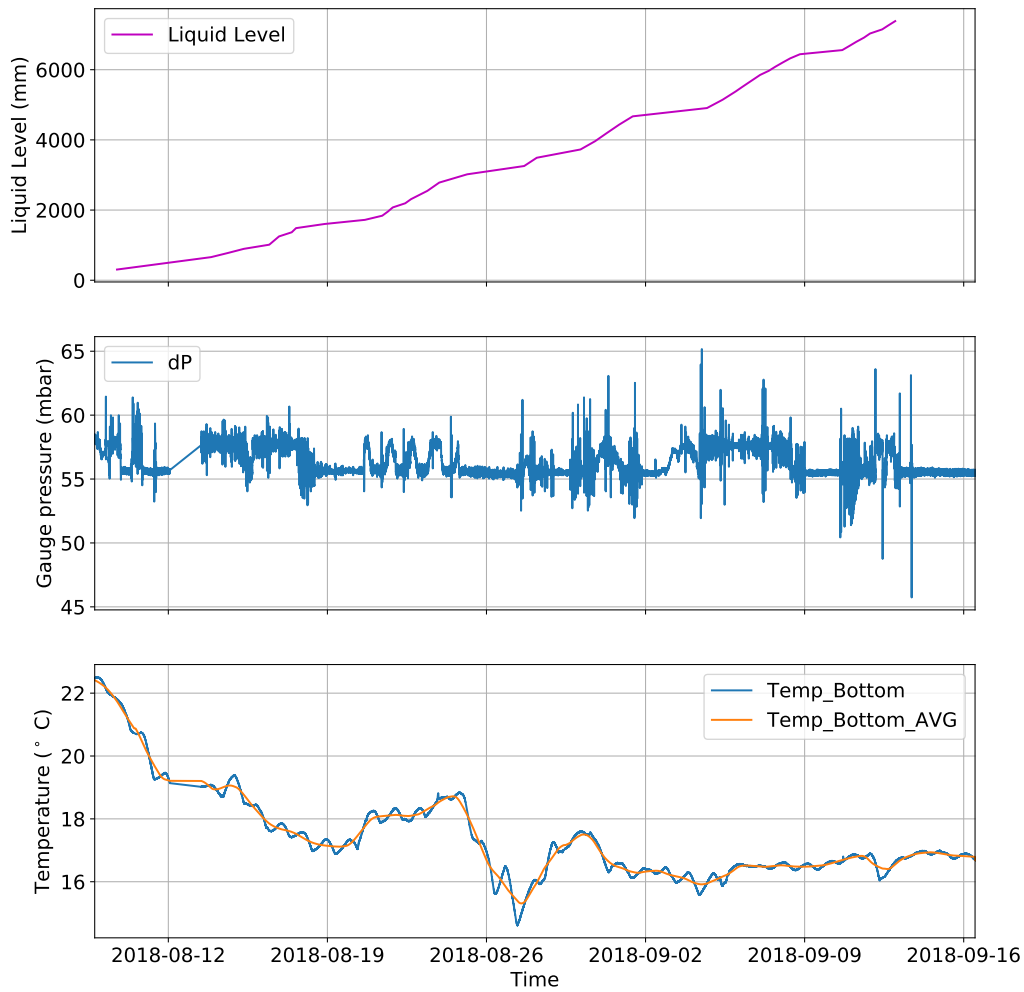


Figure 12: LAr level (top), pressure (middle) and cryostat outer structure temperature (bottom) trends during the filling of the NP04 cryostat.

Table 1: ProtoDUNE-SP cryogenics parameters after commissioning

Liquid level	7.45 m
Liquid volume	540 m ³
Liquid mass	752.76 t
Normal operating pressure	1050.00 mbar

977 Table 1 lists the final parameters of the ProtoDUNE-SP cryogenics, Figure 13 shows the stability
 978 of the cryostat pressure against ambient pressure variations during the beam run period (October -
 979 November 2018). Table 2 shows the heat leak balance of the cryogenics system as measured during
 980 steady-state operations after the cryogenics cold commissioning.

981 At the end of operations the tank will be emptied and the LAr will be returned to the storage
 982 tank outside the building, and from there unloaded back to LAr trucks.

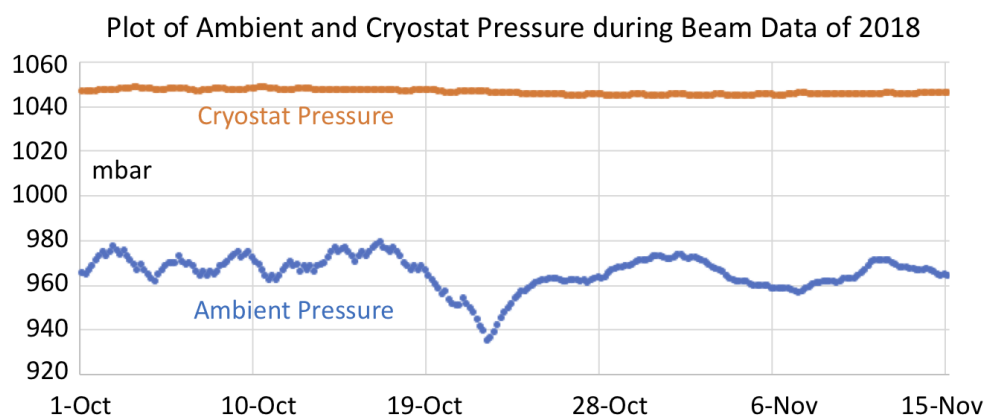


Figure 13: Stability of the pressure inside the cryostat versus atmospheric pressure variations during the beam period.

Table 2: Heat leak balance as measured during steady-state operations after the cryogenics cold commissioning

Circulation/purification process	2150 W
Proximity cryogenics	1200 W
Cryostat including top cap	5170 W
Miscellaneous (cold electronic, cables, penetrations, rods, etc..)	1980 W
TOTAL heat load	10500 W

983 3.3.3 Cryostat Pressure Control

984 The pressure inside the cryostat is maintained within a very narrow range by a set of active controls.
 985 Pressure-control valves can increase or decrease the cooling power in the condenser by controlling
 986 the amount of LN₂ flowing to the heat exchanger and the amount of GN₂ that is vented. Other
 987 pressure-control valves can be used to vent GAR to atmosphere and/or introduce clean GAR from
 988 the storage, as needed.

989 During normal operation the pressure-control valves are set to control the internal cryostat
 990 pressure to 1050 ± 1 mbar absolute. Excursions of a few percent from this value set off warnings
 991 to alert the operator to intervene, but more severe deviations (i.e., pressure exceeding 200 mbarg
 992 or going below 30 mbarg) trigger automatic actions: the system isolates the cryostat from any
 993 potential source of pressure, first closing the valves connecting the cryostat to the circuits used for
 994 gas make-up, purge, or cool-down, and the valve to the phase separator. Then the LAr circulation
 995 pump is stopped and the side penetration valves are closed.

996 If the pressure is too high, the system increases the LN₂ flow through the heat exchanger inside
 997 the condenser and powers down any heat sources within the cryostat (e.g., detector electronics). At
 998 this point some of the GAR is vented to reduce the pressure in a controlled way. On the other hand
 999 if the pressure is too low, fresh GAR can be introduced into the cryostat through the GAR make-up

1000 line, a line dedicated to taking in argon directly from the outside supply.

1001 The ability of the control system to maintain a set pressure is dependent on the size of pressure
1002 fluctuations (due to changes in flow, heat load, temperature, atmospheric pressure, etc.) and the
1003 volume of gas in the system. During normal operation ProtoDUNE-SP has 0.45 m of gas ullage at
1004 the top of the cryostat. This is 5% of the total argon volume and it is the typical vapour fraction
1005 used for cryogenic storage vessels. Reaction times to changes in the heat load are slow, typically on
1006 the order of one hour.

1007 The cryostat is equipped with an additional high-integrity, mechanical, fail-safe over-pressure
1008 and under-pressure protection system capable of preventing catastrophic structural failure of the
1009 cryostat in any condition. The system is composed of a diverter valve connected to a set of two
1010 devices, combination pressure and vacuum safety valves (PSV/VSVs), located on the cryostat roof.
1011 Functions for both over- and under-pressure are combined in a single device for efficiency. One of
1012 the two identical devices in the system is installed in service mode and the other in stand-by, to
1013 guarantee that one is always active in case, for example, maintenance is required.

1014 The device in service monitors the differential pressure between the inside and the outside of
1015 the cryostat and opens rapidly when the differential pressure is outside a preset range. In case of
1016 excessive pressure, the PSV/VSV opens and argon is released. The pressure within the cryostat falls
1017 and argon gas discharges into the argon vent riser. The valve is designed to close when the pressure
1018 returns below the preset level. In case the pressure detected is too low, the PSV/VSV opens and
1019 allows air to enter the cryostat to restore a safe positive pressure.

1020 **3.3.4 Cryogenics Control System**

1021 The cryogenics control system is a fully automated system that enables continuous cryogenic
1022 operation through the various modes of operation described in Section 3.3.2, while allowing manual
1023 actions by the operator as needed. It is a modular system, both in terms of the electrical and control
1024 hardware and the process control programming.

1025 This system's combination of automated and manual operation allowed its implementation at an
1026 early stage of the project, i.e., before the project inputs were fully defined, and enabled adjustments
1027 as the process and instrumentation evolved. It also made it possible to commission the cryogenics
1028 system in batches, i.e., to operate in one mode while implementing the control programming for the
1029 next mode.

1030 The electrical and control architecture is based on a functional analysis of the cryogenics sys-
1031 tem and the subsequent Product Breakdown Structure (PBS), Piping and Instrumentation Diagram
1032 (P&ID), parts list (detailing the characteristics of the instrumentation), and process logics specifi-
1033 cation. The hardware architecture consists of three different hardware installations, each controlled
1034 by a dedicated Programmable Logic Controller (PLC) Siemens s317, remote input/output mod-
1035 ules (I/O), and control cabinets. Each hardware installation corresponds to one of the three main
1036 cryogenics subsystems, namely, the external infrastructure for the storage and the proximity system
1037 for the two ProtoDUNE cryostats. Each control cabinet is dedicated to a specific function, e.g.,
1038 LAr/nitrogen management, purification, phase separation, condensing, argon circulation. Each
1039 cabinet includes industrial cryogenics instrumentation: actuators (valves, pumps) and sensors. The
1040 infrastructure for the ProtoDUNE-SP hardware installation includes a total of 10 control cabinets
1041 and 630 signals.

1042 The control system software was developed using the UNIfied Industrial COntrol System
1043 (UNICOS) [14]. The software architecture relies on a Process Control Object (PCO) breakdown
1044 structure. The process logic specification used as basis for the programming was designed with a
1045 modular structure and relies on associated option modes, sequencers, and interlocks. The option
1046 modes of the master PCO correspond to the sequence of operations of the cryogenics system,
1047 namely, default (which covers the fall-back situation with the cryostat pressure protection always
1048 active), open-loop purge, closed-loop purge, cool-down, fill, steady-state, and emptying. These
1049 option modes are used either to switch on a set of dependant units fulfilling the function for a given
1050 stage of operation or to set a collection of states of the controlled objects, e.g., fixed position or
1051 regulation mode for a valve, or a set-point.

1052 In case of abnormal behaviour, software interlocks prevent any further automatic actions.
1053 The specifications and programming were completed and implemented sequentially, in batches
1054 corresponding to the operation modes. This allowed starting safely with an incomplete system,
1055 continuing to program while the system was already in operation, and adjusting the program as
1056 needed during commissioning.

1057 The system is equipped with several features to ensure safe and continuous cryogenics operation,
1058 maintainability, and to provide flexibility for system evolution. For example, all equipment essential
1059 to the functioning of the system is powered from redundant electrical power supplies, including
1060 Uninterruptable Power Supplies (UPS) and diesel generators. Vacuum enclosures placed in the
1061 cryostat pit are constantly monitored. A degraded vacuum could signal a potential argon leak,
1062 therefore an alarm would be raised to indicate this condition.

1063 **3.3.5 Cryogenics Commissioning**

1064 Quality assurance and quality control were performed during the design, construction, installation
1065 and commissioning phases. During the construction and installation phases, non-destructive tests
1066 (X-rays, He leak tests and pressure tests) were successfully executed. During cold commissioning
1067 another series of tests was completed successfully, the main two of which were a check of the I/O
1068 signals and a functional test of all valves and equipment. The I/O check consisted of verifying
1069 all connections and the synchronisation of the 630 signals, testing the response to actions like
1070 opening/closing valves and to sensor readings, and verifying the sensor calibration or run calibration
1071 sequence for each control valve. In addition, tests were run on the Ethernet or hardwired signal lines
1072 dedicated to the exchange of information between the cryogenics system and the detector system,
1073 the safety system, and the CERN Central Control room.

1074 A ‘mirror’ station (not connected to the actual field equipment) provided a functional test
1075 environment for the process control logic. The tests were subsequently carried out on the real
1076 system to verify first alarms, interlocks, and the sequential function charts. Operation modes were
1077 tested afterwards, during the system commissioning.

1078 4 Detector Components

1079 4.1 Inner Detector: High Voltage

1080 A liquid argon time projection chamber (LArTPC) requires an equipotential cathode plane at high
1081 voltage (HV) and a precisely regulated interior electric field (E field) to drift electrons from particle
1082 interactions to sensor planes. The ProtoDUNE-SP LArTPC consists of a vertical cathode plane
1083 assembly (CPA), vertical anode plane assemblies (APAs), and sets of conductors surrounding the
1084 drift volume that are collectively called the field cage (FC). The FC provides a graded voltage profile
1085 between the CPA and APA in order to produce a uniform E field in the drift volume.

1086 Figure 14 shows the TPC configuration. Six top and six bottom FC modules connect the
1087 horizontal edges of the CPA and APA arrays, and four endwalls connect the vertical edges (two per
1088 drift volume). Each endwall is composed of four endwall modules. A Heinzinger -300 kV 0.5 mA
1089 HV power supply delivers voltage to the cathode. Two HV filters in series between the power supply
1090 and HV feedthrough filter out high-frequency fluctuations upstream of the cathode.



Figure 14: One of the two drift volumes of ProtoDUNE-SP. The FC modules enclose the drift volume between the CPA array (at the centre of the image) and the APA (upper right). The endwall FCs are oriented vertically; the top and bottom units are horizontal. The staggered printed circuit boards connecting the endwall FC profiles are the voltage divider boards.

1091 4.1.1 Cathode Plane Assembly (CPA)

1092 The CPA is located in the middle of the TPC, dividing the detector into two equal-distance drift
1093 volumes. The CPA's 7 m × 6 m area is made up of six panels, each of which is constructed of
1094 three vertically stacked modules. The same modular structure and materials will be used in the far
1095 detector design. The scope of the ProtoDUNE-SP CPA includes:

- 1096 • 18 CPA modules, each with a frame and resistive sheet,

- 1097 • HV bus connecting the resistive sheets and modules, and
- 1098 • HV cup for receiving input from the power supply.

1099 Several requirements are placed on the HV system. Electrically, the CPA must provide an
1100 equipotential surface at 180 kV nominal bias voltage that remains stable for data taking. The
1101 resistive sheet must provide slow discharge of accumulated charge in the event of an unexpected
1102 HV breakdown, to prevent damage to the readout electronics. To ensure a uniform drift field, the
1103 flatness must remain to within 1 cm while submerged in LAr. Mechanically, the CPA needs to
1104 support the full weight of the four connected top and bottom FC modules, as well as that of a
1105 person during the installation. It must allow for cryostat roof contraction during the cool-down to
1106 LAr temperature. Furthermore, it must be constructable within the cryostat, and its materials must
1107 inhibit trapped LAr volumes.

1108 CPA design

1109 The cathode plane surface is made of a resistive material, which, in the event of HV breakdown at
1110 a point on a CPA module, will restrict the sudden change in voltage to a relatively localised area,
1111 thus preventing discharges from potentially damaging either the cold electronics (CE), the cryostat,
1112 or the capacitively coupled anode planes. The rest of the CPA maintains its original bias voltage,
1113 and gradually discharges to ground through the high resistivity of the cathode material.

1114 The 18 CPA modules are constructed of strong 6 cm thick FR4 (the fire-retardant version of
1115 G10) frames. The frames hold 3 mm thick FR4 sheets laminated on both sides with a commercial
1116 resistive Kapton film of type D11261075 [15]. Each CPA module is 1.16 m wide and 2 m high,
1117 and they stack three high to form a CPA panel of height 6 m. The CPA plane consists of six panels
1118 placed side-by-side and has the same dimensions as each of the two APA planes.

1119 The surface of the frame facing the APAs is covered by a set of resistive FR4 strips with a bias
1120 voltage different from that of the CPA resistive sheets, chosen such that the frame itself causes no
1121 distortion in the drift field.

1122 The outer edges of the cathode plane facing the cryostat wall are covered with the same metal
1123 profile assemblies as used in the field cage (FC), described in Section 4.1.2. This limits electric
1124 field strength to below 30 kV/cm, as required, in the areas around the CPA frame and eliminates the
1125 need for a special design of these most crucial regions of the cathode plane. The edges of the CPA
1126 are effectively a continuation of the FC, as shown in Figure 15. Since the FC profiles are the only
1127 objects facing grounded surfaces, they are the most likely candidates for HV discharges to ground.
1128 To limit peak current flow, these edge profiles are connected to the field-shaping strips by means of
1129 a wire jumper.

1130 The CPA is connected to the HV feedthrough through a receptacle, called the *HV cup* as shown
1131 in Figure 15, at the downstream side of the cryostat (with respect to the beam entrance) and biased
1132 at 180 kV. It provides the voltage and the required current to all the FC modules (top, bottom, and
1133 end walls) through electrical interconnects (Section 4.1.2).

1134 The design takes into account deformation and stress due to the pressure from the circulating
1135 LAr as well as shrinkage due to the temperature change. For example, to ensure contact between
1136 the CPA modules after cool-down, a gap of 0.7 mm, corresponding to the calculated amount of

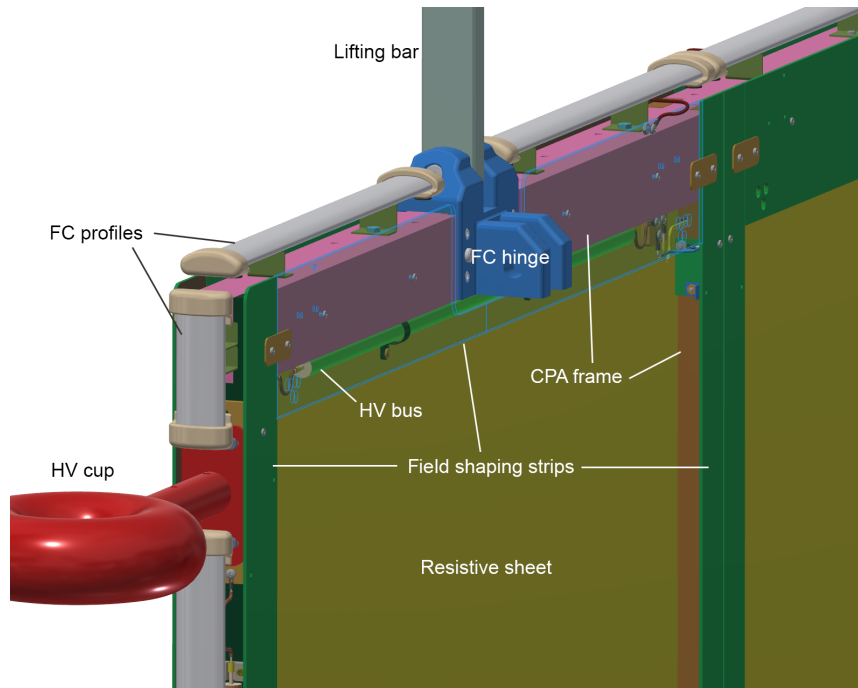


Figure 15: HV input cup connection to CPA array. The system of electrically interconnected HV buses allows biasing of the entire CPA at -180 kV and provides the required voltage and current to all the FC modules.

1137 separation that contraction will remove as they cool down, has been introduced. The joints between
 1138 the FC and the CPA are also designed to accommodate an estimated shrinkage of 5.2 mm of the
 1139 steel supporting beam between the CPA and APAs.

1140 **Mechanical and electrical interconnections between modules**

1141 Three modules are stacked vertically to form the 6 m height of a CPA panel as shown in Figure 16.
 1142 The frames of these modules are bolted together using tongue-and-groove connections at the ends.
 1143 The resistive cathode sheets and the field-shaping strips are connected using metallic tabs to ensure
 1144 redundant electrical contact between the CPAs.

1145 Each CPA panel is suspended from the cathode rail using a central lifting bar. Due to the roof
 1146 contraction as the cryostat is cooled, it was calculated that each CPA would move 2 mm relative
 1147 to its neighbours. Several pin-and-slot connections are implemented at the long edges of the CPA
 1148 panels to ensure the co-planarity of the modules while allowing for a small vertical displacement.

1149 The electrical connectivity of the resistive sheets within a CPA panel is maintained by several
 1150 tabs through the edge frames. The voltage is passed from one CPA panel to another through
 1151 embedded cables in the panels, referred to collectively as the HV bus, as shown in Figure 15.
 1152 Redundant connections in the HV bus between CPA panels are used to ensure reliability. The HV
 1153 bus also provides a low-resistance path for the voltage needed to feed the FC resistive divider chains.
 1154 The required connections to the FC modules are made at the edges of the CPA. Along its perimeter,
 1155 the HV bus cables are hidden between the field-shaping strip overhang and the main cathode resistive

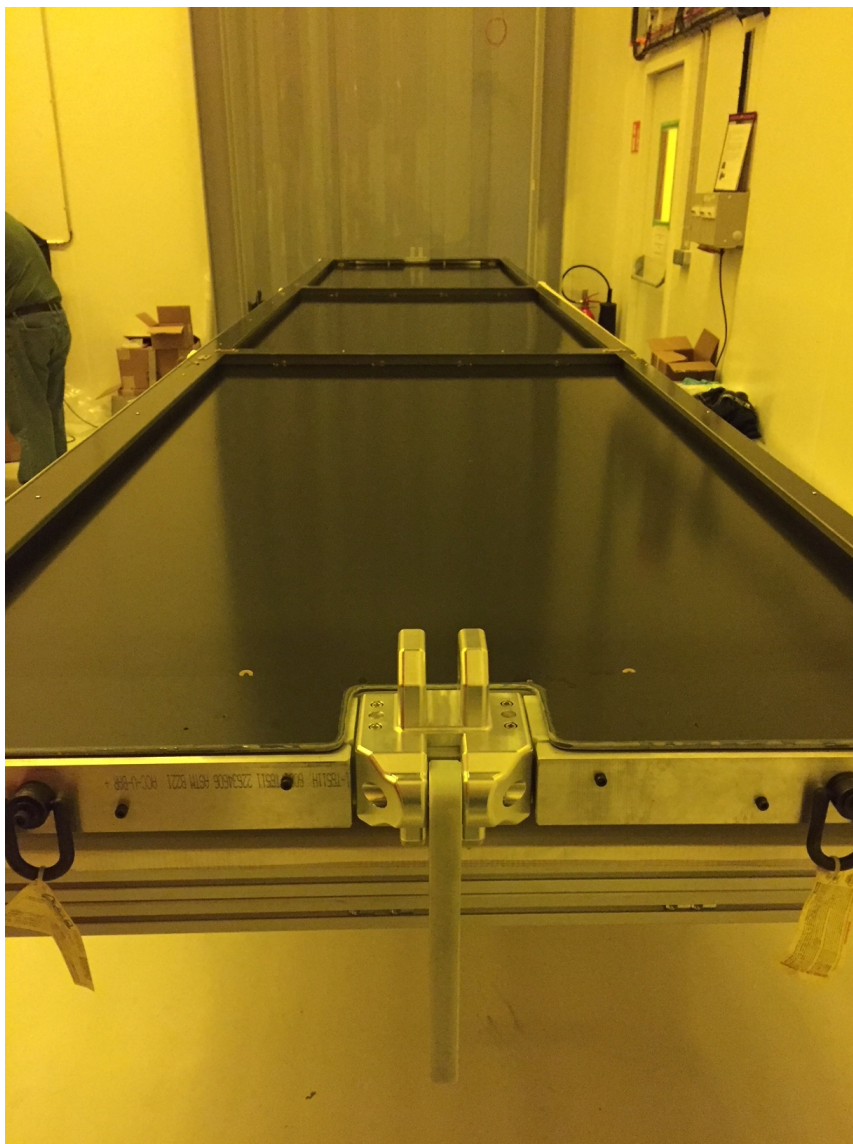


Figure 16: Completed 6 m long ProtoDUNE-SP CPA panel on the production table.

1156 sheet. The cables are capable of withstanding the full cathode bias voltage to prevent direct arcing
1157 to (and as a result, the recharging of) a CPA that discharges to ground. Connections are flexible in
1158 order to allow for FC deployment, thermal contraction, and motion between separately supported
1159 CPA components.

1160 **4.1.2 Field Cage (FC)**

1161 The FC covers the top, bottom, and endwalls of all the drift volumes, thus providing the necessary
1162 boundary conditions to ensure a uniform electric field and shielding it from the cryostat walls. The
1163 FC is made of adjacent extruded aluminum profiles running perpendicular to the drift field and
1164 set at increasing potentials along the 3.6 m drift distance from the CPA HV (-180kV) to ground
1165 potential at the APA planes. Other elements of the FC are the ground planes (GP) sitting above the

1166 top and below the bottom FC modules. They confine the electric field in the liquid phase, avoiding
1167 high field both in the gas phase at the top of the cryostat and close to the piping at the bottom.
1168 The structures holding the profiles are made of insulating fibreglass-reinforced plastic (FRP). FRP
1169 has good mechanical strength at cryogenic temperatures and low coefficient of thermal expansion.
1170 The FC modules come in two distinct types: the identical top and bottom modules, which run the
1171 full length of the detector, and the endwall FC modules, which are installed vertically to close the
1172 detector drift volume at either end.

1173 The FC is divided into mechanically and electrically independent modules, which comes
1174 with several advantages. As a consequence of electrically subdividing the modules, the stored
1175 energy and therefore the risk of detector damage is limited. In addition, the division acts as a
1176 protection from transient surges. FC modules have their own, independent voltage divider network
1177 providing the necessary linear voltage gradient. In case of a resistor failure in a divider chain field,
1178 distortions would be restricted to the FC module concerned. The mechanical subdivision simplifies
1179 construction and assembly of the FC.

1180 **Top/Bottom Field Cage and Ground Planes**

1181 There are six top and six bottom FC assemblies, all like the one shown in Figure 17. The assemblies
1182 are constructed from pultruded FRP I-beams and box beams that support the aforementioned alu-
1183 minium profiles. The length and width are 2.3 m and 3.5 m, respectively, each assembly comprising
1184 57 aluminum profiles. A GP consisting of modular perforated stainless steel sheets runs along the
1185 outside surface of each top and bottom FC with a 20 cm clearance. The gas region at the top of the
1186 volume, also referred to as the ullage, which is necessary for safe and stable operation of the LAr
1187 cryogenics system, contains many grounded conducting components with sharp features near which
1188 the electric field could easily exceed the breakdown strength of gaseous argon if directly exposed
1189 to the energised FC. The GP protects against this. The bottom FCs are equipped with GPs to shield
1190 from cryogenic piping and other sensors with sharp features on the cryostat floor.

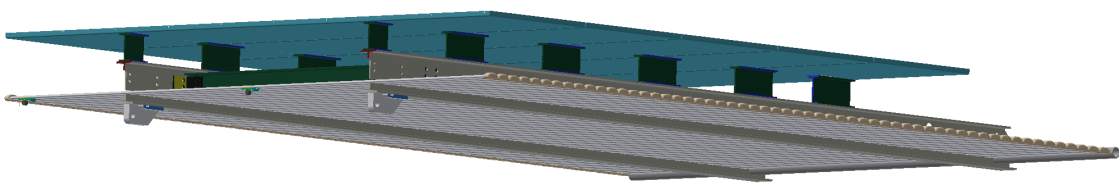


Figure 17: Drawings of a Top/Bottom FC module. The lower gray section illustrates the FC profiles and the upper blue section is the ground plane (GP).

1191 The connections between the top and bottom FC modules and the CPAs are made with aluminum
1192 hinges 2.54 cm in thickness that allow the modules to be folded in on the CPA during installation.
1193 The hinges are electrically connected to the second profile from the CPA. The connections to the
1194 APAs are made with stainless steel latches that are engaged once the top and bottom FC modules
1195 are unfolded and fully extended towards the APA. A top FC module being lifted for installation on
1196 the CPA panel is shown in Figure 18.



Figure 18: Lifting of a Top FC module for subsequent installation on the CPA panel. The side of the FC module that is lifted will attach to the CPA while the other side (bottom side) is connected with latches to the APA.

1197 **Endwall Field Cage**

1198 Each of the two drift volumes has two endwall FCs one on each end. Each endwall FC is in turn
1199 composed of four stacked endwall FC modules, the topmost equipped with hanger plates. Each
1200 endwall FC module is constructed of two FRP box beams each 3.5 m long as shown in Figure
1201 19 (dark grey) and Figure 20. The endwalls are not equipped with GPs as there is enough side
1202 clearance between the cryostat wall and FC, thus avoiding high E-fields. In ProtoDUNE-SP the
1203 endwall at the beam entry point is customized to hold the beam plug, described in Section 4.1.3.

1204 **Field Cage Profiles**

1205 The FC modules consist of extruded aluminum field-shaping-profiles. The profile shape minimises
1206 the electric field strength between a given profile and its neighbours and between a profile and
1207 other surrounding parts. The profile ends have a higher surface electric field, especially those at the
1208 corners of the FC (boundary with APA or CPA). To prevent HV breakdowns in the LAr, the ends
1209 of the profiles are encapsulated by custom UHMWPE (Ultra-High-Molecular-Weight Polyethylene)
1210 caps. The caps are designed and experimentally verified to withstand the full voltage across their
1211 thickness.

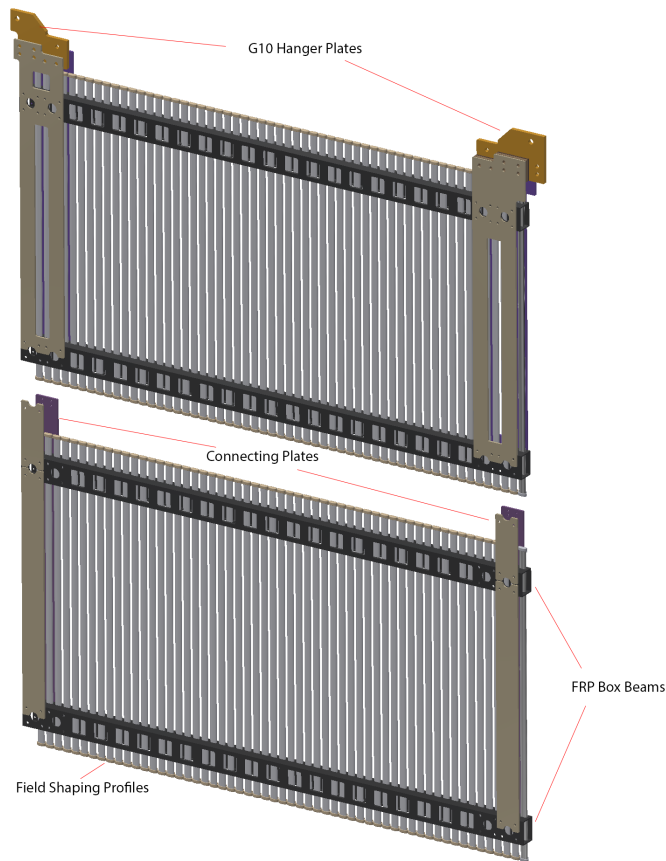


Figure 19: Top: uppermost module of the endwall FC. The two G10 hanger plates connect the endwall FC to the detector support system (DSS) beams above the APAs and CPAs. Bottom: regular endwall FC module. Three of those modules are stacked vertically below a top module, to form the total height of the drift volume.

1212 Voltage Divider Boards and Terminations

1213 A resistive divider chain interconnects all the metal profiles of each FC module to provide a linear
 1214 voltage gradient between the cathode and anode planes.

1215 The resistive divider chain is a chain of resistor divider boards each with eight resistive stages
 1216 in series. Each stage (corresponding to a 6 cm distance between FC profile centers) consists of two
 1217 1 G resistors in parallel yielding a parallel resistance of 0.5 G per stage to hold a nominal voltage
 1218 difference of 3 kV. In the event of a HV breakdown, each stage is protected against HV discharge
 1219 by varistors. Three varistors (with 1.8 kV clamping voltage each) are wired in series and placed
 1220 in parallel with the associated resistors. A photo and schematic of the resistor divider board are
 1221 shown in Figure 21. Each FC divider chain connects to an FC termination board in parallel with
 1222 a grounded fail-safe circuit at the APA end. The FC termination boards are mounted on the top
 1223 of the upper APAs and the bottom of the lower APAs. Each termination board provides a default
 1224 termination resistance, and an SHV cable connection to the outside of the cryostat, via the CE signal
 1225 feedthrough flange, through which it is possible to either supply a different termination voltage to

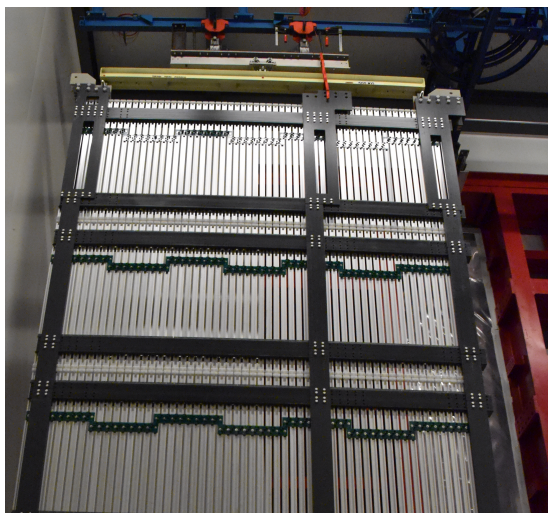


Figure 20: Endwall FC assembly, the stacked modules are visible. The endwall is hung in front of the cryostat before insertion through the TCO. The visible face is the one that will face the inside of the detector active volume. The dark grey FRP plates are the support structure of the endwall and interconnected between the volumes.

1226 the FC or monitor the current flowing through the divider chain, or both.

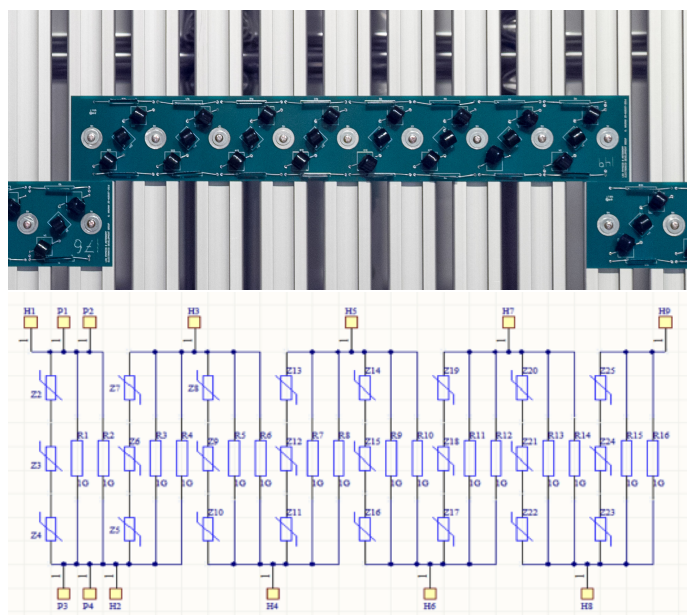


Figure 21: Resistor divider board photograph (top) and schematic (bottom).

1227 4.1.3 Beam Plug

1228 To minimise the material interactions of the particle beam in the cryostat upstream of the TPC, a
 1229 volume of LAr along the beam path (between the cryostat inner membrane and the FC) is displaced,

1230 and replaced by a less dense volume of dry nitrogen gas. The gas is contained within the *beam plug*,
1231 a cylindrical glass-fiber composite pressure vessel, about 50 cm in length and 22 cm in diameter.
1232 It is illustrated in Figure 22. A pressure relief valve and a burst disk are installed on the nitrogen
1233 fill line on the top of the cryostat (externally) to ensure the pressure inside the beam plug does not
1234 exceed the safety level of about 22 psi. The nitrogen system schematic is shown in Figure 23.

1235 The beam plug is secured to the endwall FC support structure as illustrated in Figure 22. Beam
1236 is fed into one of the two available drift volumes of the TPC, the drift volume not receiving beam is
1237 used for cosmic ray studies. The front portion of the beam plug extends 5 cm into the active region
1238 of the TPC through an opening in the FC. The FC support is designed with sufficient strength and
1239 stiffness to support its weight. The total internal volume of the beam plug is about 16 liters.

1240 The requirements on the acceptable leak rate is between 7.8×10^{-5} scc/s and 15.6×10^{-5} scc/s.
1241 This is very conservative and is roughly equivalent to leaking 15% of the nitrogen in the beam plug
1242 over the course of a year. In the worst-case scenario in which all the nitrogen in the beam plug
1243 leaks into the LAr cryostat, the increase in concentration is about 0.1 ppm, which is still a factor
1244 of 10 below the maximum acceptable level, as specified by light-detection requirements. Over the
1245 course of about 1.5 years of beam plug operations in LAr at ProtoDUNE-SP, no detectable leak
1246 was observed.

1247 At nominal operation, the voltage difference across the beam plug (between the first and the
1248 last grading ring) is 165 kV. To minimise risk of electrical discharges, the beam plug is divided into
1249 sections, each of which is bonded to stainless steel conductive grading rings. The seven grading
1250 rings are connected in series with three parallel paths of resistor chains. The ring closest to the FC
1251 is electrically connected to one of the FC profiles. The electrode ring nearest the cryostat wall is
1252 grounded to the cryostat (detector) ground. The maximum total power dissipated by the resistor
1253 chain is about 0.6 W.

1254 **4.1.4 High Voltage (HV) Components**

1255 The TPC high voltage (HV) components include the HV power supply, cables, filter circuit, HV
1256 feedthrough, and monitoring instrumentation for currents and voltages (both steady state and tran-
1257 sient).

1258 The 180 kV voltage necessary to produce the required electric field of 500 V/cm is delivered
1259 by the power supply through an RC filter and a HV feedthrough to the CPA. The design of the HV
1260 feedthrough is based on the reliable construction technique adopted for the ICARUS HV feedthrough
1261 [16] and shown in Figure 24. Before installation, the feedthrough was successfully operated for
1262 several days in a test stand at voltages up to 300 kV.

1263 The feedthrough design has a coaxial geometry, with an inner conductor (HV) and an outer
1264 conductor (ground) insulated by UHMWPE, as illustrated in Figure 24. The outer conductor, a
1265 stainless-steel tube, surrounds the insulator, extending down through the cryostat into the LAr.
1266 In this geometry, the E field is confined within regions occupied by high-dielectric-strength media
1267 (UHMW PE and LAr). The inner conductor is made of a thin-walled stainless steel tube to minimise
1268 the heat input and to avoid the creation of argon gas bubbles around the lower end of the feedthrough.
1269 A contact, welded at the upper end for the connection to the HV cable, and a round-shaped elastic
1270 contact for the connection to the cathode, screwed at the lower end, completes the inner electrode.
1271 Special care has been taken in the assembly to ensure complete filling of the space between the

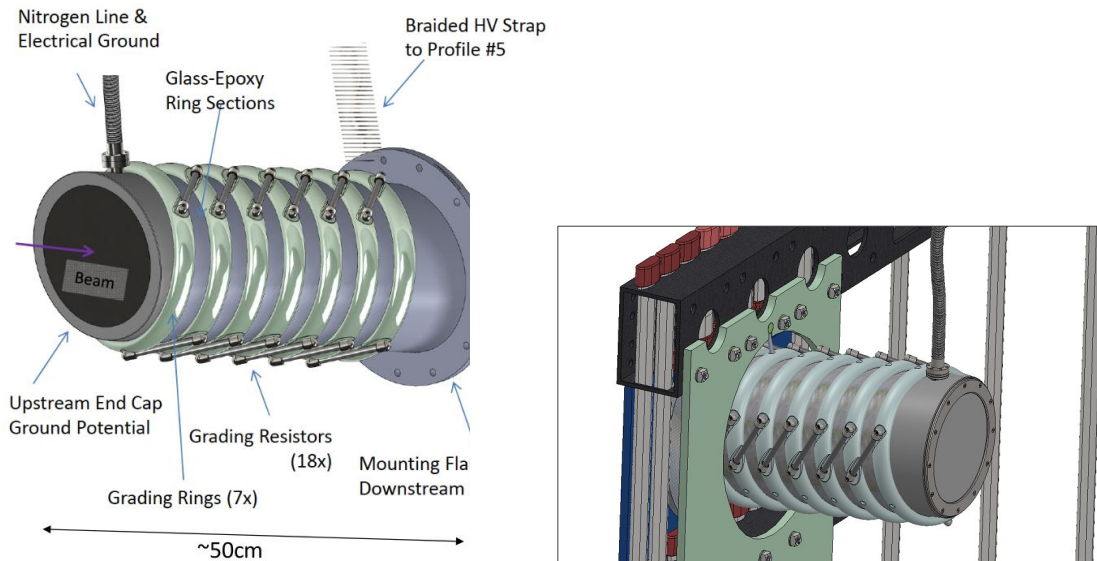


Figure 22: The beam plug is a composite pressure vessel filled with dry nitrogen gas. Left: The vessel is about 50 cm in length and about 22 cm in diameter. The pressure vessel is divided into sections with each section bonded to a stainless steel grading ring. The grading rings are connected by three parallel paths of resistor chain. Right: Beam plug to FC interface.

1272 inner and outer conductors with the (polyethylene) PE dielectric, and to guarantee leak-tightness at
 1273 ultra-high vacuum levels.

1274 Filter resistors are placed between the power supply and the feedthrough. Along with the
 1275 cables, these resistors reduce the discharge impact by partitioning the stored energy in the system.
 1276 The resistors and cables together also serve as a low-pass filter reducing the 30 kHz voltage ripple
 1277 on the output of the power supply.

1278 The filter resistors are of a cylindrical design. Each end of an HV resistor is electrically
 1279 connected to a cable receptacle. A cylindrical insulator is placed around the resistor, and a grounded
 1280 stainless steel tube surrounds the insulator.

1281 The instrumentation in ProtoDUNE-SP provided useful information on HV stability. Outside
 1282 the cryostat, the HV power supply and cable-mounted toroids monitor the HV. The power supply
 1283 has capabilities down to tens of nA in current read-back and is able to sample the current and
 1284 voltage every 300 ms. The cable-mounted toroid is sensitive to fast changes in current; the polarity
 1285 of a toroid's signal indicates the location of the current-drawing feature as either upstream or
 1286 downstream of it.

1287 Inside the cryostat, pick-off points near the anode monitor the current in each resistor chain.
 1288 Additionally, the voltage of the ground planes (GPs) above and below each drift region can diagnose
 1289 problems via a high-value resistor connecting the GP to the cryostat.

1290 HV Commissioning, Beam Time Operation and Stability Runs

1291 During cool-down and LAr filling, a power supply was used to supply 1 kV to the cathode and
 1292 monitor the current draw of the system. As the system cooled from room temperature to LAr

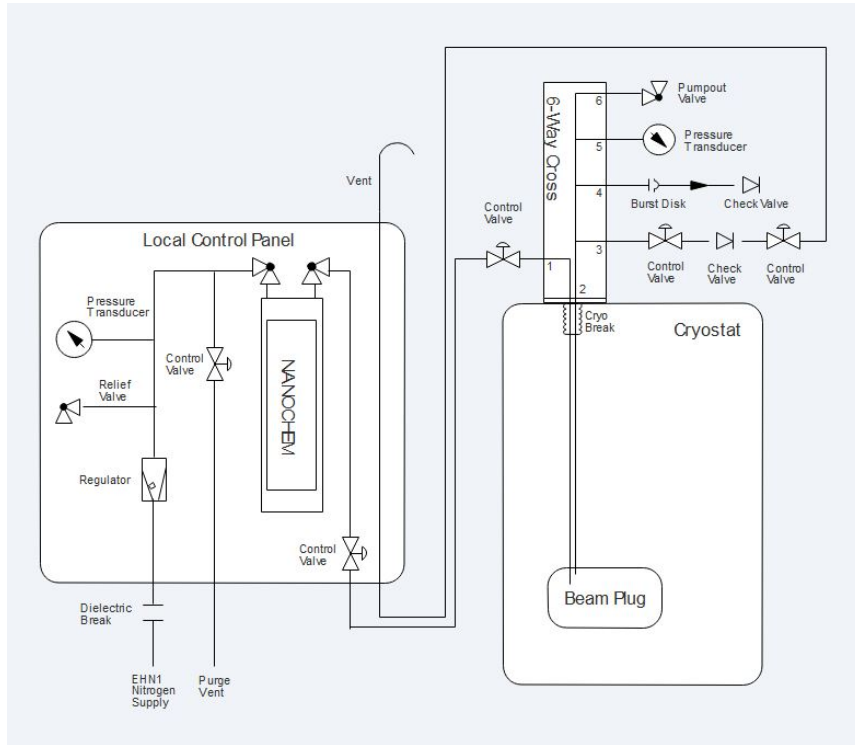


Figure 23: Beam plug nitrogen gas system schematics. The Local Control Panel is mounted on top of the cryostat near the DN160 flange feedthrough. The nitrogen line enters the cryostat via the six-way flange, which also has a burst disk for emergency pressure relief, and temperature/pressure sensors.

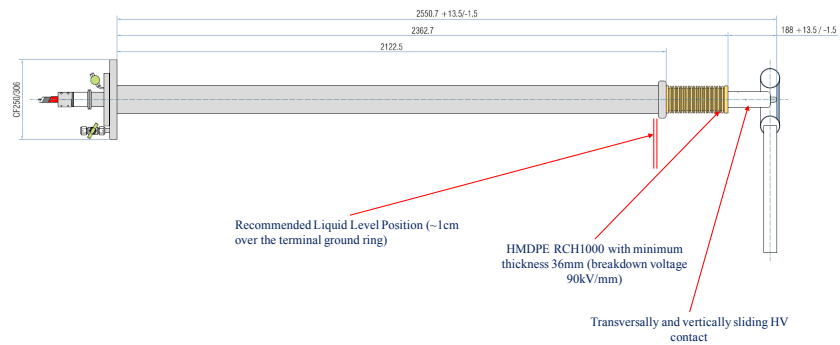


Figure 24: Photograph after installation and drawing of the HV feedthrough. The distance from the cup to the top surface is approximately 1.3 m.

1293 temperature, the resistance increased by 10%, consistent with expectations. Once the LAr level
 1294 had exceeded the height of the top GP, the voltage was ramped up to the nominal voltage.

1295 Two types of instabilities emerged in the cold side of the HV system. The first type was a

1296 so-called current blip, during which the system drew a small excessive current that persisted for
 1297 no more than a few seconds. The magnitude of the excess current during current blips increased
 1298 over the subsequent three weeks from 1% to 20%. The second type of instability, called a “current
 1299 streamer,” exhibited persistent excessive current draw from the HV power supply with accompanying
 1300 excessive current detected on a GP and on the beam plug. These two types of instabilities occurred
 1301 periodically throughout the beam run. The frequency of both types increased over time after the
 1302 system was powered on, until a steady state of about ten current blips/day and one current streamer
 1303 every four hours was reached. These effects are consistent with a slow charging-up process of
 1304 the insulating components of the FC supports, which then experience partial discharges that are
 1305 recorded as HV instabilities. This process restarts after every long HV-off period.

1306 In addition, these processes seemed to be enhanced by the LAr bulk high purity, which allowed
 1307 the electric current to develop. At low purity electronegative impurities acted as quenchers, blocking
 1308 the development of the leakage current. During the 2018 beam run periods, priority was given
 1309 to operating the ProtoDUNE-SP detector with maximal uptime in order to collect as much beam
 1310 data as possible at the nominal HV conditions [17]. In some cases, mostly outside of the beam
 1311 run period, the HV system was turned off momentarily to allow the HV system components to
 1312 discharge. This is reflected as larger dips in the uptime plot shown in Figure 25 [18]. During
 1313 periods when the rest of the subsystems (including the beam) were stable, the moving 12-hour HV
 1314 uptime fluctuated between 96% and 98%. Automated controls to quench the current streamers were
 1315 then successfully implemented in an auto-recovery mode. These helped to increase the uptime
 1316 significantly, by optimising the ramping down and up of the HV power supply voltage, which was
 1317 performed in less than four minutes. The process of the auto-recovery mode is shown in Figure 26.

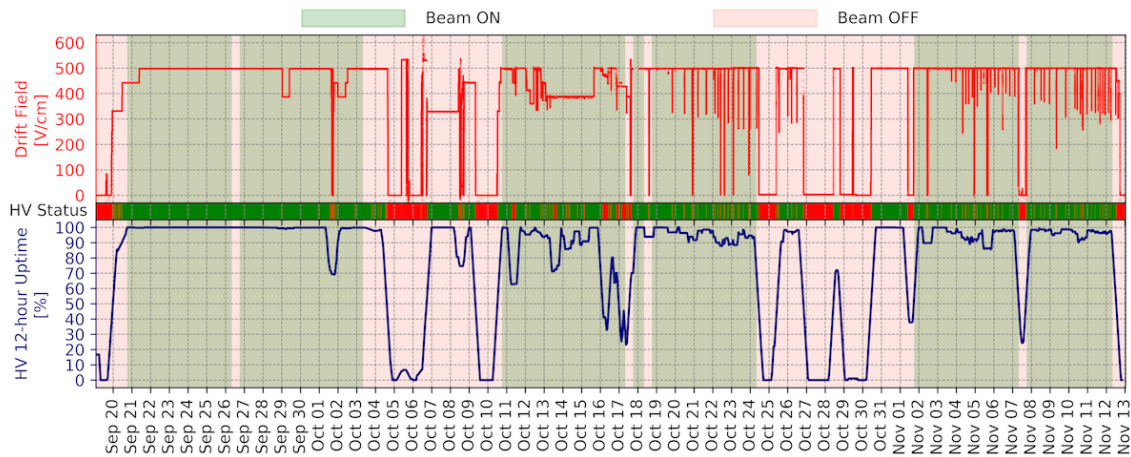


Figure 25: The performance of the HV system across the test beam period, Sep-Nov 2018. The top panel shows the drift field delivered to the TPC; the middle panel indicates HV cuts during periods when the system was not nominal (some periods not visible due to their short timescale); and the bottom panel shows the moving 12-hour uptime of the HV system based on these HV cuts.

1318 Investigating the long-term behaviour of the HV instabilities and understanding their origin
 1319 became goals of the long-term operation of ProtoDUNE-SP in 2019. As mentioned above, it
 1320 appeared that the current-streamer effect is a charging-up process with its frequency increasing

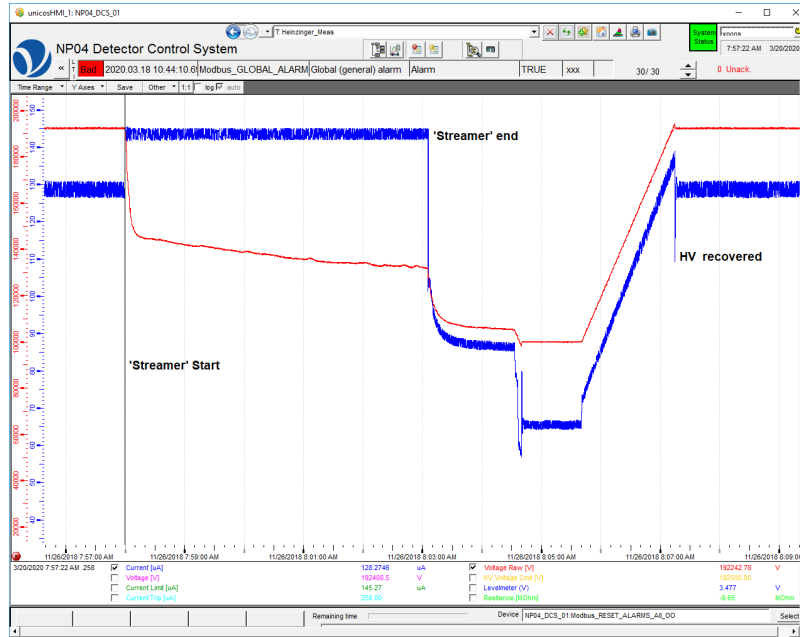


Figure 26: Automatic Recovery of a ‘streamer’ event recorded on 26/11/2018 by DCS. The HV current (in blue) is limited at 142 μA ; the voltage (in red) decreases until the discharge is finished, returning to the nominal voltage after a predefined time.

1321 with time after a long HV-off period. This behaviour was observed repeatedly and this cause was
 1322 confirmed in 2019. The current-streamer rate stabilised at 4-6 events per day, and the location
 1323 remained on the same single ground plane (GP#6). The rate and location were approximately
 1324 independent of the HV applied on the CPA in the 90 kV to 180 kV range.

1325 More recently, after changing the LAr re-circulation pump in April 2019, the detector was
 1326 operated for several months in very stable cryogenic conditions and with very high and stable LAr
 1327 purity (as measured by purity monitors and cosmic rays). During this period, a significant evolution
 1328 was observed. The HV system was set and operated at the nominal value of 180 kV at the CPA for
 1329 several weeks without interruption.

1330 To better understand the current-streamer phenomenon, the HV system was operated for about
 1331 fifty days without the auto-recovery script, and the current streamers were left to evolve naturally.
 1332 They typically lasted six to 12 hours, exhibiting steady current and voltage drawn from the HV
 1333 power supply, and they eventually self-quenched without any intervention. During this period, the
 1334 repetition rate was significantly reduced to about one current streamer every 10-14 days; this rate
 1335 can be compared to the 4-6 per day in the previous periods with auto-recovery on.

1336 The auto-recovery script was then re-enabled and the current-streamer rate stabilised at about
 1337 one in every 20 hours; in addition, the intensity of the current streamer on the GP was reduced with
 1338 respect to the previous periods. As in the previous runs, the current streamers always occurred on
 1339 the same GP (GP#6) with a small leakage current on the beam plug hose, which is close to GP#6.

1340 This behaviour is a further indication that the current streamers were, in fact, a slow discharge
 1341 process of charged-up insulating materials present in the high-field region outside of the FC. The
 1342 auto-recovery mode did not allow a full discharge, so the charging up was faster, and the streamer

1343 repetition rate was shorter.

1344 The LAr purity loss experienced at the end of July 2019 was accompanied by the complete
1345 disappearance of any HV instabilities. They gradually reappeared when the electron lifetime
1346 exceeded 200 microseconds, and their intensity constantly increased as purity improved. This
1347 behaviour replicated that observed after the initial filling, and is consistent with what has been
1348 observed on other similar systems [19], thus supporting the hypothesis that the HV instabilities are
1349 enhanced by the absence of electronegative impurities in high-purity LAr.

1350 The effects of the current streamers on the front-end electronic noise and the PD background
1351 rate were investigated. No effect of the current streamers on the FE electronics was observed. On
1352 the other hand, recent analysis of the data collected by the PDS during active current streamers has
1353 indicated a high single photon rate on the upper upstream part of the TPC. This is consistent with
1354 the activities recorded on GP#6, which is located exactly at this upper upstream area.

1355 4.2 Inner Detector: Anode Plane Assemblies and Front-end Electronics

1356 4.2.1 Anode Plane Assemblies (APA)

1357 Anode Plane Assemblies (APAs) are the detector elements used to detect ionization electrons
 1358 created by charged particles traversing the LAr volume inside the ProtoDUNE-SP TPC. There are
 1359 two APA arrays, one on the outer side of each of the two drift volumes. Each array comprises three
 1360 APAs (6.3 m tall, 2.3 m wide, 0.12 m thick) hung vertically and adjacent to each other. Each APA
 1361 has layers of sense and shielding wires wrapped around a framework of lightweight, rectangular
 1362 stainless steel tubing, as shown in Figure 27. The sense wire readout is performed by cold electronics
 1363 (CE) attached at the upper end (head) of each APA.

1364 The APAs are designed and built to address the physics performance specifications listed in
 1365 Table 3, which are defined to ensure high-efficiency event reconstruction throughout the entire
 active volume of the LArTPC.

Specifications	Value
MIP identification	100% efficiency
Charge reconstruction	> 90% efficiency for > 100 MeV
Vertex resolution (, ,)	1.5 cm, 1.5 cm, 1.5 cm
Particle identification	
Muon momentum resolution	< 18% for non-contained, < 5% for contained
Muon angular resolution	< 1
Stopping hadron energy resolution	1-5%
Shower identification	
Electron efficiency	> 90%
Photon mis-identification	< 1%
Electron angular resolution	< 1
Electron energy scale uncertainty	< 5%

Table 3: Physics requirements that motivate APA design parameters.

1366
 1367 Identifying minimum-ionizing particles (MIPs) is a function of several detector parameters,
 1368 including argon purity, drift distance, diffusion, APA sense-wire pitch, and equivalent noise charge
 1369 (ENC). It is required that MIPs originating anywhere inside the active volume of the detector be
 1370 reconstructed with 100% efficiency. The choice of wire pitch combined with the other high-level
 1371 parameter values, listed in Table 4, is expected to enable this efficiency and provide good tracking
 1372 resolution and good granularity for particle identification.

1373 The specified vertex resolution of 1.5 cm along each coordinate direction follows from a
 1374 requirement that it be possible to determine the fiducial volume to 1%. The chosen wire pitch
 1375 achieves this for the x and y coordinates. The resolution on z , the drift coordinate, will be higher
 1376 than in the x - y plane due to the combination of drift velocity and electronics sampling rate.

1377 In the construction of an APA, the frame is first covered on both sides with a fine mesh that
 1378 defines a uniform ground across the frame. Along the length of the frame and around it, over the
 1379 mesh layer, layers of sense and shielding wires are strung at carefully selected angles relative to

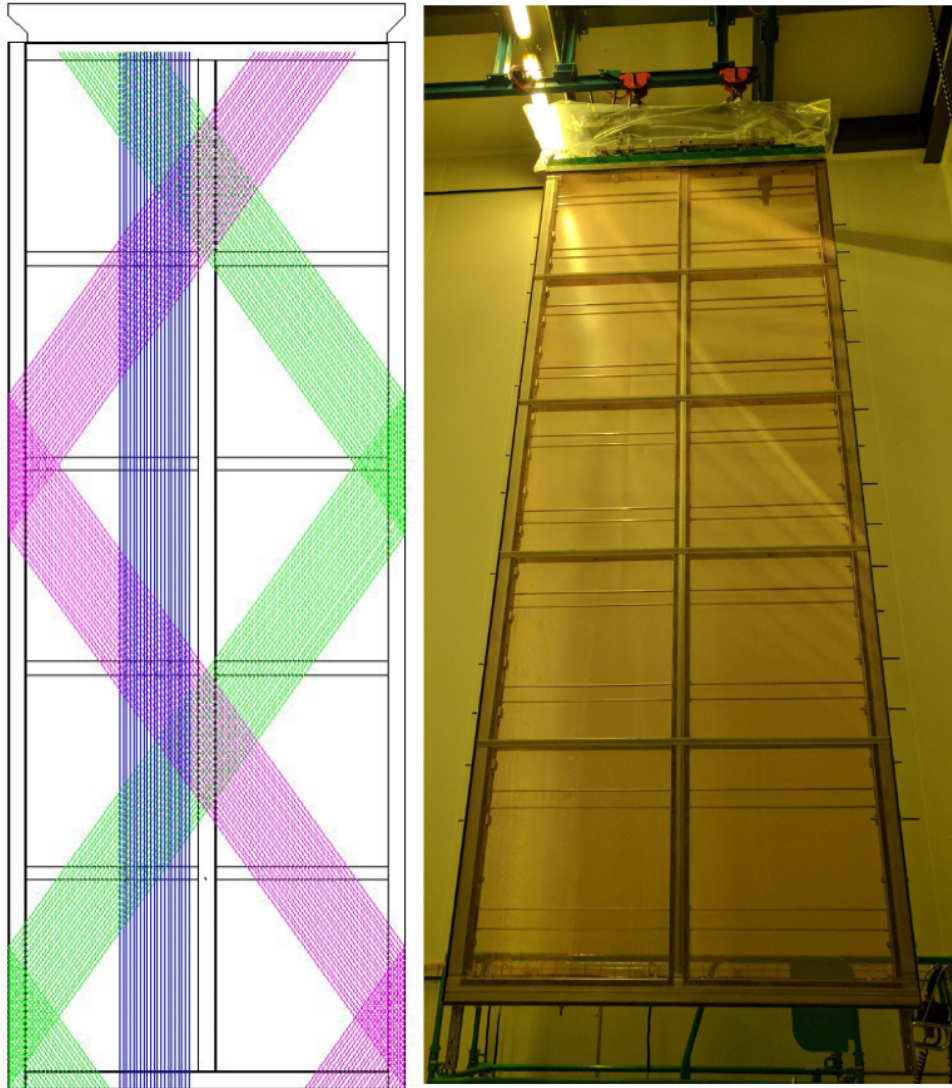


Figure 27: Left: Sketch of a ProtoDUNE-SP APA showing portions of the wire layers: the induction layers U (green) and V (magenta); and the collection layer X (blue). Only portions are shown to accentuate their angular relationships to the frame and to each other. The induction layers are connected electrically across both sides of the APA. The grid layer (G) wires (not shown), run vertically, parallel to the X layer wires; separate sets of G and X wires are strung on the two sides of the APA; they are not wrapped. The mesh is not shown. Right: Assembled APA hanging inside the clean room next to the ProtoDUNE-SP cryostat at CERN.

1380 each other. The wires are terminated on boards that both anchor them and provide the connections
 1381 to the CE.

1382 The grid plane wires (G) are not connected to the electronic readout. Separate sets of grid
 1383 wires run along each side of the APA, parallel to its long edge. The two planes of induction wires
 1384 (U and V) wrap continuously around both sides of the APA in a helical fashion. The collection
 1385 plane wires (X) run vertically, parallel to the grid wires. The ordering of the layers, from the outside

Parameter	Value
Active Height	5.984 m
Active Width	2.300 m
Wire Pitch (U,V)	4.669 mm
Wire Pitch (X,G)	4.790 mm
Wire Position Tolerance	0.5 mm
Wire Plane Spacing	4.75 mm
Wire Angle (w.r.t. vertical) (U,V)	35.7
Wire Angle (w.r.t. vertical) (X,G)	0
Number Wires / APA	960 (X), 960 (G), 800 (U), 800 (V)
Number Electronic Channels / APA	2560
Wire Tension	5.0 N
Wire Material	Beryllium Copper
Wire Diameter	150 μ m
Wire Resistivity	7.68 $\mu\Omega$ /cm @ 20 C
Wire Resistance/m	4.4 $\mu\Omega$ /m @ 20 C
Frame Planarity	5 mm
Photon Detector Slots	10

Table 4: APA design parameters.

1386 in, is G-U-V-X, with the mesh layer at the centre. All wire layers span the entire face on both sides
1387 of the APA frame.

1388 The angle of the induction planes in the APA (35.7) was chosen such that each induction
1389 wire only crosses a given collection wire one time, reducing the ambiguities that the reconstruction
1390 must address. Coupled with the wire pitch, this angle makes it possible for an integer multiple of
1391 electronics boards to read out one APA.

1392 The operating voltages of the APA layers are listed in Table 5. When operated at these
1393 voltages, the drifting ionization follows trajectories around the grid and induction wires, ultimately
1394 terminating on a collection plane wire; i.e., the grid and induction layers are completely transparent
1395 to drifting ionization, and the collection plane is completely opaque. The grid layer is present for
1396 pulse-shaping purposes, effectively shielding the first induction plane from the drifting charge and
1397 removing the long leading edge from the signals on that layer. The mesh layer serves to shield the
1398 sense planes from pickup from the PDS.

APA layer	Bias voltage
Grid (G)	665 V
Induction (U)	370 V
Induction (V)	0 V
Collection (X)	820 V
Mesh (M)	0 V

Table 5: Bias voltages for APA wire planes and mesh.

1399 The wrapped configuration allows the APA array to fully cover the active area of the LArTPC,
1400 minimizing the amount of dead space between the APAs that would otherwise be occupied by
1401 electronics and associated cabling.

1402 The current design of the DUNE-SP far detector module implements three APA arrays that run
1403 the 60 m length of the TPC. One runs down the centre of the detector, the other two are installed
1404 along the outer walls, and two CPA arrays are interleaved between them, creating a set of four
1405 drift fields. The central APA array, flanked by drift fields, requires sensitivity on both sides, which
1406 the wrapped induction-plane wire design enables. Whereas this double-sided feature is not strictly
1407 necessary for the ProtoDUNE-SP arrangement, in which only the inner side of each APA faces a
1408 drift field, it is compatible with this setup, as the grid layer on the wall side effectively blocks any
1409 ionization generated outside the TPC from drifting in to the sense wires.

1410 The APAs are wound with 150 μ m (.006 in) diameter beryllium copper (CuBe) wire (98%
1411 copper, 1.9% beryllium), used for its high durability and yield strength. The X- and G-plane
1412 wires extend the full 6 m length of the APA and are not wrapped. The diagonal, wrapped wires
1413 (U and V planes) extend 3.9 m across each face of the APA. To prevent deflection from gravity,
1414 electrostatic forces, and liquid drag from any moving LAr, a set of *combs* supports these wires at
1415 regular intervals along the length of the APA, keeping the longest unsupported wire length under
1416 1.6 m. The combs are slotted pieces of 0.5 mm thick G10, mounted on each of the frame's four
1417 cross braces. The wires are held at a tension of 5 N.

1418 The wire tension and wire placement accuracy specifications ensure that the wires are held taut
1419 in place with no sag. Wire sag can impact both the precision of reconstruction and the transparency
1420 of the TPC. The tension of 5 N is low enough that as the wires contract during cool-down, they stay
1421 safely below the vendor-tested 25.6 N breaking tension value.

1422 All APA wires are terminated on stacked wire boards, installed at the head end of each APA
1423 to provide the connections to the CE, as shown in Figure 28. The APA has ten adjacent sets of
1424 these board stacks on each side rather than one long stack spanning the entire width. Within each
1425 stack, one board corresponds to one wire plane. Attachment of the wire boards begins with the
1426 (innermost) X wire plane to the lowest board in the stack. These wires are strung top to bottom
1427 along each side of the APA frame, soldered, epoxied to connections on the board, and trimmed.
1428 As each subsequent layer is applied, its wires are attached to the next highest wire board layer.
1429 Mill-Max pins and sockets provide the electrical connections between the circuit boards within a
1430 stack.

1431 The wire boards for the X and G planes accommodate 48 wires each, and those for the U and
1432 V planes accommodate 40 each. Each board stack, therefore, has 176 wires, but only 128 signal
1433 channels since the G wires are not read out. The total of 20 stacks per APA results in 2,560 signal
1434 channels and a total of 3,520 wires starting at the top of the APA and ending at the bottom. Each
1435 APA holds a total of 23.4 km of wire. Figure 29 depicts the connections between the different
1436 elements of the APA electrical circuit.

1437 At the head end of the APA, the 4.75 mm wire-plane spacing is set by the thickness of these
1438 wire boards. The first plane's wires solder to the surface of the first board, the second plane's wires
1439 to the surface of the second board, and so on. For installation, temporary toothed-edge boards
1440 beyond these wire boards are used to align and hold the wires until they are soldered to pads on the
1441 wire boards. After soldering, the extra wire is snipped off.

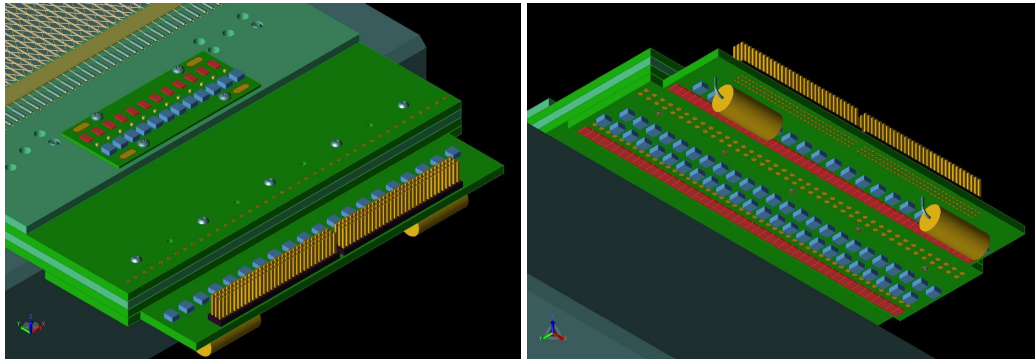


Figure 28: Views of an APA wire-board stack from above (left) and below (right). The X plane wire board is the lowest in the stack. The left image shows the main capacitive-resistive (CR) board connected to the X plane board as it extends beyond the stack. V and U plane boards are attached to the X plane board using Mill-Max pins. The G plane board (outermost and extending less far) is glued on to the board stack of U, V, X, planes. The G plane has its own CR board that is attached as shown in the left figure.

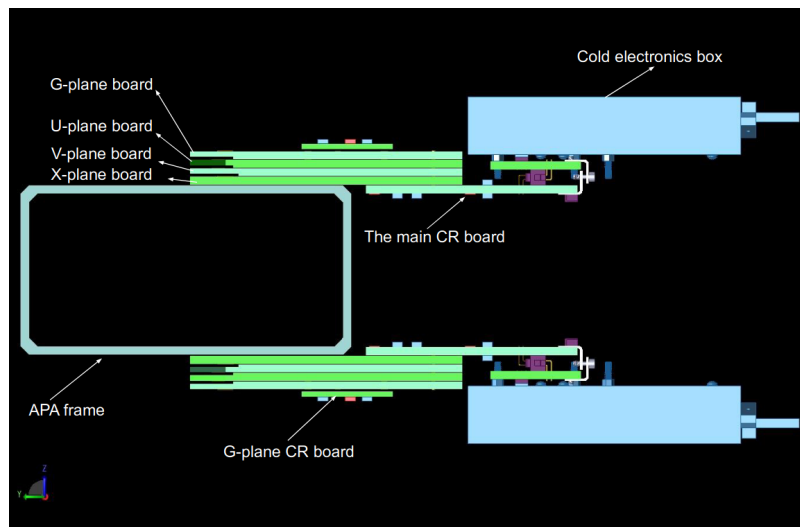


Figure 29: Connections between the APA wires, viewed from the APA edge. The symmetric set of wire boards within a stack can be seen on both sides of the APA, with the CR board extending further to the right. The CR board provides a connection to the CE housed in the boxes at the far right of the figure.

1442 Attached to the wire board stack, capacitive-resistive (CR) boards provide DC bias and AC
 1443 coupling to the wires. The CR boards carry a bias resistor ($51\text{ M}\Omega$) and a DC-blocking capacitor
 1444 (3900 pF) for each wire in the X and U planes. Connections from the CR boards to the CE are
 1445 made through a pair of 96-pin Samtec connectors. In the case of the outermost G plane, wire boards
 1446 connect adjacent groups of four wires together and bias each group through an RC filter whose
 1447 components are placed on special G plane CR boards. All CR boards are attached to the board
 1448 stacks after fabrication of all wire planes.

1449 Pins extending outward from the CR boards provide connections from the APA to the modularly
1450 designed CE. Each board stack has one CE module connected to it. Each CE module is housed in a
1451 small metallic enclosure called a CE box that provides electrical shielding and mechanical support,
1452 simplifies installation and replacement, and helps with the dissipation of argon gas generated by the
1453 warm electronic components. The CE modules are mounted in such a way that any of them can be
1454 removed from the inner side of the APA after APA installation. Figure 30 illustrates the CE boxes
1455 and their installation in ProtoDUNE-SP.

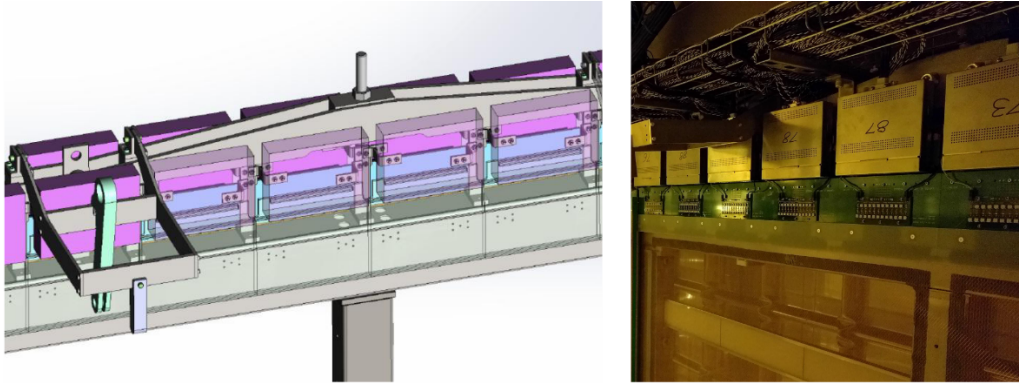


Figure 30: 3D model of modular CE boxes (left). A set of CE boxes installed on an APA in ProtoDUNE-SP (right).

1456 4.2.2 TPC Front-end Cold Electronics (CE)

1457 The ProtoDUNE-SP TPC read-out electronics are referred to as “cold electronics (CE)” because
1458 the system resides in the LAr, mounted directly on the APA, thus reducing channel capacitance
1459 and noise by minimising the length of the connection between an anode wire and its corresponding
1460 electronics input.

1461 The CE signal processing is implemented in ASIC chips using CMOS technology, which has
1462 been demonstrated to perform well at cryogenic temperatures, and includes amplification, shaping,
1463 digitisation, buffering, and multiplexing (MUX) of the signals. The CE is continuously read out,
1464 resulting in a digitised ADC sampling from each APA channel (wire) at a rate of up to every 500 ns
1465 (2 MHz maximum sampling rate).

1466 The 2,560 channels from each APA are read out by 20 front-end motherboards (FEMBs), each
1467 providing digitised wire readout from 128 channels. One cable bundle connects each FEMB to the
1468 outside of the cryostat via a CE feedthrough in the signal cable flange at the top of the cryostat,
1469 where a single flange services each APA. Each cable bundle contains wires for low-voltage (LV)
1470 power, high-speed data readout, and clock/digital-control signal distribution. In addition to the CE
1471 cables, eight separate cables carry the TPC wire-bias and FC termination voltages from the signal
1472 flange to the APA wire-bias boards as shown schematically in Figure 31.

1473 The main component of the CE architecture, illustrated in Figure 32, is the 128-channel
1474 FEMB, which itself consists of an analogue motherboard and an attached FPGA mezzanine card
1475 for processing the digital outputs. Each APA is instrumented with 20 FEMBs, for a total of 2,560

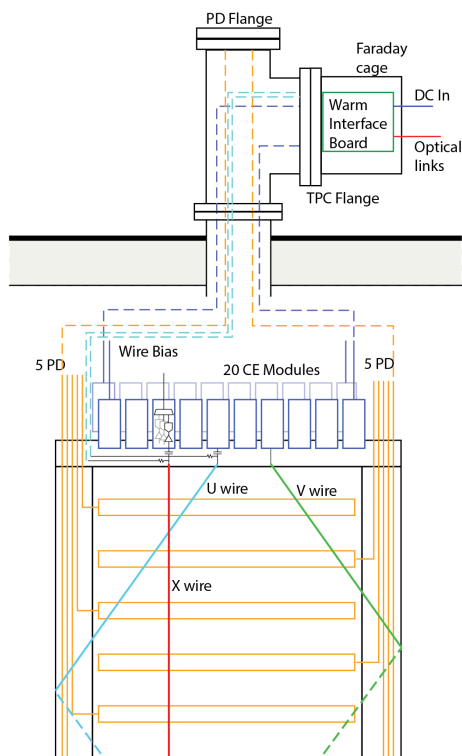


Figure 31: Power and readout cable connection between the APA and signal flange on the cryostat. The orange cables represent photon detector connections, the turquoise lines represent wire biases and field cage (FC) terminations and blue lines represent power and readout cables for the CE.

1476 channels per APA. The FEMBs plug directly into the APA CR boards, making the connections from
 1477 the U, V, and X plane wires to the charge amplifier circuits as short as possible.

1478 The analogue mother board is instrumented with eight 16-channel FE ASICs, eight 16-channel
 1479 ADC ASICs, LV power regulators, and input-signal protection circuits. The 16-channel FE ASIC
 1480 provides amplification and pulse shaping. The 16-channel ADC ASIC comprises 12-bit digitisers
 1481 performing at speeds up to 2 MS/s, local buffering, and an 8:1 MUX stage with two pairs of serial
 1482 readout lines in parallel. Figure 33 shows the analog motherboard, the FPGA mezzanine, and the
 1483 complete FEMB assembly.

1484 Each FE ASIC channel has a charge amplifier circuit with a programmable gain, selectable
 1485 from 4.7, 7.8, 14, and 25 mV/fC (full-scale charge of 55, 100, 180 and 300 fC), a high-order anti-
 1486 aliasing filter with programmable time constant (peaking time 0.5, 1, 2, and 3 μ s), an option to
 1487 enable AC coupling, and a baseline adjustment for operation with either the collecting (200 mV)
 1488 or the non-collecting (900 mV) wires. Shared among the 16 channels in the FE ASIC are the bias
 1489 circuits, programming registers, a temperature monitor, an analog buffer for signal monitoring, and
 1490 the digital interface. The FE ASIC's estimated power dissipation is about 6 mW per channel at
 1491 1.8 V supply.

1492 The FE ASIC was implemented using the commercial CMOS process (0.18 μ m and 1.8 V),
 1493 which is expected to be available for at least another ten years. The charge amplifier input MOSFET
 1494 is a p-channel biased at 2 mA with a L/W (channel length/width) ratio of 0.27 μ m / 10 μ m, followed

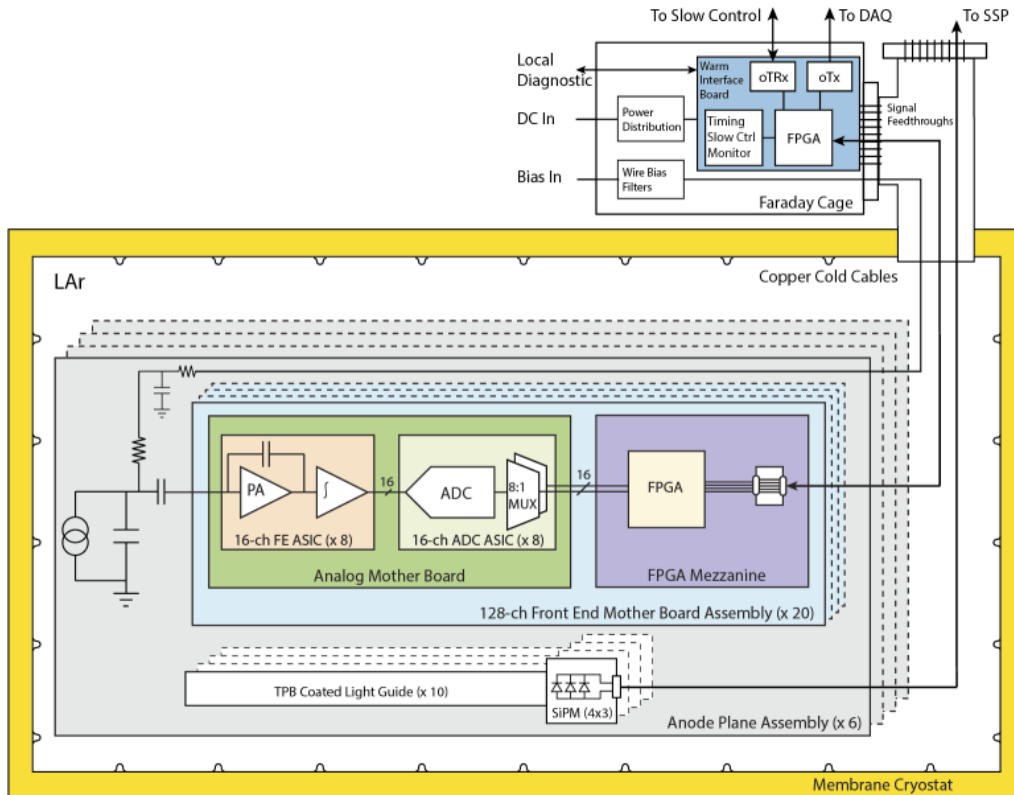


Figure 32: The CE architecture. The basic unit is the 128-channel FEMB.

1495 by dual cascade stages.

1496 Each FE ASIC channel is equipped with an injection capacitor that can be used for testing and
 1497 calibration and is enabled or disabled through a dedicated register. The injection capacitance has
 1498 been measured using a calibrated external capacitor. The measurements show that the calibration
 1499 capacitance is extremely stable, changing from 184 fF at room temperature to 183 fF at 77 K. This
 1500 result and the measured stability of the peaking time demonstrate the high stability of the passive
 1501 components as a function of temperature. Channel-to-channel and chip-to-chip variation in the
 1502 calibration capacitor is typically less than 1%.

1503 The ADC ASIC design is also implemented using the CMOS process (0.18 μm and 1.8 V).
 1504 The ADC ASIC is a complex design with 320,000 transistors, while the FE ASIC has 16,000. The
 1505 transistor design work has been done following the rules for long cryogenic lifetime. Shared among
 1506 the 16 channels in the ADC ASIC are the bias circuits, programming registers, an 8:1 MUX, and
 1507 the digital interface. The estimated power dissipation of ADC ASIC is below 5 mW per channel at
 1508 1.8 V supply.

1509 The ADC ASIC data are passed to the FPGA mezzanine board for transmission to the warm
 1510 electronics located on the outside of the signal flange. The FPGA has four 4:1 MUX circuits that
 1511 combine the 16 serial lines from the eight ADC channels into four serial lines of 32 channels
 1512 each, and four 1.2 Gigabit-per-second (Gbps) serial drivers that drive the data in each line over
 1513 cold cables to the warm interface electronics (WIBs). The FPGA on the mezzanine card is also

1514 responsible for communicating with the control and timing systems from the WIB and providing
1515 the clock and control signals required by the FE and ADC ASICs.

1516 The FPGA and all other electrical components on the FEMB assembly has been evaluated
1517 and characterised at RT (300 K) and LN2 (77 K) temperature. During these tests the FEMB has
1518 been temperature-cycled multiple times. In addition, power-cycle tests at cryogenic temperature
1519 have been performed. Figure 34 shows the measured ENC as a function of filter-time constant
1520 (peaking time) for two different gains as measured on a prototype FEMB. ENC is the value of
1521 charge (in electrons) injected across the detector capacitance that would produce at the output of
1522 the shaping amplifier a signal whose amplitude equals the output RMS noise. These measurements
1523 were made with the prototype FEMB at both RT and submerged in LN2 with a wire-simulating
1524 input capacitance of 150 pF (equivalent to an approximately 7 m sense wire load). In
1525 LN2, for peaking times $1 \mu\text{s}$, less than 600 e⁻ was measured. For comparison, a MIP travelling
1526 perpendicularly to the wire plane in the direction of wire spacing is expected to deposit at least
1527 10,000 e⁻ on the collection wires, for a worst-case SNR is about 16 to 1³. One of the key
1528 ingredients to achieving a low-level noise performance is the grounding of the experimental setup.
1529 The details of the ProtoDUNE-SP grounding scheme and methods to ensure a low noise level are
1530 discussed in Section 5.4

1531 As mentioned in Section 4.2.1, each FEMB is enclosed in a Faraday box, called a CE box,
1532 that provides shielding from noise. As shown in Figure 35, it provides the electrical connection
1533 between the FEMB and the APA frame. Mounting hardware inside the CE box connects the ground
1534 plane of the FEMB to the box casing, which is electrically connected to the APA frame via twisted
1535 conducting wire. This is the only point of contact between the FEMB and APA, except for the input
1536 amplifier circuits connected to the CR board, which also terminate to ground at the APA frame.

1537 4.2.3 TPC Front-end Warm Electronics

1538 The warm interface electronics are housed in warm interface electronics crates (WIECs) attached
1539 directly to the signal flange. The WIEC shown in Figure 36 contains one power and timing card
1540 (PTC), up to five warm interface boards (WIBs) and a passive power and timing backplane (PTB),
1541 which fans out signals and LV power from the PTC to the WIBs.

1542 The WIB is the interface between the DAQ system and up to four FEMBs. It receives the
1543 system clock and control signals from the timing system and provides for processing and fan-out of
1544 those signals to the four FEMBs. The WIB also receives the high-speed data signals from the four
1545 FEMBs and transmits them to the DAQ system over optical fibres. The WIBs are attached directly
1546 to the TPC CE feedthrough on the signal flange. The feedthrough board is a PCB with connectors
1547 to the cold signal and LV power cables fitted between the compression plate on the cold side, and
1548 sockets for the WIB on the warm side. Strain relief for the cold cables is supported from the back
1549 end of the feedthrough.

1550 The PTC provides a bidirectional fibre interface to the timing system. The clock and data
1551 streams are separately fanned-out to the five WIBs. The PTC fans the clocks out to the WIB over
1552 the PTB, which is a passive backplane attached directly to the PTC and WIBs. The received clock
1553 on the WIB is separated into clock and data using a clock/data separator. The PTC also receives

³For the minimum performance requirements of 500 V/cm and a 3 ms electron lifetime

1554 LV power for all CE connected through the signal flange, approximately 250 W at 48 V for a fully-
1555 loaded flange (one PTC, five WIB, and 20 FEMB). The LV power is then stepped down to 12 V via
1556 a DC/DC converter on-board the PTC and fanned out on the PTB to each WIB, which provides the
1557 necessary 12 V DC/DC conversions and fans the LV power out to each of the cold FEMBs supplied
1558 by that WIB, as shown in Figure 37. The majority of the 250 W drawn by a full flange is dissipated
1559 in the LAr by the cold FEMB.

1560 Each WIB contains a unique IP address for its UDP (User Datagram Protocol) slow control
1561 interface. In addition, the WIB is capable of receiving the encoded system-timing signals over bi-
1562 directional optical fibres on the front panel, and processing these using either the on-board FPGA
1563 or clock synthesizer chip to provide the 50 MHz clock required by the CE.

1564 The FPGA on the WIB is an Altera Arria V GT variant, which requires a 125 MHz clock for
1565 its state machine that is provided by an on-board crystal oscillator. It can drive the high-speed data
1566 to the DAQ system up to 10.3125 Gbps per link, implying that all data from two FEMB (2 5 Gbps)
1567 could be transmitted on a single link. On top of that, the FPGA has an additional Gbps Ethernet
1568 transceiver I/O based on the 125 MHz clock, which provides real-time digital data readout to the
1569 slow control system as well.



Figure 33: The Front End Mother Board (FEMB). Top: The analogue mother board, showing four ADC ASICs and four FE ASICs, surface mounted. The other side of the board has another four ADC and FE ASICs. Middle: The FPGA mezzanine. Bottom: The complete FEMB assembly. The cable shown is the high-speed data, clock, and control cable.

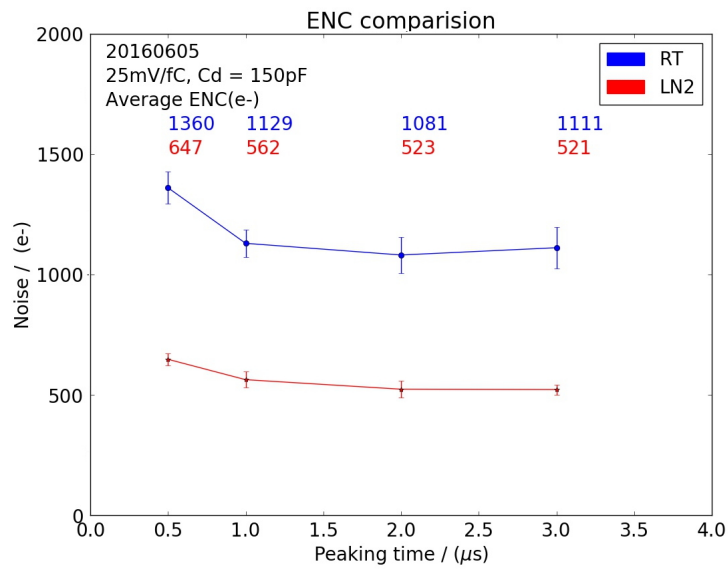
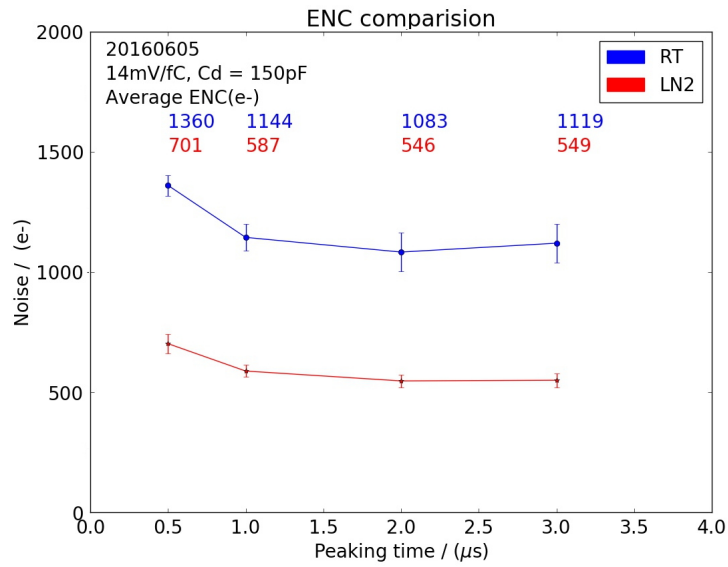


Figure 34: Measured ENC vs filter time constant from the latest prototype version of the FEMB for two different gains, 14 mV/fC and 25 mV/fC. In the legend RT refers to room temperature measurements and LN2 refers to measurements made in liquid nitrogen.

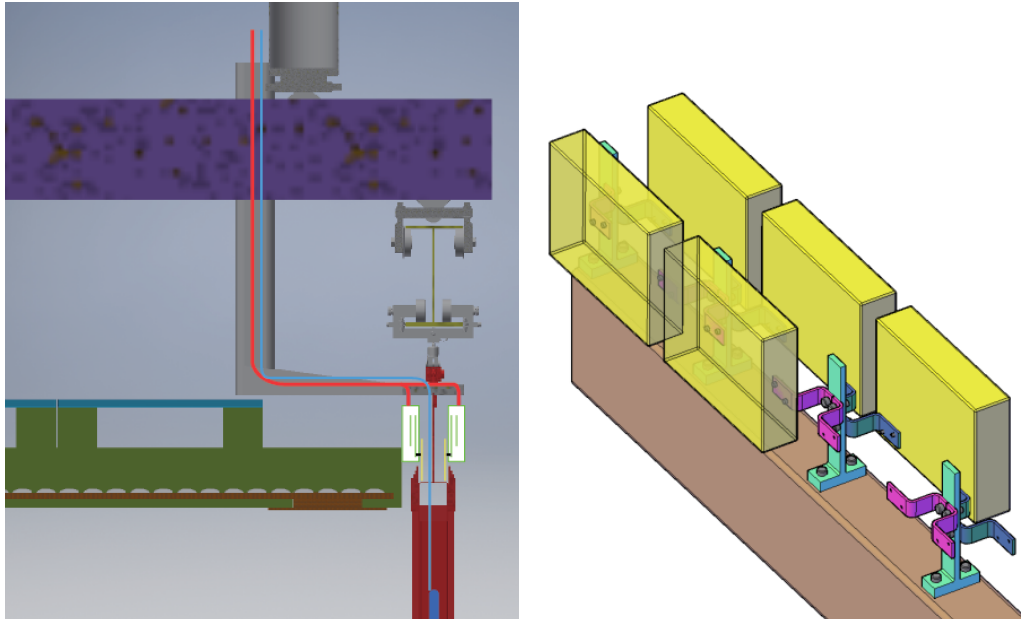


Figure 35: Left: cable routing from CE box to signal flange on the cryostat. Right: CE box (yellow) for the FEMB.

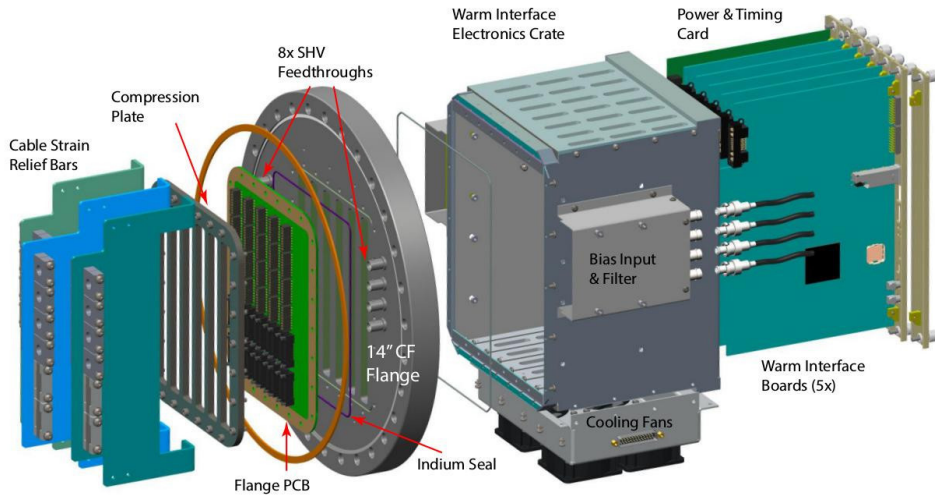


Figure 36: Exploded view of the ProtoDUNE-SP signal flange.

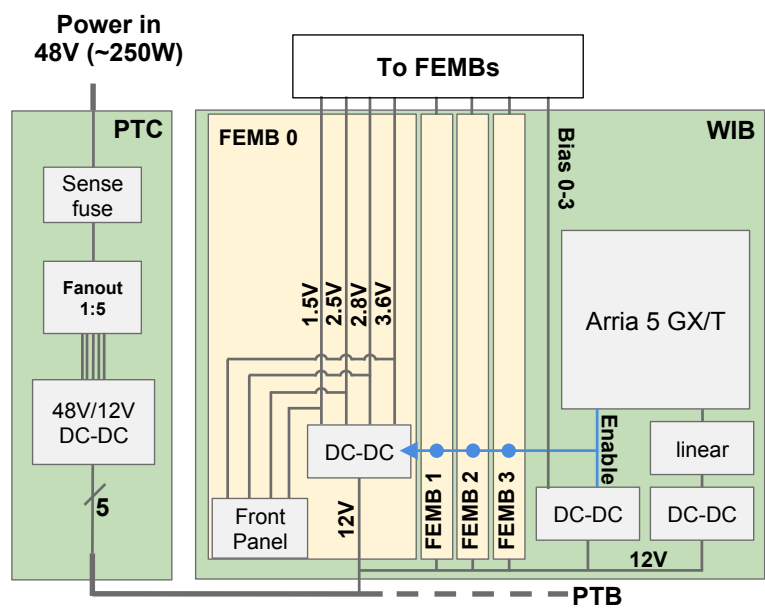


Figure 37: LV power distribution to the WIB and FEMBs. Power of 250 W is for a fully-loaded crate with the majority of the power dissipated by the 20 cold FEMBs in the LAr.

1570 4.3 Inner Detector: Photon Detection System

1571 The Photon Detection System (PDS) in the DUNE FD is critical for the DUNE physics program
1572 and the ProtoDUNE PDS serves as a prototype for the DUNE FD PDS system. The topology and
1573 particle trajectories for events produced by accelerator neutrinos can be reconstructed in the TPC
1574 using charge signals with drift times referenced to the accelerator clock. However, the observation of
1575 potential nucleon decay or neutrinos from supernova bursts and other cosmological sources require
1576 additional timing information. To make these observations, the PDS must have large acceptance
1577 for light in each of the 12 m 14 m 58.2 m 17 kt FD modules and a timing resolution that
1578 localises beam and self-triggered TPC events to mm-scale resolution; it must exist within the design
1579 constraints of the TPC without affecting its operation; and the entire system must be implemented so
1580 as to minimise cost while maximising light detection efficiency. These requirements translate to a
1581 minimum photon yield of at least 0.5 PE/MeV at a maximum drift distance of 3.6 m and a minimum
1582 timing resolution of 100 ns. The PDS in ProtoDUNE-SP demonstrates that current designs satisfy
1583 all of these requirements and, with some revisions, will satisfy the physics goals of the DUNE FD.

1584 The PDS obtains event and timing information from the photons produced by LAr scintillation
1585 as particles traverse the detector. LAr is highly transparent to its scintillated light, producing
1586 photons at 128 nm with a Rayleigh scattering length of about 90 cm and an absorption length that
1587 is entirely dependent on the presence of impurities [20, 21]. Minimum ionising particles generate
1588 about 50,000 photons per MeV of deposited energy, but fewer photons are produced in the presence
1589 of electric fields due to the reduction of electron-ion recombination. At the nominal 500 V/cm
1590 field strength in ProtoDUNE-SP, the photon yield is about 24,000 photons per MeV. Roughly a
1591 quarter of the photons produced are promptly emitted through singlet configuration decay of excited
1592 argon dimers; the remaining light is emitted with a lifetime of approximately 1.3 ns from the triplet
1593 configuration [22]. The measurement of prompt photons produced in LAr scintillation serves to
1594 temporally and spatially localise relevant events, by setting a “ t_0 ” for each event.

1595 The PDS is made up of modules, each combining a photon collector and a photon sensor.
1596 ProtoDUNE-SP implemented 60 modules using three different module designs, “double-shift light
1597 guides” (29), “dip-coated light guides” (29), and “ARAPUCA” light traps (2). The designs share a
1598 common low-profile elongated rectangular shape for insertion into slots in the APA frames, to sit
1599 between the APA’s two sets of wire planes. All modules have the same external dimensions and
1600 mounting system. Ten PD modules were inserted into each APA, regularly spaced in the vertical
1601 dimension of each of the six APAs. This configuration maximises the detection efficiency of the PDS
1602 without affecting the operation of the TPC. The module dimensions, 2.3 cm 11.8 cm 20.97 cm,
1603 are dictated by the need to mount them in the APA frames without impairing the mechanical stability
1604 or useful fiducial volume of the TPC. The active area of each PD module is 1744 cm² for both types
1605 of light guides, and 1223 cm² for the ARAPUCA bars, for a total coverage of about 12.5% of the
1606 APA surface. PD placement in an APA frame along with examples of all three types of detector
1607 technologies are shown in Figure 38.

1608 Signals for the PDS system are routed directly to 24 instances of an electronic readout system,
1609 called a SiPM Signal Processor (SSP), all of which independently synchronize and interface directly
1610 with the ProtoDUNE-SP data acquisition (DAQ) system. A pair of standalone UV LED calibration
1611 systems, called Light Calibration Modules (LCMs), are used to precisely determine photosensor

calibration, timing resolution, and to observe the long-term stability in the PDS.

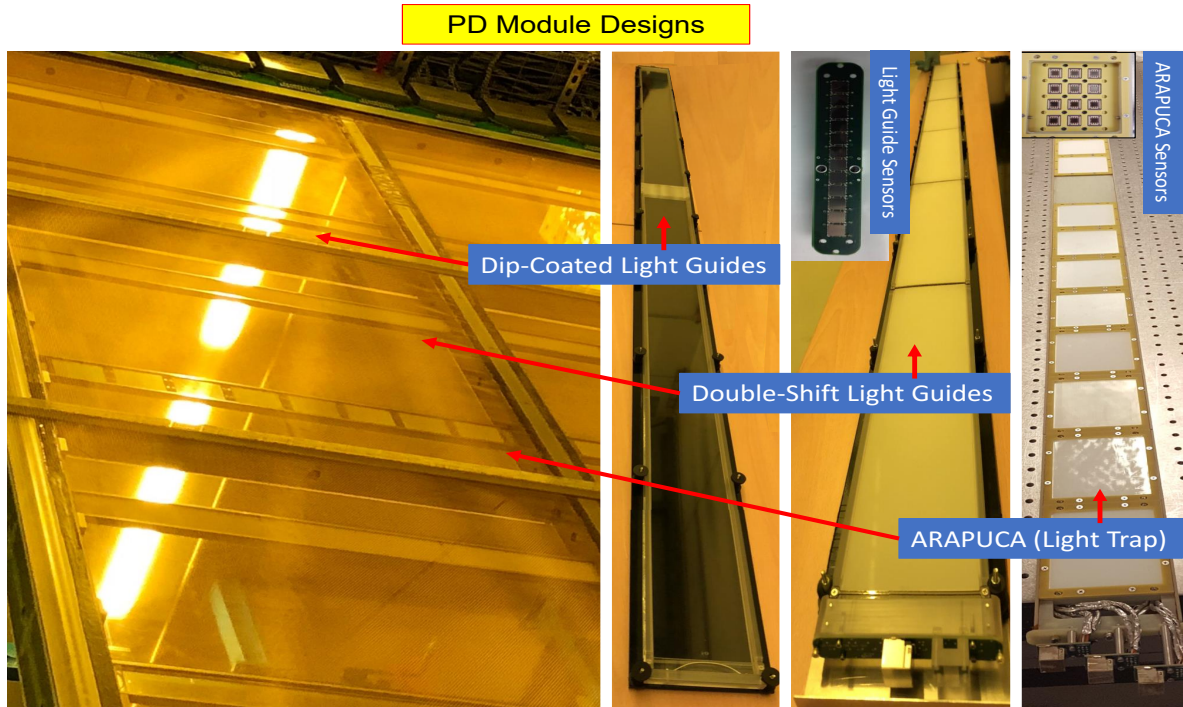


Figure 38: Photon Detectors in a ProtoDUNE-SP APA. The three types of photon collector technologies are shown in the APA (left) and before installation (right), along with the arrangement of photosensors. Before installation and from left to right, the modules are: a dip-coated light-guide module, a double-shift light-guide module, and an ARAPUCA (light trap). The right-most collection of photosensors shows the arrangement of a single cell in the ARAPUCA and the sensor collections just to its left show the arrangement of photosensors in the dip-coated and double-shift modules.

1612

1613 4.3.1 Photon Collector: Dip-coated Wavelength-shifting Light Guides

1614 The dip-coated collector design uses diamond-polished acrylic, cut from cast LUCITE UTRAN
1615 manufactured by Palskolite, Inc., and supplied by EMCO Industrial Plastics as the light-guide
1616 “bar”. The bar has an index of refraction of 1.49 and is dipped in a solution of tetraphenyl-
1617 butadiene (1,1,4,4-Tetraphenyl-1,3-Butadiene, TPB) and other solvents (including a surfactant) to
1618 produce a wavelength-shifting (WLS) layer on the outside surface. When a particle passes through
1619 the active volume, VUV light produced from scintillation at 128 nm interacts with the surface
1620 coating on the bar, where it is shifted to blue light at 425 nm, and isotropically emitted. Once the
1621 blue light enters the light guide, it travels via total internal reflection and is absorbed by a collection
1622 of photosensors at one end. A conceptual example of the dip-coated WLS light guide is shown in
1623 Figure 39.

1624 Bar construction began with the industrial manufacture of the acrylic, which was shipped
1625 pre-polished. The first quality control step was a visual inspection of the acrylic which ensured that

1626 bars used for production were relatively free from scratches or chips and matched pre-production
1627 bars in terms of polish quality. Production bars were then measured at five points of contact using
1628 calipers to verify their required dimensions and tolerances: $(209.270 \pm 0.127 \text{ cm} \pm 8.471$
1629 $0.127 \text{ cm} \pm 0.599 \pm 0.060 \text{ cm})$. Once a bar was approved for use, a unique serial number was
1630 etched on it. The next steps were to anneal (bake and then slowly cool) the bars then dip them in the
1631 WLS solution. Annealing was done to strengthen the bar material and as a form of quality control.
1632 Bar annealing took place in a large oven in Lab 3 at Fermilab that was set at about $76.7 \text{ }^\circ\text{C}$. Baking
1633 lasted approximately four hours. Annealed bars were required to bear no visual signs of crazing
1634 (mechanical stress breaks that make the bar appear cloudy). Accepted bars were cleaned with
1635 ethanol and dipped in a coating solution, consisting of 50 mL toluene, 12 ml ethanol, 0.1 g acrylic
1636 pellets, and 0.1 g TPB for five minutes, where the acrylic pellets ensure that the coating index of
1637 refraction matches that of the bar [23]. A mechanised dipping vessel was prepared to automate the
1638 process and standardise bar quality. Finally, successfully prepared, annealed, and dipped bars were
1639 hung in air under a fume hood to dry for at least 30 minutes. The dipping and drying processes
1640 were sensitive to moisture and required a low-humidity environment ($<15\%$ relative humidity). The
1641 dipping vessel at Fermilab is shown in Figure 40.

1642 Quality control for fully dipped and dried bars consisted of observing the attenuation of 200 nm
1643 light in the bars in both warm and LAr temperature regimes. The warm measurements used full-
1644 size bars whereas measurements at LAr temperatures took place on shorter bars that were cut to fit
1645 within the TallBo facility at the Proton Assembly Building (PAB) at Fermilab. Both measurement
1646 campaigns yielded an attenuation length in excess of 2 m.

1647 **4.3.2 Photon Collector: Double-shift Wavelength-shifting Light Guides**

1648 The double-shift light-guide collector [24, 25] combines the use of WLS TPB-coated radiator
1649 plates with a WLS light-guide bar. In this design, LAr scintillated light at 128 nm undergoes two
1650 wavelength-shifting steps, once to 425 nm blue light in the plate and then to 490 nm green light in
1651 the bar. A conceptual example of the double-shift WLS light guide is shown in Figure 39. The
1652 benefits of this design are in the increased efficiency of photosensor detection for light at 490 nm
1653 and in the production and quality control of the technology. During and after construction, bars are
1654 separable and components can be independently studied and optimised.

1655 The outer WLS material is a set of twelve separate radiator plates that completely cover the light
1656 guide, six on each side, placed end-to-end. The plates are made from 1/16 inch acrylic (purchased in
1657 one order from McMaster Carr) that were laser-cut in pairs at Fort Collins Plastics in Fort Collins,
1658 CO. The plates are coated by hand in a WLS solution consisting of 5 gm of scintillation grade
1659 ($>99\%$) TPB to 1,000 gm of dichloromethane, using a Binks high-volume lower pressure sprayer
1660 system. Two plates, cut from a single piece of acrylic, along with three breakout tabs for quality
1661 control, are coated with the WLS at the same time (tab-plate-tab-plate-tab).

1662 Once the plates are coated, they are annealed in a vacuum oven at $80 \text{ }^\circ\text{C}$, a temperature just below
1663 the melting point of the acrylic. The annealing incorporates the TPB into the acrylic, ensuring that
1664 it will not separate or precipitate due to aging or cryocycling in LAr. Metrology tests are carried
1665 out to ensure that no changes in bar dimension occurred during annealing. The plates are then
1666 separated and the breakout tabs are tested for brightness using a McPherson VUV monochromator
1667 with an H_2 lamp source, and calibrated with a NIST-calibrated photodiode. Each plate is evaluated

1668 with respect to a standard tab, averaging the response from the two tabs on either side of it [26].
 1669 The evaluation is relative; plates are accepted only if they are brighter than baseline plates that meet
 1670 efficiency goals derived from DUNE physics requirements. The measurement of baseline plate
 1671 efficiency was conducted on a LAr test stand at Fermilab, on two prototype paddles using a cosmic
 1672 ray trigger [24].

1673 The second WLS material and primary light guide for the double-shift collectors is made from
 1674 special commercial Eljen EJ-280PSM crosslinked polystyrene. The polystyrene was cut into bars
 1675 that were required to meet the following dimensions within tolerances: (209 15 0 05 cm 8 6
 1676 0 05 cm 0 6 0 05 cm). Bars that passed were next accepted or rejected on the basis of internal
 1677 attenuation length, which was measured in a dark box with a 435 nm LED at room temperature. The
 1678 correlation between attenuation length at room temperature and at LAr temperature was established
 1679 at Indiana University on a set of shorter Eljen bars. The results of these combined studies showed
 1680 that a room temperature attenuation length measurement greater than 6.4 m in the dark box ensured
 1681 an attenuation length in LAr greater than 2 m. An attenuation length greater than 6.80 m as measured
 1682 in the dark box at Indiana University was therefore required for acceptance [26].

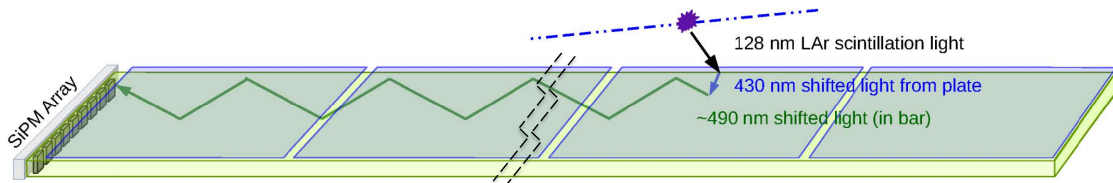


Figure 39: A conceptual example of the dip-coated and double-shift WLS light guides. The top design shows conceptually how the dip-coated light guide collects scintillation light at 128 nm and converts it to 430 nm. The bottom design shows the operation of the double-shift WLS light guide. It converts from 128 nm to 430 nm and then again to 490 nm.

1683 4.3.3 Photon Collector: ARAPUCA Light Trap

1684 ~~The operating concept of the ARAPUCA is the trapping of incident photons inside a highly~~
 1685 ~~reflective chamber until they reach a sensor, yielding high detection efficiency despite a limited~~
 1686 active coverage [27]. A single ARAPUCA cell consists of a highly reflective chamber with a single-
 1687 direction acceptance window. The window consists of a dichroic optical filter sandwiched between
 1688 thin layers of wavelength shifting materials. A conceptual demonstration of the ARAPUCA concept
 1689 is shown in Figure 41 and its construction is shown in Figure 42.

1690 For the collector to act as a photon trap, the external face of the dichroic filter has a WLS
 1691 coating with an emission wavelength less than the cutoff wavelength of the filter. The transmitted
 1692 photons pass through the filter where they encounter a second WLS-coated surface. This second



Figure 40: Mechanized dipping setup at Fermilab, used for the production of dip-coated light guides.

1693 coating has emission spectra that exceed the cutoff wavelength, thus trapping the photon inside the
1694 box. Trapped photons reflect off the inner walls and the filter surface(s) (of reflectivity typically
1695 greater than 98%) and have a very high probability of impinging on a photosensor before being
1696 lost to absorption. Dichroic filters with cutoff at 400 nm were acquired from Omega Optical. The
1697 internal surfaces of the filter are lined with VIKUITI™3M specular reflector coated with TPB,
1698 and P-Terphenyl (1,4-Diphenylbenzene, PTP) is applied to the external side of the filter. PTP and
1699 TPB coatings were applied using a resistive evaporation technique under a clean vacuum of at least
1700 2.0×10^{-6} torr. A quartz microbalance was used to monitor rate and thickness during coating and
1701 was consistently placed in the same position relative to the substrates and target material. PTP and
1702 TPB surface densities are about 200 and 300 cm^2 , respectively.

1703 Quality control for each batch of evaporated coating consisted of the random testing of one of
1704 four pieces in liquid argon. The test pieces were cooled in cold argon vapor for two hours before
1705 being fully immersed in LAr for up to 20 hours. When a piece did not pass this test, the entire

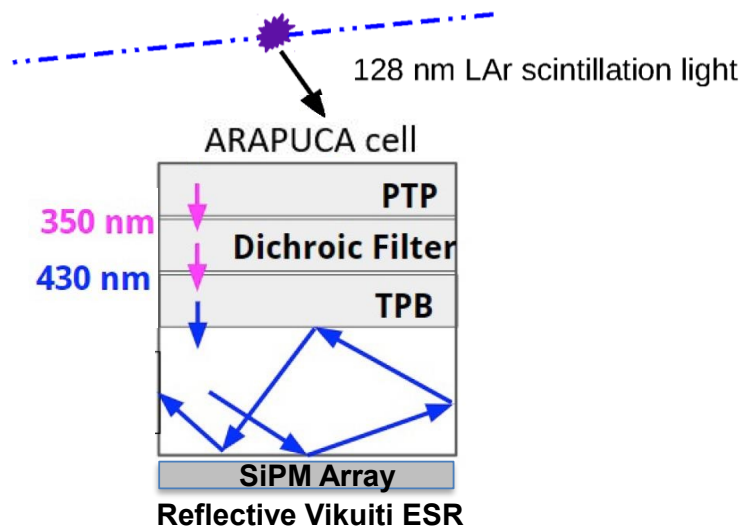


Figure 41: A schematic diagram of the ARAPUCA light trap. Scintillation light is first wavelength shifted to 350 nm to pass through a dichroic filter, then again to 430 nm after the filter, at which point it can no longer return through the acceptance window. It internally reflects until absorbed by the photosensor array.

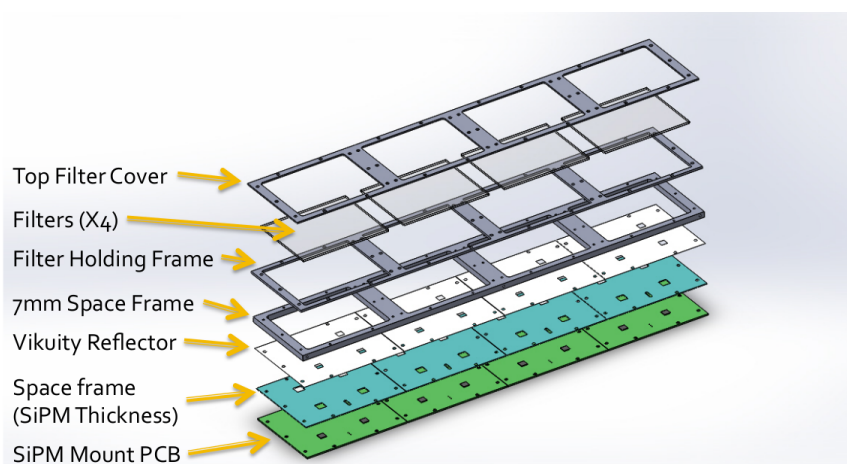


Figure 42: Exploded view of one ARAPUCA supercell. The filter cover, filters, and filter holding frame are all embedded in the space frame. MPPCs photosensors are mounted in the SIPM Mount PCB and supported by the second space frame.

1711 **4.3.4 Photosensors**

1712 The ProtoDUNE-SP PDS uses three different silicon photon sensor (SiPM) models commercially
1713 manufactured by two different companies, SensL Technologies, Ltd. (now, ON Technologies) and
1714 Hamamatsu Photonics. All sensors have the same active area, $6 \times 6 \text{ mm}^2$. Samples of the different
1715 sensors types were tested and characterised at LN_2 temperature before use.

1716 SensL Technologies, Ltd provided (MicroFC-60035-SMT) sensors with pixel size $35 \text{ }\mu\text{m}$. Two
1717 types of series models were used, A-Series and C-Series, with the switch due to a change in
1718 availabilty from the manufacturer. SensL devices equip most of the WLS bar-type modules, i.e., 21
1719 dip-coated modules and 22 double-shift modules. Each module array contains 12 SiPMs passively
1720 ganged in groups of three and read out as four independent channels. A total of 172 channels are
1721 equipped with 516 SensL SiPMs.

1722 Hamamatsu Photonics provided two versions of its Multi-Pixel Photon Counter (MPPC) of
1723 model number S13360-6050, a CQ “Quartz Window” type and a VE “Through Silicon Via” type
1724 for use in the WLS bar detectors and the ARAPUCAs. Both have a pixel of $50 \text{ }\mu\text{m}$. The VE MPPC
1725 is coated with epoxy resin and uses through-hole electrodes called TSV (through-silicon via). In
1726 VE MPPCs, the space around the active area is reduced with respect to standard wire-bonding
1727 techniques, allowing for better packaging. The Quartz Window MPPC is an uncoated MPPC in
1728 a ceramic package with a quartz window, aimed to better resist thermal stresses. All ARAPUCA
1729 modules are equipped with Hamamatsu CQ MPPCs, while eight dip-coated and seven double-shift
1730 modules are equipped with VE MPPCs. All photosensors were tested at warm temperature before
1731 mounting them on the boards, to verify compliance with producer specifications. The equipped
1732 boards were thermal-cycled and tested again before being coupled to the lightguides.

1733 **4.3.5 Photon Detector Readout Electronics**

1734 For each photon detector, signals from one of the three different ganging schemes are summed
1735 together and connected, in the cold volume, to a 20 m long multi-conductor Cat6 cable that feeds
1736 through the detector flange. No front-end electronics are necessary in the cold volume for the
1737 operation of the ProtoDUNE-SP PDS. The readout system transmits unamplified signals from
1738 the photosensors in the LAr volume to the outside of the cryostat and performs processing and
1739 digitisation using a SiPM Signal Processor (SSP), a readout developed and manufactured by Argonne
1740 National Laboratory. Signal cables from each of the six detector flanges connect directly to four
1741 of 24 SSP modules. An SSP module consists of 12 individual readout channels packaged in a
1742 self-contained 1U module. Each channel contains a fully-differential voltage amplifier and a 14 bit,
1743 150 MHz analogue-to-digital converter (ADC) that digitises the waveforms received from the SiPM
1744 arrays. The front-end amplifier is configured as fully-differential with a high common-mode
1745 rejection, and receives the SiPM signals into a termination resistor that matches the characteristic
1746 impedance of the signal cable. The SSP module can operate three separate WLS light guide modules
1747 or one ARAPUCA module.

1748 The digitised data is stored in pipelines in the SSP, for up to 13 ns for a single output, per
1749 channel. The processing is pipelined, and performed by a Xilinx Artix-7 Field-Programmable Gate
1750 Array (FPGA). The FPGA implements an independent Data Processor (DP) for each channel. The
1751 processing incorporates a leading edge discriminator for detecting events and a constant fraction

1752 discriminator (CFD) for sub-clock timing resolution. An operational schematic of the SSP is
 1753 shown in Figure 43. Each channel can be individually triggered by any of the following: a

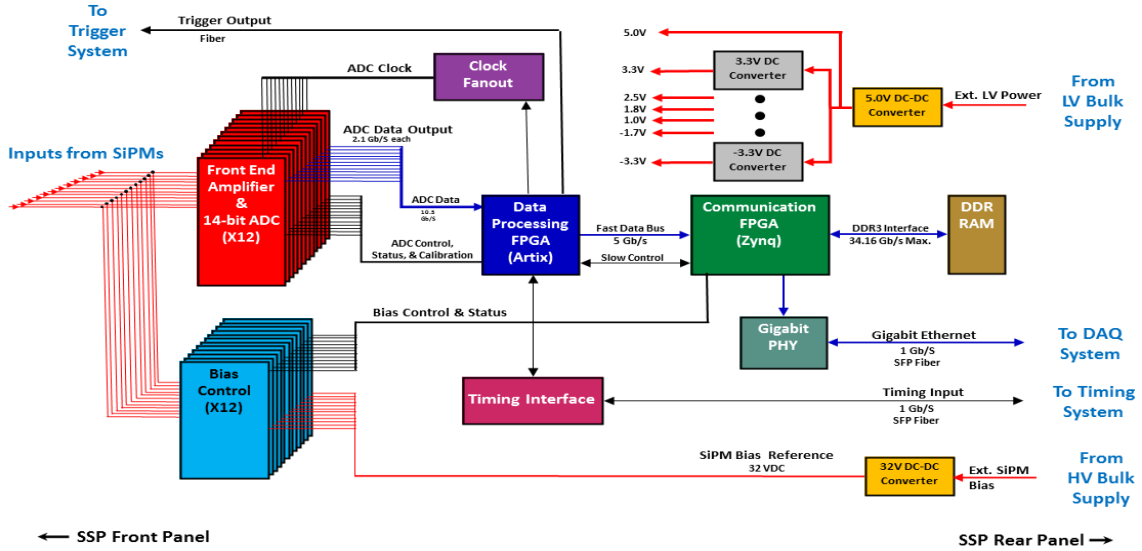


Figure 43: Operational schematic of the ProtoDUNE-SP SSP. This diagram shows how the SSP manages the timing, readout, and bias voltage of 12 channels of ganged photosensors. The SSP also interfaces with the end trigger, DAQ, and timing systems.

1753
 1754 periodic timestamp trigger, a SSP-internal trigger based on a leading-edge discriminator local to
 1755 the individual channel, or a SSP-external trigger from the timing system. If a SSP trigger is present,
 1756 the channel will produce a data packet consisting of a header and a waveform of predefined length,
 1757 which comprises a series of ADC values. The header contains bookkeeping information (e.g.,
 1758 module and channel numbers, timestamps, trigger type) and some calculated integral values for
 1759 the waveform. Because the SSP trigger system is distinct from the global trigger, the unit of data
 1760 produced when an SSP channel triggers is called a “packet,” and the term “trigger” refers to the
 1761 global triggers only. The SSP boardreader generates a fragment when a trigger produced by the
 1762 timing system is observed, and this fragment will contain all packets received from the SSP with
 1763 timestamps in a window ± 2.5 ms from the timestamp of the trigger.

1764 In general, an SSP fragment will contain a fixed 12 packets with identical timestamps cor-
 1765 responding to the trigger time, one for each channel, and also an arbitrary number of additional
 1766 packets generated when a channel’s discriminator fires. It should be expected that a different number
 1767 of packets will be observed for each channel within a given fragment. In the case that only the
 1768 SSP-external trigger is enabled, exactly 12 packets should be present in a single fragment. In such
 1769 a case the packets received by the SSP that do not fall within the window around a timing system
 1770 trigger will be dropped and never included in a fragment. All 24 SSPs are individually synchronised
 1771 to the dedicated ProtoDUNE-SP timing system time-stamp.

1772 4.3.6 PDS Quality Control and Installation at CERN

1773 All PD modules for ProtoDUNE-SP arrived at CERN ready for APA installation. PD modules
1774 were shipped from Colorado State University (CSU), via a special PD-Crate, which contained 12
1775 PD modules, individually packaged in an anti-static bag and placed between anti-static foam. The
1776 final quality control steps before installation were a visual inspection of each PD module and an
1777 assessment of each module using a PD darkbox scanner, shown in Figure 44.

1778 In the standard procedure for the darkbox scanning measurements, both the module photosen-
1779 sors (SiPMs/MPPCs) and the darkbox-LED were allowed to warm up for 30 minutes, using nominal
1780 voltage. This assured stability within each scan and reliability for module-to-module comparisons.
1781 The PDS group used LBNEWare, custom made software which interfaces with the SSPs directly,
1782 as the DAQ for these tests. For each module scan, the LED was set to pulse and read out 5000
1783 times at multiple locations along each side of the PD module. This allowed for sufficient signal
1784 observation and determination of the mean response of the module along each position. The mean
1785 response was determined by fitting a Gaussian to the 5000 integrated waveforms. Prior to arrival at
1786 CERN an attenuation length had been calculated for each PD module using the relative brightness
1787 (mean signal) along each position. At CERN, a cross-check in pseudo-attenuation length was made
1788 and the module with the longest pseudo-attenuation length was selected for installation into the
1789 APA. Modules were placed facing the TPC for the best photon yield response. Spare modules were
1790 also sent to CERN and were sorted for use in the detector through the same module-to-module
1791 comparisons using the same pseudo-attenuation measurement. Figure 44 shows the result of a
1792 sample scan [26].

1793 Each APA frame held ten PDS modules, inserted on rails, equally spaced along the full length
1794 of the APA frame. The spacing between modules along the direction was approximately 60 cm.
1795 PDS modules were inserted into the frames of completed APAs, between the sets of wire layers. Two
1796 ARAPUCA devices were mounted in ProtoDUNE-SP, one in APA 3 directly in front of the beam
1797 plug for the observation of photons from beam interactions, and the other in the middle of APA 6 to
1798 observe photons from cosmic particles. The two light-guide designs filled the remaining modules
1799 in alternating positions in the APAs. Once the PD modules were installed into an APA, the entire
1800 APA and its components were tested in the cold box. The full PDS chain, including photosensors,
1801 cold cables, warm cables, SSP, DAQ, and the connection to the slow control system was then tested.
1802 The full test included tests for functionality, stability, trigger rates, threshold calibrations, and PD
1803 module response and comparison, as well as thermal-cycling at 150K. With respect to the slow
1804 control and DAQ, nominal configuration settings were implemented in GUI format, with additional
1805 configurations that could be uploaded at run time.

1806 Data rates were also tested using the DUNE Light Calibration Modules (LCMs) and the
1807 Detector Control System data limits were established and optimised for data taking. The cold box
1808 helped determine if live data were sufficient by using the data to prepare for online monitoring
1809 diagnostics, such as persistent traces, leading-edge amplitude histograms, integral waveforms,
1810 average waveforms, and internal/external triggering for every PDS channel. The functionality
1811 of each PDS channel was verified by inspecting waveforms using persistent traces in the online
1812 monitoring system, as shown in Figure 45. The cold box tests and online monitoring allowed the
1813 observation of overall clean waveforms in the data. They also provided an opportunity to observe

1814 faults with the grounding or disconnects in the SSPs, channels, and cables. The cold box tests also
1815 allowed preliminary module-to-module comparisons.

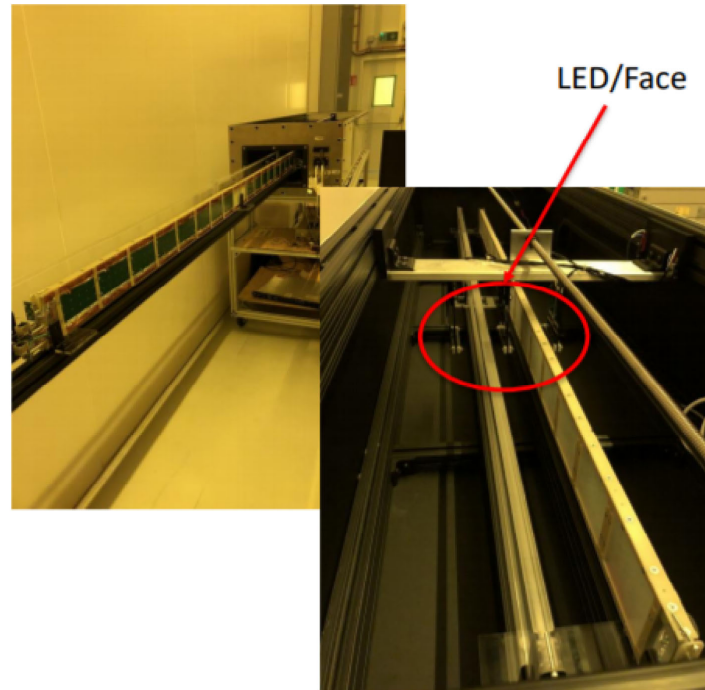


Figure 44: PDS Darkbox Scanner and Sample. A photon detector was light sealed in the box and exposed to incident light along its entire length provided by an LED.

1816 The cryogenic PD cables were installed at the same time as the PD modules. Each APA has
1817 ten Cat6 PD cables, one per module, with alternating installation sides. During installation of the
1818 APAs in the cryostat, cables were routed through feedthroughs in the cryostat roof. From there,
1819 the cables were connected to the SSP modules (see Figure 46). During the cold box tests and after
1820 installation, the PDS was fully interfaced with both the Detector Control System (DCS) and the
1821 monitoring system. Photosensors can be biased and unbiased from the DCS, their status can be
1822 displayed, and the bias voltage can be modified manually or according to different preset conditions,
1823 as shown in Figure 47.

1824 **4.3.7 Photon Detector UV-Light Calibration System**

1825 A UV-light-based calibration and monitoring system, designed and fabricated by Argonne National
1826 Laboratory, is used to calibrate SiPM gain and cross-talk, and to monitor linearity, time resolution,
1827 and long-term stability of the system. The system hardware consists of both warm and cold
1828 components. The system has no active components within the cryostat and in no way alters the
1829 operation of the PDS or the HV system. The active system component consists of an external 1U
1830 rack-mount Light Calibration Module (LCM). The LCM generates 275 nm UV-LED light pulses
1831 that propagate through a quartz fiber-optic cable to diffusers located at the CPA. The calibration
1832 module consists of an FPGA-based control logic unit coupled to an internal LED Pulser Module

Cold Tests

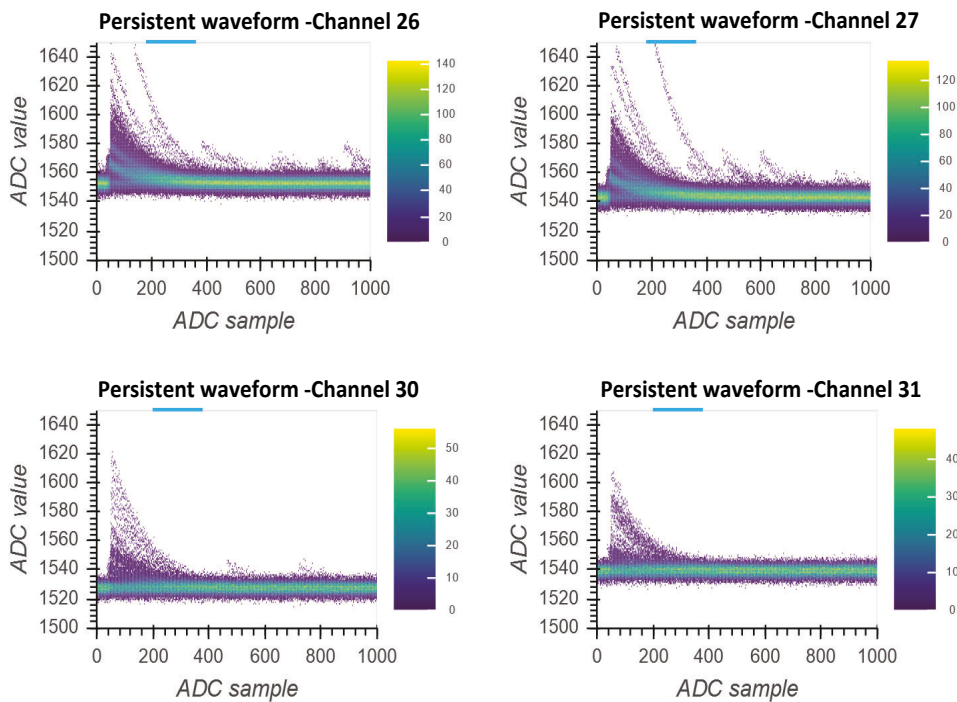


Figure 45: Photon detector cold box waveform example. Each plot shows the raw response of the photon detector channel under quality control testing in the CERN cold box before installation into

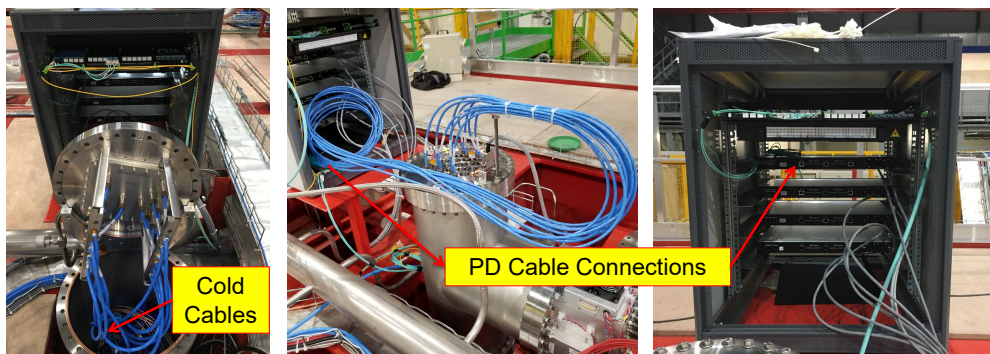
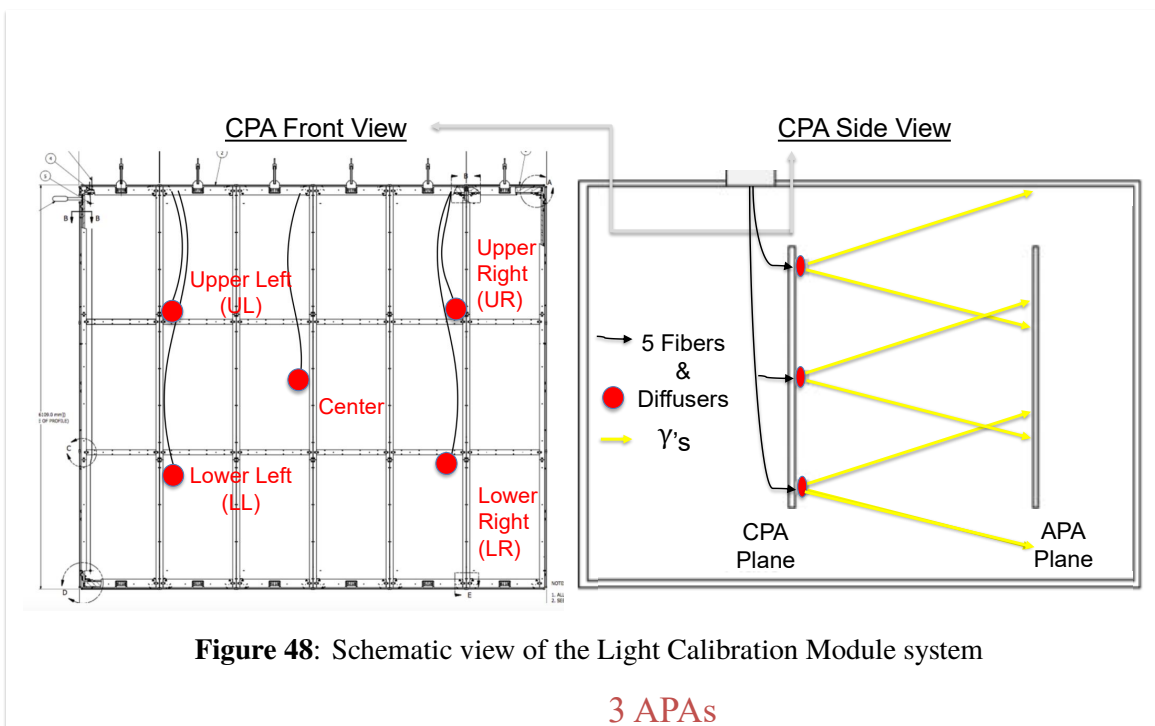
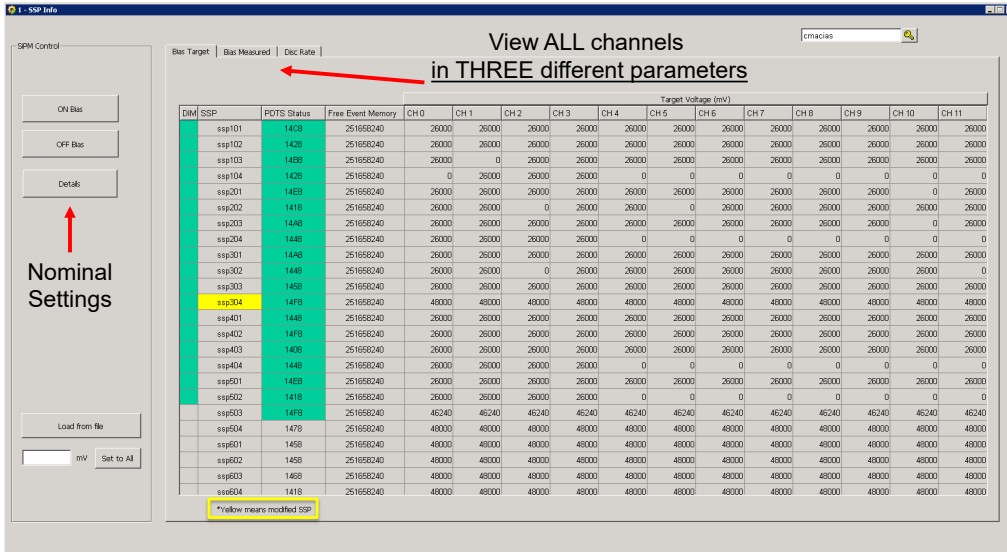


Figure 46: PDS Cable Routing. From left to right, the three pictures show cold cables connecting to the flange from inside the cryostat, warm cables connecting from the warm side of the flange, and warm cables connecting from the flange warm side to the SSPs.

1833 (LPM) and an additional bulk power supply. Light diffusers located on the CPA surface uniformly
1834 illuminate the APA surface and hence the PDS light collection modules. Five light diffusers on
1835 each face of the CPA plane are used: one in the center and four in each of the four CPA corners, as
1836 shown in Figure 48.

1837 The calibration system produces UV light flashes with a predefined pulse amplitude, pulse
1838 width, repetition rate, and pulse duration. It also provided an external trigger for the light collection



1839 system. Pulse multiplicity control offers the option to produce two pulses at a fixed time difference
 1840 to study timing properties of the photon system as well as trigger delays. The UV light system was
 1841 used as a complement to cosmic-ray muons for calibration.



1842 **4.3.8 Full PDS Performance**

1843 The performance of the full PDS as measured during ProtoDUNE-SP operations is reported in
 1844 detail in the ProtoDUNE-SP performance paper [3]. A summary is included here for completeness.
 1845 All channels exhibit a linearity of gain response to varying bias voltage (V_B). The actual breakdown
 1846 voltage (V_{bd}) of the multi-sensor channel at LAr temperature, however, shows a relatively large

1847 spread, particularly for the 12-H-MPPC channels of the ARAPUCA modules. For these 12-H-MPPC
1848 channels, the signal-to-noise (SNR) values are around 6, while for the 3-S-SiPM channels of the
1849 double-shift and dip-coated bar modules the SNR is in the range 10 to 12. Within the uncertainties
1850 of the calibration measurements taken during operations, neither the gain nor the other parameters
1851 were found to drift significantly over time for any of the sensors used in the ProtoDUNE-SP PDS.
1852 The photon detection efficiency was evaluated through eight independent measurements using muon
1853 and electron data at four different beam momenta, supplemented by simulation. Photon detection
1854 efficiencies average 2% for the single area ARAPUCA cell, 0.21% for the double-shift module, and
1855 0.08% for the dip-coated modules (see Table 4 in [3]). An extrapolation of the performance to a
1856 PDS system consisting entirely of ARAPUCA modules indicates that it can perform calorimetric
1857 energy reconstruction with an expected light yield of 1.9 photons/MeV at 3.3 m from the anode.
1858 This performance exceeds the specifications of the DUNE far detector by almost a factor of four.

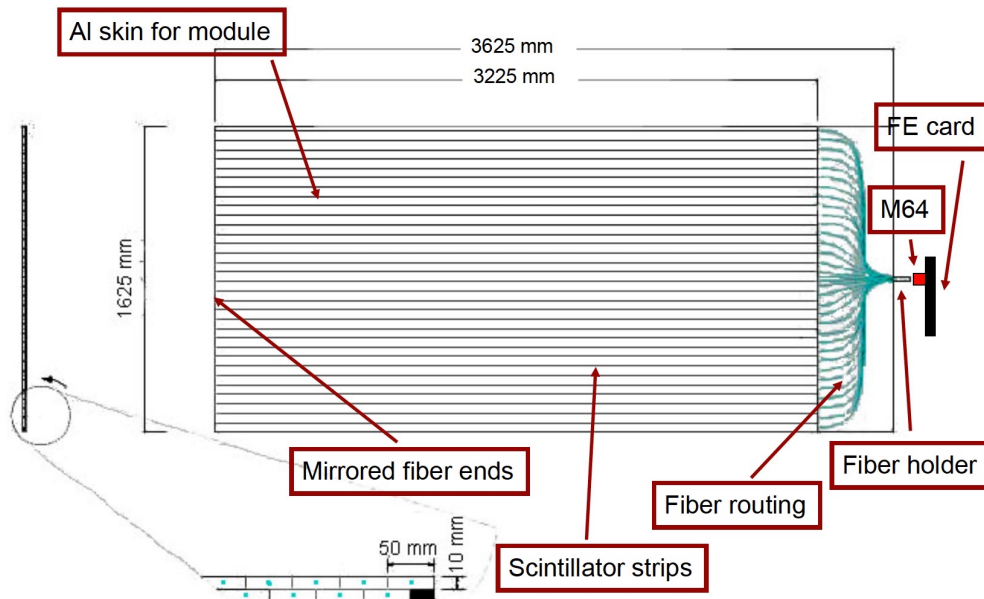


Figure 49: Labeled illustration of a CRT module.

4.4 Cosmic Ray Tagger (CRT)

As ProtoDUNE-SP sits on the surface, it experiences 20 kHz of cosmic-ray muons entering the detector. To provide external reconstruction to a sample of these cosmic-ray muons and beam halo-muons, a system of scintillation counters external to the cryostat, called the CRT, covers almost the entire upstream and downstream faces of the TPC. The fact that the CRT only covers the front and back faces of the TPC means that many cosmic-ray muons do not cross any part of the CRT. Both tagged and untagged muons provide important calibration data and performance indicators.

The scintillation counters used in the CRT were originally built and deployed for the outer veto of the Double Chooz experiment [29]. The CRT is composed of 32 modules, each of active area 1.6 m \times 3.2 m, arranged into mechanically independent super-modules of four modules each.

Each module is instrumented with 64 scintillator strips 5 cm wide and 365 cm long, arranged in two parallel planes of 32 each. A schematic of a CRT module is shown in Figure 49.

Each strip has a wavelength-shifting scintillating fiber that transports the light to an individual pixel of a 64 multi-anode photo-multiplier tube (Hamamatsu M64). The two layers of strips are offset by half a strip width to maximise coverage. The extra centimeters of strip, compared to the length of a module (320 cm), are outside the active area. Each module measures a one-dimensional spatial position from its strip number and measures its given position along from its super-module's placement. To reconstruct a CRT hit in three-dimensions, two modules are placed edge-to-edge with their strips all parallel, and two more placed behind them in with their strips rotated by 90 degrees. This composes one super-module of dimensions 3.65 m by 3.65 m, as illustrated in Figure 50. The coordinate system is shown in Figure 51.

For the ProtoDUNE-SP downstream face, four super-modules are arranged edge-to-edge in a square roughly the size of a ProtoDUNE-SP face, also shown in Figure 50. This assembly of CRT modules is centred with respect to the centre of the TPC in and placed 10.5 m from the upstream

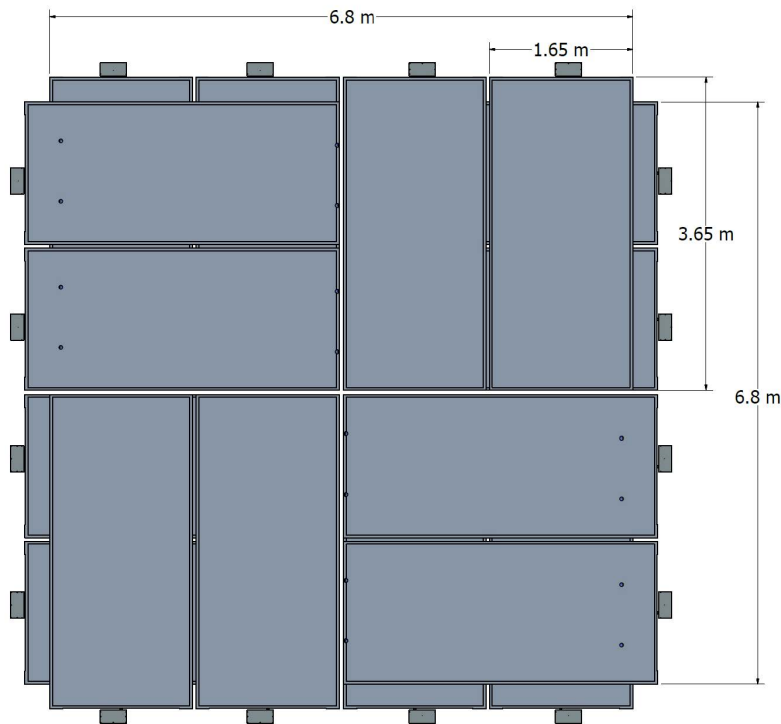


Figure 50: Drawing of the downstream CRT module assembly, showing the four super-modules positioned in a square. Each super-module consists of two modules edge-to-edge with scintillator strips running in the x direction, and either behind or in front of them, two modules with strips running in the y direction. The active area of the entire assembly is $(6.8 \text{ m})^2$, as indicated. For the upstream portion, the assembly is split in two, left and right.

1883 face of the TPC in the cryostat.

1884 The positioning of the upstream super-modules of the CRT system is complicated by the
 1885 presence of the beampipe requiring that this portion of the CRT system be split, with the right
 1886 and left halves offset from each other in x . One set of the two vertically stacked super-modules
 1887 is placed 2.5 m from the front face of TPC (left of beam) and the other (right of beam) is placed
 1888 9.5 m upstream of it, as shown in Figure 51 and in the photographs in Figure 52. In each stack,
 1889 the upper and lower super-modules are actually offset slightly from each other in y (the upstream to
 1890 downstream direction) so that they can both hang from the same bar.

1891 Scintillation light from the strips is measured by the M64 photomultipliers. Customised ADC
 1892 boards then digitise the signals of all strips in the module. A CRT module will trigger if any
 1893 ADC signal is above threshold and provide the Central Trigger Board or CTB (see Section 6.1)
 1894 the digitised readings of all 64 strips in a single CRT module with a timestamp that has a 20 ns
 1895 resolution.

1896 Offline reconstruction then assembles the CRT signals stored for an event into three-dimensional
 1897 hits. First, strip signals below the dark count threshold are rejected and then the pulse magnitude,
 1898 CRT module number, the strip's identification number, and a timestamp for each strip is collected
 1899 from the raw data. These primitively act as “one-dimensional” hits and are then sorted between

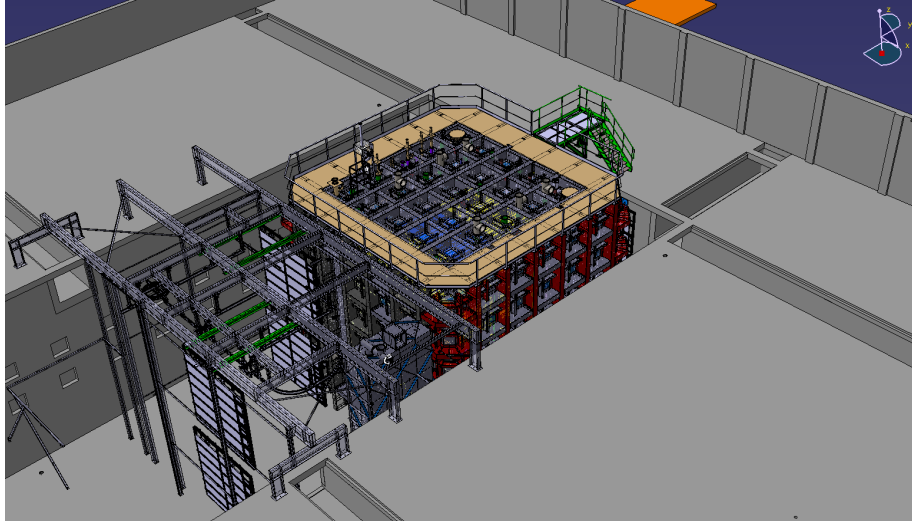


Figure 51: 3D CAD view showing the upstream CRT planes split left and right to accommodate the beam pipe.

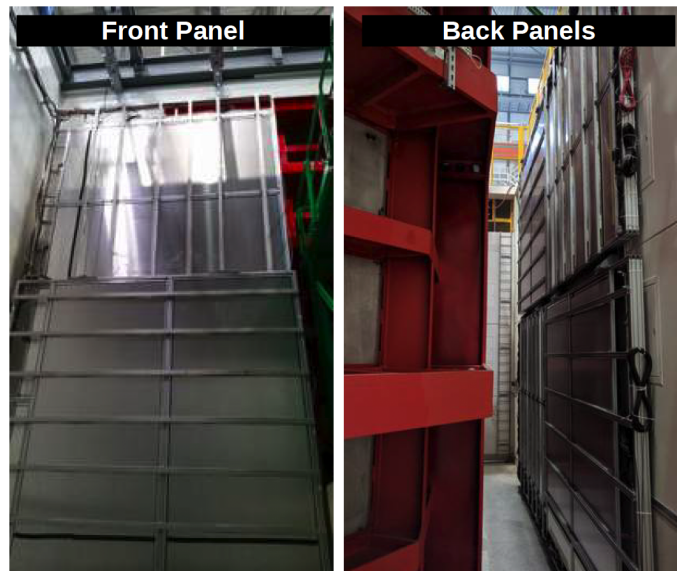


Figure 52: Photos of the beam-left upstream CRT assembly of two super-modules (left) and the downstream assembly of four super-modules.

1900 upstream and downstream CRT modules based on their CRT module channel number. Reconstructed
 1901 CRT hits are then constructed by combining strip signals of overlapping CRT modules that occur
 1902 within a coincidence window. The coincidence window is set at 80 ns or 4 time ticks of the CTB and
 1903 was decided upon using information on the timing offsets between CRT modules obtained during
 1904 commissioning. The timing resolution of a CRT hit is measured as the difference between the
 1905 timestamps on two overlapping CRT modules, measured to be less than 60 ns as seen in Figure 53.

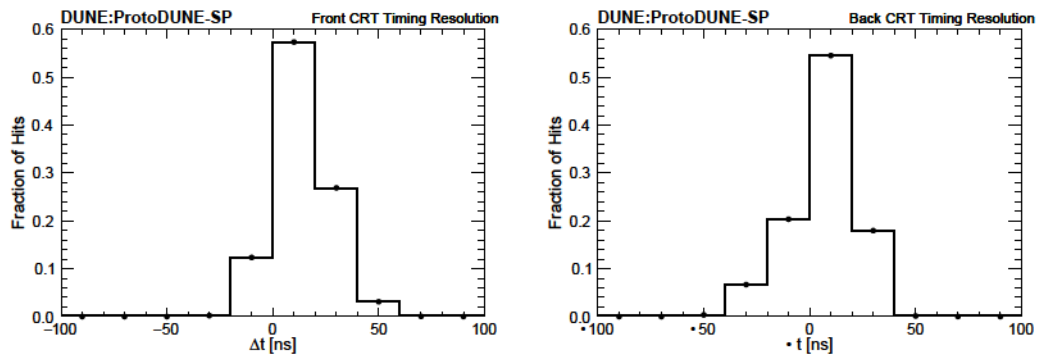


Figure 53: Timing resolution for CRT reconstructed hits on the front CRT modules (left) and on the back CRT modules (right) from data taken in November 2018.

1906 4.5 Cryogenics Instrumentation

1907 ProtoDUNE-SP includes instrumentation designed to monitor the quality and stability of the overall
1908 detector environment, to ensure that the LAr quality is adequate for operation of the detector, and
1909 to help diagnose the source of any changes in detector operations (see Figure 54). Monitoring
1910 instrumentation placed inside the cryostat includes thermometry to monitor the cryostat cool-down
1911 and fill, level meters to monitor the height of the LAr surface, purity monitors to provide a rapid
1912 assessment of the electron-drift lifetime independent of the TPC, and a system of internal cameras.
1913 Gas analysers used to monitor the cryostat purge process are located outside the cryostat.

1914 4.5.1 Purity Monitor

1915 Achieving an electron lifetime that is long enough so that electrons can drift sufficient distances is
1916 a challenging aspect of LArTPCs. The electron (e^-) lifetime in a LArTPC is inversely proportional
1917 to, and determined by, the electronegative impurity concentration in the LAr, making the LAr
1918 purity an essential concern for successful operation and physics reach of the detector. Electron
1919 loss due to electronegative impurities in a LArTPC can be parameterised as $N_0 e^{-t/\tau}$,
1920 where N_0 is the number of electrons generated by ionization and not recombined with argon ions,
1921 τ is the number of electrons after drift time t , and τ is the electron lifetime. ProtoDUNE-SP
1922 was designed to have the same 3.6 m drift distance and 500 V/cm electric field as planned for
1923 the DUNE-SP far detector modules. Given the drift velocity of approximately 1.5 mm/μs in this
1924 field, the drift time from cathode to anode is roughly 2.3 ms. Thus, if the electron lifetime is
1925 2.3 ms $\ln 0.8 \approx 0.22$ 10 ms, then the LArTPC signal attenuation, $N_0 e^{-t/\tau} / N_0$, remains
1926 less than 20% over the entire drift distance.

1927 Purity monitors are used to independently infer the effective free electron lifetime in a LArTPC.
1928 It works by illuminating a photocathode with deep UV light to generate an electron current, then
1929 collects the drifted current at an anode a known distance away. Attenuation of the current is related
1930 to the electron lifetime. In the ProtoDUNE-SP purity monitors the UV light is generated by an
1931 external xenon light source and delivered by quartz fibres to the inside of the cryostat. The fraction
1932 of photoelectrons generated at the purity monitor cathode that arrives at the anode (N/N_0) after
1933 the drift time t is a measure of the electron lifetime τ : $N/N_0 = e^{-t/\tau}$, where N_0 is the combined
1934 charge of the electrons generated at the photocathode, N is the combined charge of the electrons
1935 collected by the anode after drift time t , and τ is the electron lifetime.

1936 The purity monitors are placed inside the cryostat but outside of the TPC volume due to their
1937 size.

1938 Although ProtoDUNE-SP receives ample cosmic ray data to perform electron lifetime measure-
1939 ments, the purity monitor system was found to be essential for providing quick, reliable, real-time
1940 information. It enabled operators to catch purity-related changes caused by LAr recirculation issues
1941 in time to correct them.

1942 In addition, since the purity monitors have much smaller volumes than the LArTPC, the
1943 measurements from this system are affected to a much smaller degree by the space charge caused
1944 by cosmic rays. Since purity monitors provide run-by-run electron lifetime measurement in liquid
1945 argon, they have unique importance for DUNE's deep-underground far detector charge calibration,
1946 where the cosmic-ray-based calibration is very challenging due to the low cosmic statistics.

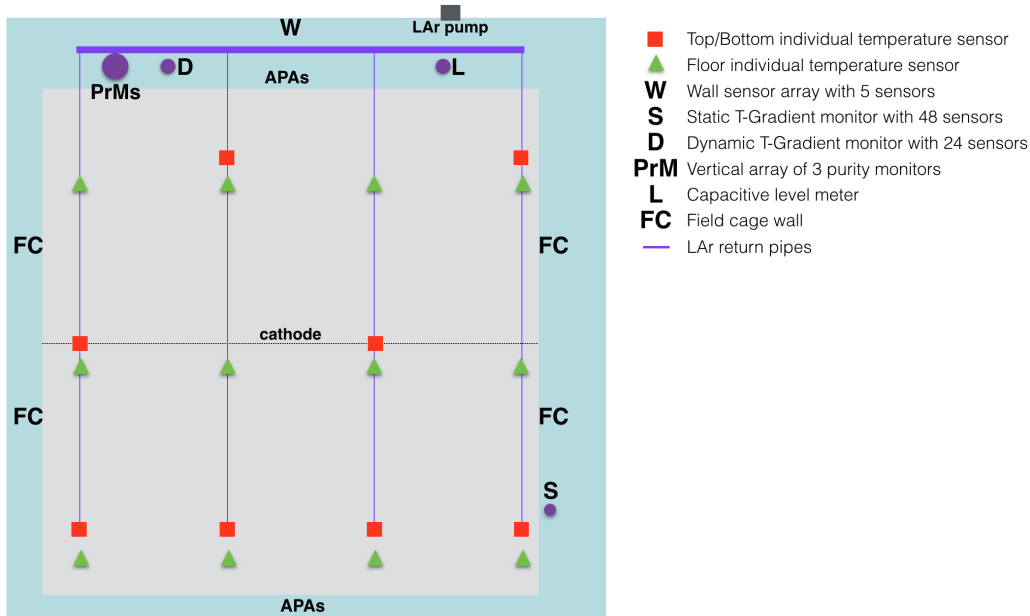


Figure 54: Top view of the cryostat with the distribution of LAr instrumentation devices. The upstream side of the detector where the beam enters the cryostat is on the left hand side of the image.

Purity Monitor Design

1947

1948 The purity monitor design follows that of the monitors used in the ICARUS experiment [16]
 1949 (Figure 55). It consists of a double-grid ion chamber with four parallel, circular electrodes: a disk
 1950 holding a photocathode, two grid rings (one each in front of the anode and the cathode), and an
 1951 anode disk. The cathode grid (labelled “ground-grid” in the figure) is held at ground potential. The
 1952 cathode, anode grid, and anode can each be independently biased via modified vacuum-grade HV
 1953 feedthroughs. The anode grid and the field-shaping rings are connected to the cathode grid by an
 1954 internal chain of 50 MΩ resistors to ensure the uniformity of the electric field in the drift regions.
 1955 A stainless steel mesh cylinder is used as a Faraday cage to isolate the purity monitor from external
 1956 electrostatic background.

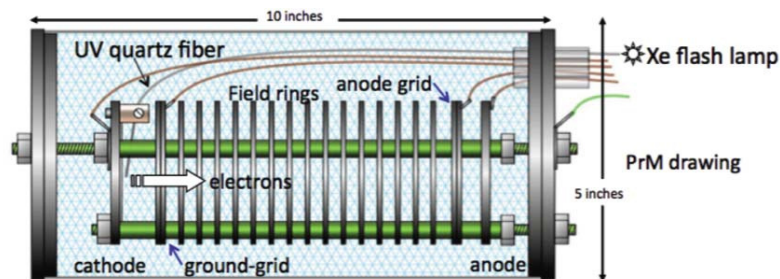


Figure 55: Schematic diagram of the purity monitor design [16].

1957

Low signal strength has limited the precision and measuring ranges of purity monitors in

1958 previous LArTPC experiments [12, 16]. To boost the signal strength for use in ProtoDUNE-SP, UV
1959 light was delivered to each purity monitor by eight fibres and an 8-channel feedthrough, resulting
1960 in signal magnitudes six times larger than with a single fibre. This increase came without penalty
1961 in timing resolution.

1962 The electron drift time is a key indicator of the measurement range and precision of the purity
1963 monitor. The electron drift time depends on the cathode–anode distance and the applied voltage
1964 within the monitor. During the commissioning and beam phases of ProtoDUNE-SP the electron
1965 drift time within the detector varied from 150 μ s to 3 ms. The purity monitors were operated at
1966 different high voltage settings that covered an electron drift time measurement range of 35 μ s to
1967 more than 10 ms. The electron drift lifetime exceeded 3 ms during the beam phase.

1968 **Purity Monitor Data**

1969 Three purity monitors were installed at heights of 1.8 m, 3.7 m, and 5.6 m from the bottom of the
1970 ProtoDUNE-SP cryostat to continuously monitor the LAr purity during all phases: commissioning,
1971 beam test, and operation. Figures 56 and 57 show the anode-to-cathode signal ratios and
1972 the electron lifetime measured by each purity monitor from the commissioning phase, which started
1973 in September 2018, through the entire beam test, which ended in November 2018, and continued
1974 through the non-beam operations, which ended in February 2020. The shaded bands represent
1975 uncertainties in the measurements. All are normalised to a drift time of 2.3 ms.

1976 Each electron-lifetime measurement by the purity monitors is based on the signal ratios
1977 from 200 UV flashes at the same location occurring within a 40 second window. These measure-
1978 ments, taken regularly, were able to indicate incipient circulation-related issues on a quick timescale,
1979 mitigating potentially serious consequences for the detector. They caught a filter saturation during
1980 LAr filling and recirculation pump outages; these incidents show as sudden dips in Figures 56
1981 and 57. The measurement uncertainties in Figure 56 include statistical and time-dependent fluctu-
1982 ations as well as uncertainties in the baseline of the purity monitor signal waveform, the cathode
1983 and anode RC constants, the inefficiency of grid shielding, and the electrical transparency of the
1984 grids. The “inefficiency of grid shielding” refers to the inefficiency of the cathode and anode grids
1985 to shield against induced currents on the anode and cathode while electrons are drifting between the
1986 anode and cathode grids. The electrical transparency of a grid is the proportion of the electrons that
1987 pass the grid. Other uncertainties in such quantities as signal rise time and electron drift time were
1988 found to be small. The overall uncertainties in purity-monitor charge ratio measurement ————
1989 at 2.3 ms drift time for the purity monitors, from highest position to lowest, are 1.9%, 2.2%, and
1990 3.9%, respectively.

1991 Note that given $\tau = \frac{d}{v}$, when $v \rightarrow 0$, the measured lifetime τ is infinity. As
1992 shown in 57, when the LAr purity is stabilised after filtering, τ is close to one, which means
1993 that the electron loss (due to impurities) after drifting for 2.3 ms is very small. The top and middle
1994 purity monitors measured the electron lifetime to be greater than 70 ms, and the bottom monitor
1995 measured it as greater than 30 ms. Considering the inverse relationship between the drift electron
1996 lifetime and the amount of oxygen equivalent impurity, the estimate predicts the impurity never went
1997 above 40 ppt equivalent of oxygen in the week of data-taking. At the end of beam data-taking on
1998 November 11th, 2018, the impurity in the detector can be estimated to be approximately 3.4–0.7 ppt
1999 oxygen equivalent [3, 30]. These measurements indicate that ProtoDUNE-SP exceeded the high

LAr purity required by the DUNE far detector. They also corroborate the high electron lifetime measurements ProtoDUNE-SP has previously reported using TPC tracks matched to the CRT [3], [31].

Again given σ_{τ} , the relative uncertainty in lifetime τ is propagated as $\frac{\sigma_{\tau}}{\tau}$. It follows then that for a given σ_{τ} uncertainty of τ , the relative uncertainty in the measured electron lifetime is proportional to the electron lifetime and inversely proportional to the electron drift time t_d . For a long electron lifetime, the relative uncertainty in this lifetime is large, as shown in Figure 57. However, since the main sources of uncertainties in t_d are not correlated with the lifetime, $\frac{\sigma_{\tau}}{\tau}$ is not significantly correlated with the electron lifetime or the drift time, and therefore the large relative lifetime uncertainty at high purity does not indicate lower precision in the purity monitor's measurement of the charge loss during the electron drift time. The run-by-run purity monitor electron lifetime has been included in the ProtoDUNE-SP calibration database for TPC charge and energy calibration. The performance of the purity monitor based electron lifetime calibration tested with ProtoDUNE-SP cosmic rays is shown in Figure 58 [32]. After the purity-monitor-based lifetime calibration, the charge loss on the TPC signal due to LAr impurity is mostly corrected.

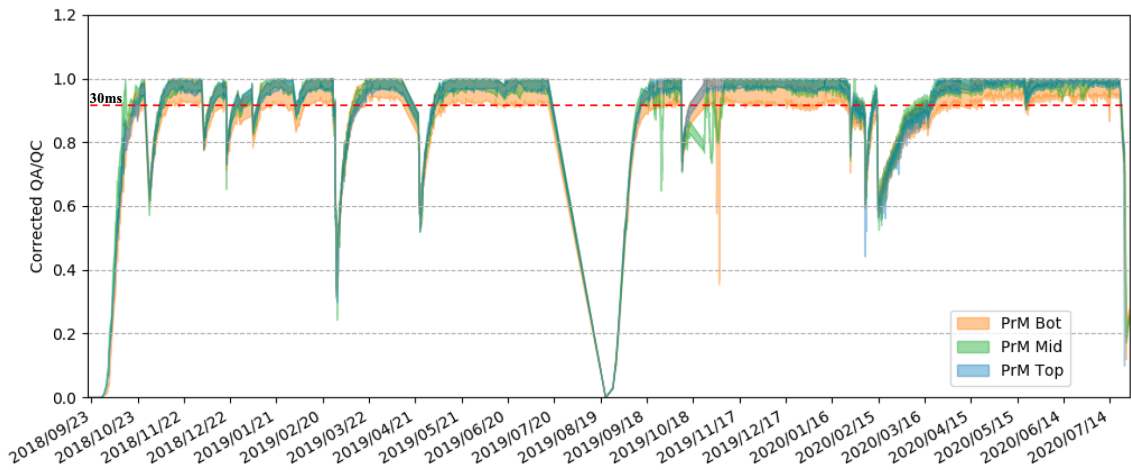


Figure 56: The anode-to-cathode signal ratios measured by three purity monitors in ProtoDUNE-SP as a function of time, September 2018 through February 2020. The purity is low prior to the start of circulation in October 2018. Later dips represent recirculation studies and recirculation pump stops. The shaded bands represent uncertainties of the measurements.

4.5.2 Temperature Sensors

Since the purity monitors cannot be placed within the TPC volume, to monitor the cryogenics system and the LAr for homogeneous mixing, temperature monitors are used as a substitute. An extensive set of temperature measurements is recorded to create a detailed 3D temperature map of the detector volume that is used as input for the computational fluid dynamic (CFD) model validation. Results from these CFD simulations can predict the LAr purity across the entire cryostat volume. The vertical coordinate is particularly important since it corresponds closely to the LAr recirculation and uniformity.

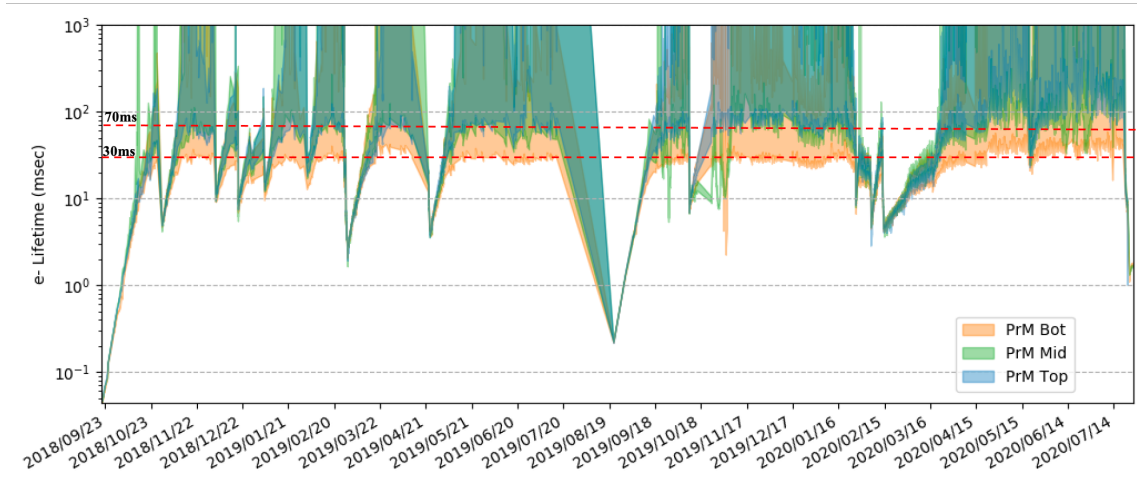


Figure 57: The electron lifetimes measured by three purity monitors in ProtoDUNE-SP as a function of time, September 2018 through February 2020. The purity is low prior to the start of circulation in October 2018. Later dips represent recirculation studies and recirculation pump stoppages. The shaded bands represent uncertainties of the measurements.

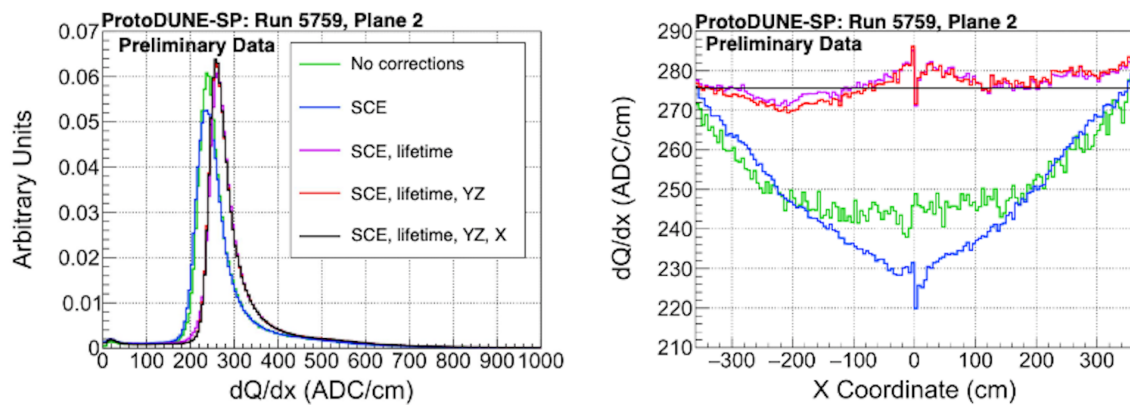


Figure 58: Performance of the purity monitor based electron lifetime calibration for cathode-crossing cosmic rays in ProtoDUNE-SP Phase-1: (Left) distribution and (Right) vs. electron drift distance , comparing no calibration (green), space charge effect calibration (SCE) (blue), PrM electron lifetime calibration+SCE (violet), electron lifetime calibration+SCE+YZ correction, electron lifetime calibration+SCE+YZ+Y correction. After the purity monitor based lifetime calibration (violet), the 15% charge loss on TPC signal (blue) is mostly corrected.

2024 In ProtoDUNE-SP 92 high-precision temperature sensors are distributed near the TPC walls
 2025 in two configurations (see Figure 59): i) a formation of two high-density vertical arrays (called
 2026 T-gradient monitors), and ii) coarser 2D horizontal arrays at the top and bottom of the TPC. The
 2027 bottom sensors are mounted on the LAr return pipes and the top sensors on the ground planes.

2028 Three elements are common to all systems: sensors, cables and readout. Lake Shore PT102
 2029 platinum sensors with 100 resistance (at 0°C) were chosen based on previous experience from

2030 the 35 t prototype[33]. For the inner readout cables, a custom cable made by Axon' was used.
2031 This 3.7 mm diameter cable consists of four AWG 28 teflon-jacketed copper wires, forming two
2032 twisted pairs, with a metallic external shield and an outer teflon jacket . The four-wire configuration
2033 eliminates any influence of wire resistance on the measurements.

2034 Finally, the readout system consists of an electronic circuit that includes: i) a precise 1 mA
2035 current source for the excitation of the sensors, ii) a multiplexer reading out the different temperature
2036 sensors and forwarding the selected one to a single channel, and iii) a readout system based on
2037 the National Instrument Compact RIO Device with a high-accuracy voltage signal readout NI9238
2038 module that provides 24-bit resolution over a 1 V range. In addition, 12 standard temperature
2039 sensors are in contact with the bottom of the cryostat to detect the presence of LAr when filling
2040 starts, and five standard sensors are lined up vertically and epoxied onto one of the lateral walls to
2041 measure the temperature of the cryostat membrane at different heights during cool-down and filling.

2042 **Static T-gradient monitor**

2043 In addition to the distributed temperature sensors described above, a vertical array of 48 sensors was
2044 installed 20 cm away from the lateral field cage (see Figure 59-left). Vertical spacing is 11.8 cm for
2045 both the top and bottom 16 sensors and 23.6 cm for the 16 in the middle, with the bottom (top-most)
2046 sensor 30.2 (738.5) cm from the bottom surface of the cryostat. Mechanical rigidity is provided by
2047 an 80 25 3 mm³ U-shaped fibre glass profile (FGP) that holds sensors and cables. Given the
2048 proximity to the field cage, the entire system is surrounded by a Faraday cage made up of 19 vertical
2049 6-mm-diameter stainless steel rods that are arranged to form a cylinder 12.5 cm in diameter. The
2050 rods and FGP are hung from the top of the cryostat and are mechanically decoupled from each other
2051 to allow for their different contraction rates in the LAr. The rods are passed through FR4 rings
2052 attached to the FGP to maintain the cylindrical shape.

2053 Sensors are mounted on a 52 14 mm² PCB with an IDC-4 connector, such that they can be
2054 plugged in at any time. Cables are housed in the inner part of the FGP and run vertically from the
2055 sensor to the flange, which has eight Sub-D 25-pin connectors.

2056 The temperature sensors are cross-calibrated in a controlled laboratory environment. During
2057 the calibration procedure, a set of four sensors (one of which is kept as a reference for all sets)
2058 are placed next to each other and submerged in LAr several times. The calibration procedure
2059 relies on the assumption of equal temperature for all sensors. Convection is minimised by placing
2060 the four sensors inside a 50 mm diameter, 1 mm thick cylindrical aluminum capsule (allowing
2061 fast cool-down in gas before immersion), which is placed in the centre of a 3D printed box with
2062 two independent concentric LAr volumes, and surrounded by 10 cm thick polystyrene walls. The
2063 stability of the calibration system, and the performance of the sensors and the readout system are
2064 shown in Figure 59-right. The accuracy of the calibration was estimated to be 2.6 mK [34]. This
2065 takes into account the uncertainty on the offset between any two sensors in the static T-Gradient
2066 monitor as well as differences between the four immersions in LAr.

2067 **Dynamic T-gradient monitor**

2068 Finally, a movable system of temperature sensors, called the Dynamic T-gradient monitor, was also
2069 installed in ProtoDUNE-SP. The Dynamic T-gradient monitor is equipped with a stepper motor
2070 connected to a carrier rod on which 24 temperature sensors are mounted. The carrier rod with

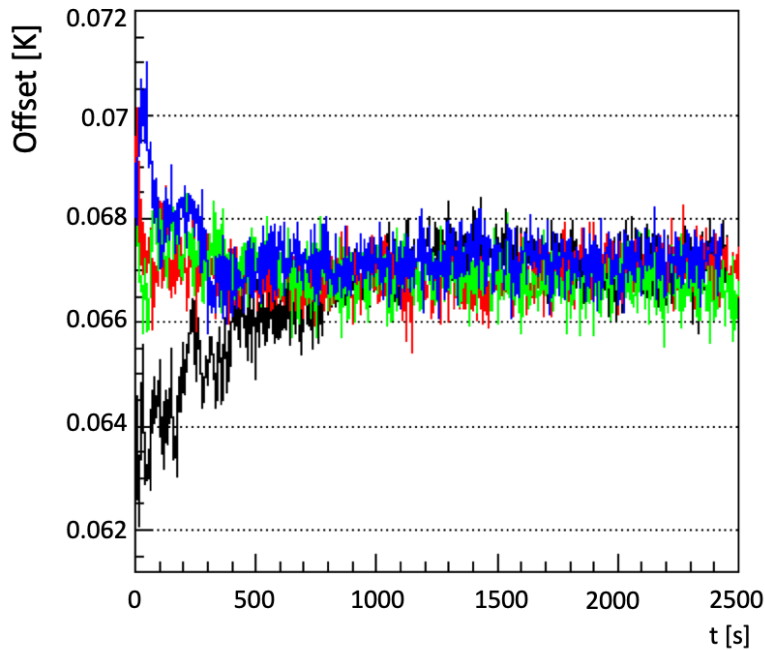


Figure 59: Temperature offset between the reference sensor and the three other sensors in a calibration set for the Static T-Gradient monitor. Offsets are shown as a function of time for four independent immersions in LAr with respect to the reference sensor. Within the time range used for the actual calibration (1000-2000 s), both fluctuations for a single immersion and difference between immersions are below 1 mK, demonstrating the performance and stability of the system and the robustness of the calibration procedure.

2071 sensors is contained inside the gas-tight enclosure shown in Figure 60-left. The stepper motor is
 2072 mounted on the outside of the enclosure. Vertical spacing is 10 cm for the five sensors at the top
 2073 and bottom, and 50 cm for the 14 sensors in the middle, where the bottom (top-most) sensor is 10
 2074 (750) cm from the bottom of the cryostat. Each sensor is soldered to a PCB. Cables are routed along
 2075 the carrier rod and connected to a flange with Sub-D connectors on both sides.

2076 The stepper motor engages with the carrier rod via a ferrofluidic dynamic seal and a pinion and
 2077 gear that converts the motor's rotational motion into linear motion of the rod without jeopardising
 2078 the integrity of the argon atmosphere inside the enclosure.

2079 The stepper motor can move the rod vertically, enabling temperature measurements at various
 2080 heights in the TPC, and at the same heights by different sensors. Assuming a stable temperature
 2081 profile over the calibration period of a couple of minutes, any offset in the temperature readings at
 2082 a given height by different sensors can be attributed to the intrinsic offset between the two sensors,
 2083 providing constants for their cross-calibration. By linking all adjacent sensors, it is possible to
 2084 calibrate out all offsets with respect to a single one and achieve precise measurement of the relative
 2085 vertical T-gradient. See Figure 60-right for the comparison of sensor readout before and after
 2086 calibration. As will be shown in Section 4.5.2, final confirmation of the robustness of the system

2087 was achieved during the “pump-off” detector period when the temperature became uniform over
2088 the detector height.

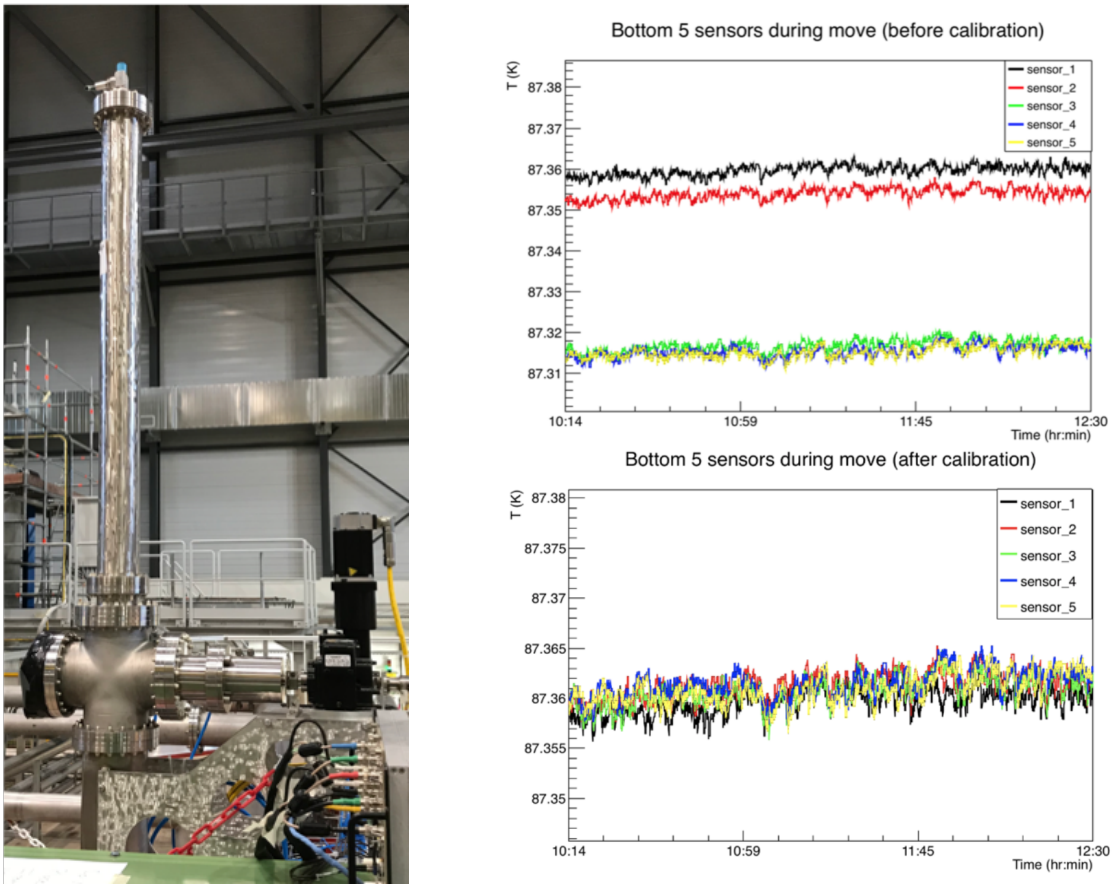


Figure 60: Left: Dynamic T-gradient monitor enclosure showing stepper motor on the side and viewports to visually check the motion of the system. The top part of the enclosure houses the carrier rod when the system moves up. Right: Temperature measurement by the bottom-most five sensors before and after cross-calibration

2089 **Temperature data analysis**

2090 The systems described above have been collecting data for more than two years, resulting in a deeper
2091 understanding of LAr dynamics inside a cryostat. Some important outcomes are discussed below.

2092 Stability studies show that except near the LAr surface the difference in temperature between
2093 any two sensors in the same T-Gradient monitor remains constant to within 3 mK, demonstrating
2094 the stability of the LAr system under standard operating conditions, and importantly, the reliability
2095 and longevity of the sensors.

2096 The slow and continuous process of progressively moving each sensor up (or down) to the
2097 location previously occupied by its neighbour is expected to yield a height profile that is effectively
2098 flat. Deviations from flatness would indicate a problem with one or more sensors.

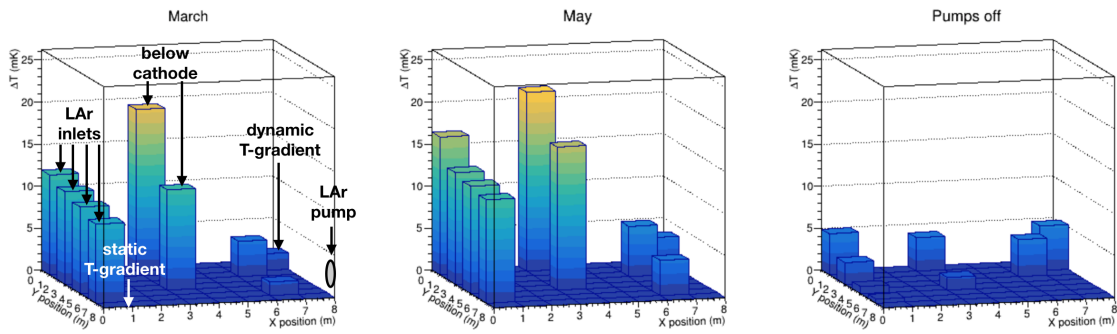


Figure 61: Temperature difference between the Static T-Gradient bottom sensor and the horizontal grid of sensors placed 40 cm apart over the bottom of the cryostat. Left and middle: temperature distribution with the recirculation system on. Right: temperature distribution when recirculating system is off.

2099 Vertical and horizontal cross-calibration profiles of the Dynamic T-Gradient monitor have
 2100 been compiled under various conditions (e.g., stable, with recirculation system on and off, at
 2101 different pressures). The pumps-off (i.e., no recirculation) measurements are particularly interesting
 2102 since small temperature gradients are expected and were in fact observed by the Dynamic T-
 2103 Gradient monitor (see Figure 62-left). The flatness of this profile to within a few mK illustrates the
 2104 homogeneity of LAr temperature. This measured homogeneity was used to re-calibrate the Static
 2105 T-Gradient monitor (this is the so-called “pumps-off” calibration method) and the result shows good
 2106 agreement with the laboratory calibration (see Figure 62-right).

2107 These studies have demonstrated significant differences in temperature based on whether the
 2108 recirculation system is on or off. These differences appear in both vertical and horizontal planes.
 2109 The grid of sensors placed 40 cm apart over the cryostat bottom shows a temperate peak (20 mK)
 2110 below the cathode plane with a decrease towards the pump on the bottom beam left when the
 2111 recirculation system is on (see Figure 61-left), and a more homogeneous distribution when it is off
 2112 (see Figure 61-right).

2113 Finally, Figure 63 shows a comparison of the vertical profiles (under stable conditions) to CFD
 2114 simulations for a variety of boundary conditions (e.g., varying flow rate and temperature of the
 2115 incoming LAr). The CFD model reasonably predicts the main features of the data, but some details
 2116 still need to be understood, e.g., the bump at 6.2 m and the lower measured temperature at the
 2117 bottom of the cryostat. More studies on CFD boundary conditions are needed.

2118 4.5.3 Cameras

2119 Cameras provide direct visual information about the state of the detector during critical operations
 2120 and when damage or unusual conditions are suspected. Cameras can be used to verify stability,
 2121 straightness, and alignment of the hanging TPC structures during cool-down and filling; ensure that
 2122 no bubbling occurs near the ground planes; and inspect the state of movable parts in the detector
 2123 (i.e., the dynamic temperature sensor). Eleven cameras were deployed in ProtoDUNE-SP at the
 2124 locations shown in Figure 64. They successfully provided views of the detector during filling and

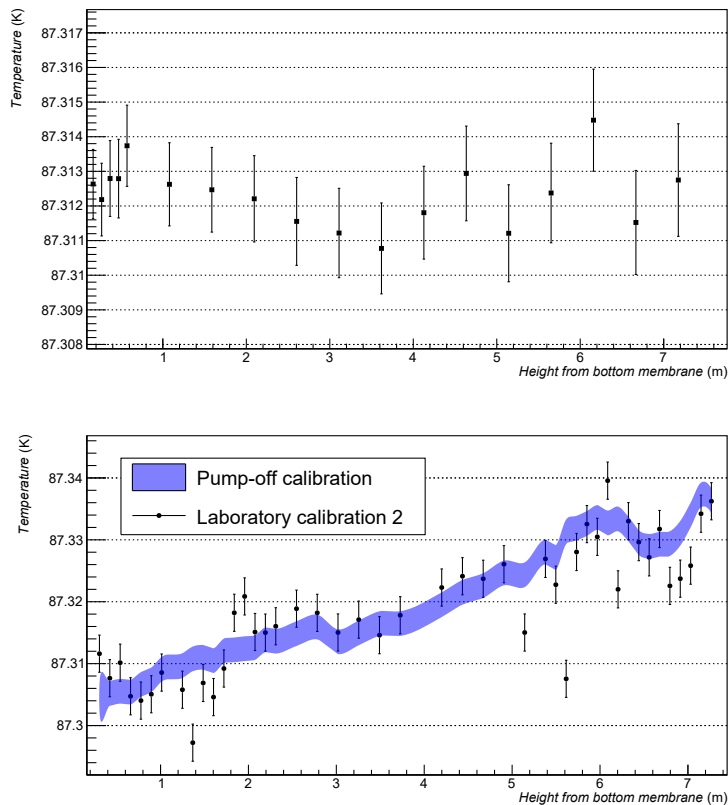


Figure 62: Top: Dynamic T-Gradient with no recirculation shows a flat profile. Bottom: Static T-Gradient while gas pressure is raised; comparison of laboratory calibration to “pumps-off” calibration.

2125 throughout its operations. Two types of cameras, were deployed, “cold” for fixed, long-term use
 2126 and “warm” for short-term inspections.

2127 **Fixed Cameras (cold)**

2128 The cold fixed cameras monitor the following items during filling:

- 2129 • positions of the corners of each APA, CPA, FC, and GP (1 mm resolution);
- 2130 • relative straightness and alignment of the APAs, CPA, and FC ($\pm 1^\circ$)
- 2131 • relative positions of profiles and endcaps (0.5 mm resolution); and
- 2132 • the LAr surface, specifically, the presence of bubbling or debris.

2133 One design for the ProtoDUNE-SP fixed cameras uses an enclosure similar to the successful
 2134 EXO-100 design [35], see Figure 65. Cameras 101, 102, 104, and 105, shown in Figure 64,
 2135 were installed in this type of enclosure. A thermocouple in the enclosure allows temperature
 2136 monitoring, and a heating element provides temperature control. SUB-D connectors are used at the

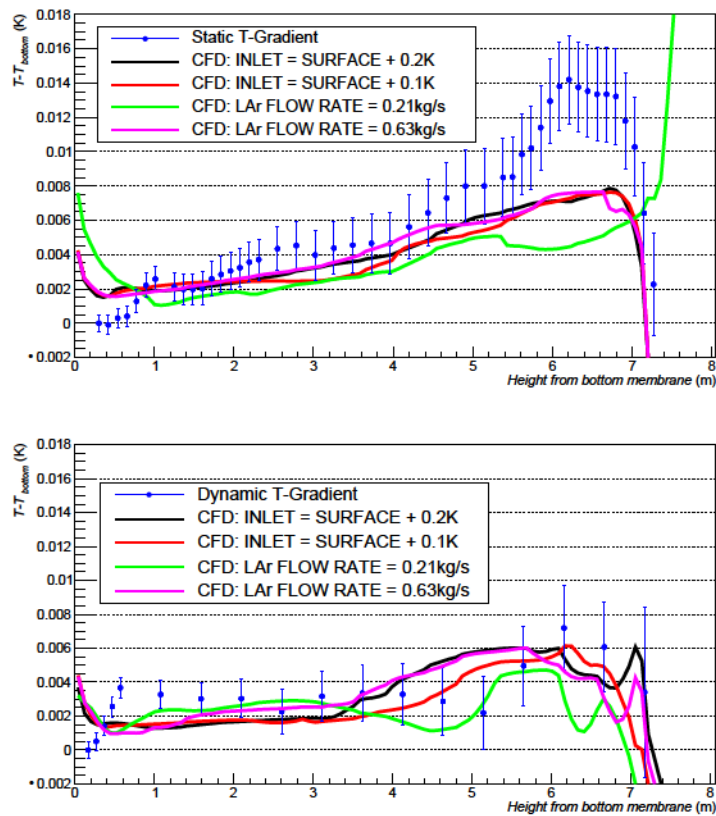


Figure 63: Temperature profiles measured by the T-gradient monitors and comparison to the CFD model with different boundary conditions. Top: Static T-gradient monitor; Bottom: Dynamic T-gradient monitor. Unless specified, LAr flow rate is nominal, 0.42kg/s.

2137 cryostat flanges and the camera enclosure for signal, power, and control connections. An alternative
 2138 successful design uses an acrylic enclosure, see Figure 65, bottom left. Cameras 001, 002, 004,
 2139 and 005, shown in Figure 64, are placed in acrylic enclosures. All have operated successfully.

2140 **Inspection Cameras (Warm)**

2141 The inspection cameras are selected to be as versatile as possible to cover the range of intended
 2142 uses. The following inspections have been done with the warm cameras:

- 2143 • status of HV-feedthrough and cup,
- 2144 • status of FC profiles, endcaps (0.5 mm resolution),
- 2145 • vertical deployment of calibration sources,
- 2146 • status of thermometers, especially dynamic thermometers,
- 2147 • HV discharge, corona, or streamers on HV feedthrough, cup, or FC,

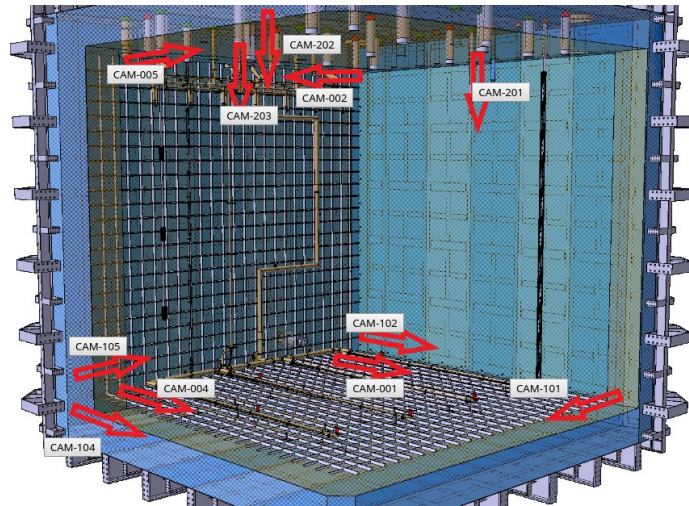


Figure 64: A 3D view showing the locations of the 11 cameras in ProtoDUNE-SP.

- 2148 • relative positions of profiles and endcaps (0.5 mm resolution), and
 2149 • sense wires at the top of the outer APA wire planes (0.5 mm resolution).

2150 Unlike the fixed cameras, the inspection cameras operate only during an inspection. It is more
 2151 practical to use commercial cameras for this purpose, which requires keeping the cameras warmer
 2152 than -150 C during deployment. Cameras of the same commercial model were used successfully
 2153 to observe discharges in LAr from a distance of 120 cm [36].

2154 In this design, the warm camera is contained inside a gas-tight acrylic tube inserted into the
 2155 feedthrough, and can be removed for servicing, upgrade, or replacement at any time. Figure 66
 2156 shows an acrylic tube enclosure and camera immediately before deployment. These acrylic tube
 2157 enclosures were deployed at the positions marked 201, 202, and 203 in Figure 64, and equipped with
 2158 cameras with fish-eye lenses during initial operation. One camera was then successfully removed
 2159 without any evidence of having contaminated the LAr. The other cameras were left in and used
 2160 during post-beam operations.

2161 **Light-emitting system**

2162 The light-emitting system uses LEDs to illuminate the parts of the detector in the cameras' fields of
 2163 view with selected wavelengths (IR and visible) that the cameras can detect. Performance criteria
 2164 for the light-emission system include the light-detection efficiency of the cameras and the constraint
 2165 on heat generation inside the cryostat. Very high-efficiency LEDs help reduce heat generation; a
 2166 750 nm LED [37] with a specification equivalent to 33% conversion of electrical input power to
 2167 light was used.

2168 One set of IR-LEDs is mounted directly under camera 002 near the beam-left manhole, shown
 2169 in Figure 67. It is constructed from the IR LED modules that were removed after the initial
 2170 operation. Each LED module has 30 LEDs. This set of LEDs draws about 2.4 A of current at 12 V

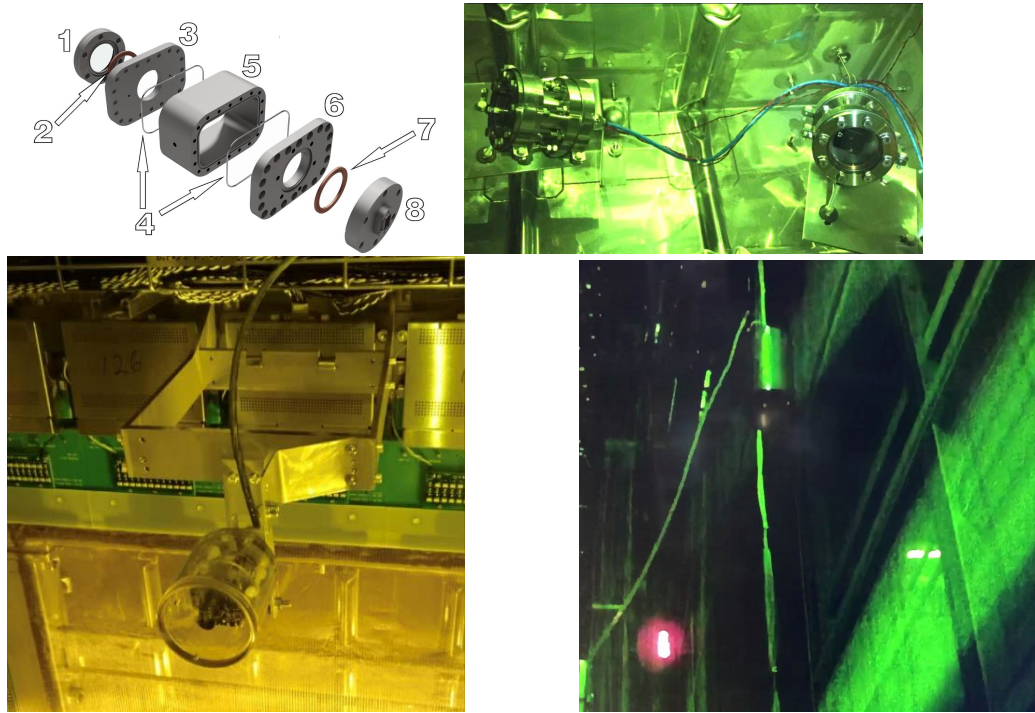


Figure 65: Top left: a CAD exploded view of a vacuum-tight camera enclosure suitable for cryogenic applications [35]. Its numbered features are (1) quartz window, (2 and 7) copper gasket, (3 and 6) flanges, (4) indium wires, (5) body piece, (8) signal feedthrough. Top right: two of the ProtoDUNE-SP cameras in stainless steel enclosures similar to the CAD design on the top left. Bottom left: one of the cameras in an acrylic enclosure. Bottom right: a portion of an image taken with camera 105 showing a purity monitor mounted outside the APA on the beam-left side. This photo was taken with ProtoDUNE-SP completely filled.

2171 at room temperature, and about 1.8 A in LAr. The assembly is installed vertically, with the LEDs
 2172 aimed upstream of the beam entry behind the beam left APAs. When powered, the centres of the
 2173 LEDs have a slight red glow.

2174 Additionally, chains of LEDs connected in series and driven by a constant current are used for
 2175 broad illumination (see Figure 67 right), with each LED paired in parallel with an opposite polarity
 2176 LED and a resistor (see Figure 68). This provides two different wavelengths of illumination by
 2177 simply changing the direction of the drive current, and allows continued use of the chain even if an
 2178 individual LED fails.



Figure 66: A photo of the ProtoDUNE-SP warm inspection camera acrylic tube immediately before installation; the acrylic tube is sealed with an acrylic dome at the bottom and can be opened at the top.

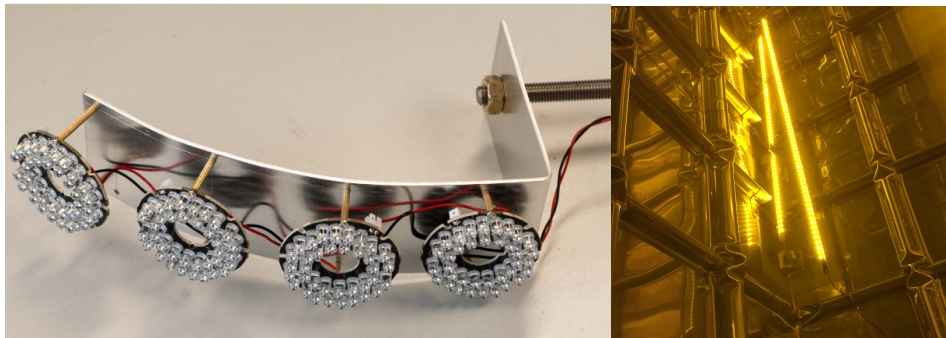


Figure 67: Left: Mounting of IR-LEDs to be placed directly under camera 002 near the beam-left manhole. Right: LED strip used for broad illumination

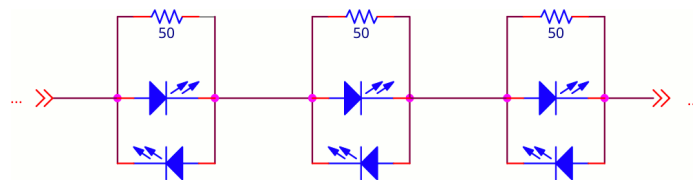


Figure 68: Example schematic for the LED chain, providing failure tolerance and two LED illumination spectra.

2179 5 Detector Assembly, Testing and Installation

2180 5.1 Detector Assembly

2181 The detector materials arrived at the EHN1 building in containers shipped from the production sites.
2182 The majority of the assembly and testing for ProtoDUNE-SP took place in the NP04 clean room
2183 inside EHN1. This space is equipped with a rail system to hang detector components, and move
2184 them into the integrated cold test stand, the cold box, and eventually into the cryostat for installation.
2185 Figure 69 shows the rail system and cold box in the clean room. The clean room satisfies the ISO-8
level of cleanliness and is equipped with filtered lights used to protect the photon detector coating.

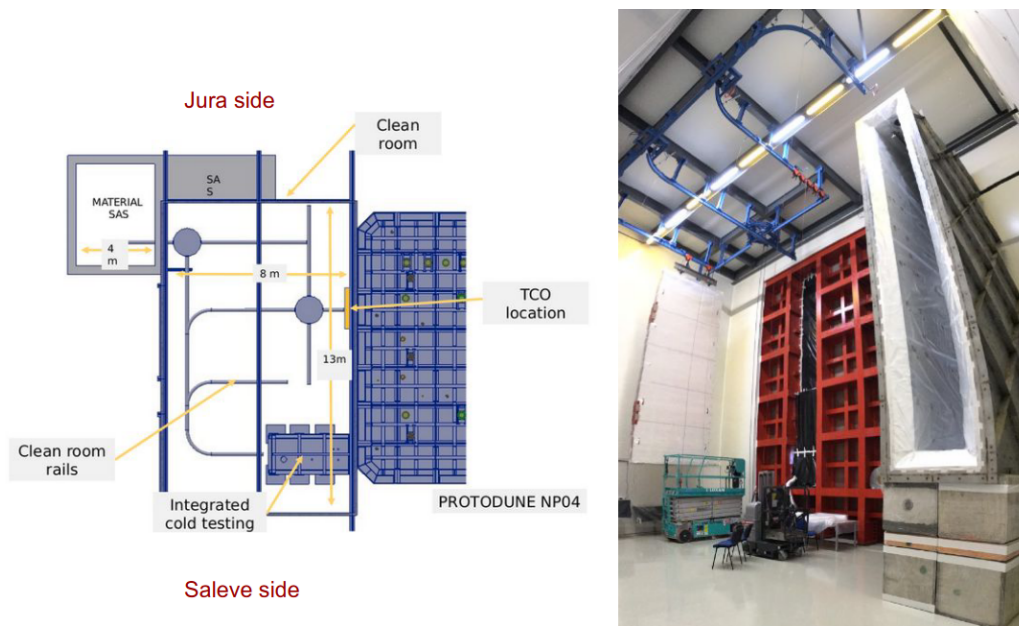


Figure 69: Left: Schematic of the NP04 clean room showing the rail system, cold box, and its orientation with respect to the cryostat. Right: A photograph taken inside the NP04 clean room. The blue structure attached to the roof is the rail system. It is shown supporting a (still covered) APA at left. The tall metal box on the right is the cold box.

2186
2187 As detector materials for ProtoDUNE-SP were brought into EHN1, they were passed into the
2188 material “sas” (the buffer zone between the EHN1 hall and the clean room) through its removable
2189 roof, unpacked and/or cleaned as necessary, hung from the rail system, then transported through a
2190 set of large doors into the clean room testing and assembly area where the following activities took
2191 place:

- 2192 • attachment of FC assemblies to CPA modules;
- 2193 • unpacking and testing of the PDS elements, and installation on the APA frames;
- 2194 • unpacking and testing of the CE elements, and mounting on the APAs;
- 2195 • integrated testing of APA with PDS and CE; and

2196 • when ready, passage through the temporary construction opening (TCO) in the side of the
2197 cryostat for installation.

2198 **5.1.1 APA Preparation and Integration**

2199 As each arriving APA container is opened inside EHN1, special lifting fixtures are attached to each
2200 end of the APA, then attached to two conveyances that lift the APA out of the container, and rotate
it 90° to vertical. The sequence is shown in Figure 70.



Figure 70: Arrival of an APA in EHN1 and its positioning. The upper left image shows the orientation of the APA as delivered, the lower right shows its vertical orientation when it is lowered into the material sas.

2201

2202 Once an APA is properly oriented, the lifting strap and fixtures are removed from its lower
2203 edge, the roof hatch on the material sas is opened, and the APA is lowered through the hatch. It is
2204 then transferred to a rolling trolley attached to a series of rails, and moved into the clean room. The
2205 APA then goes through a series of acceptance tests for both electrical integrity and wire tension, as
2206 well as an inspection for broken wires or any other damage that could have resulted from shipment
2207 and handling. At this stage, survey of the APA geometry was also performed.

2208

2209 Next, ten photon detectors (PDs) are inserted into alternating sides of the APA frame, five from
2210 each direction. After insertion, a PD is attached mechanically to the APA frame with fasteners,
2211 and a single electronics cable is attached and strain-relieved. Each PD is tested immediately after
2212 installation to ensure proper operation and to verify the cable readout. The design model and a
2213 photograph of an APA in the clean room during PD installation are shown in Figure 71.

2213

2214 After PD installation, CR boards are mounted on the geometry boards then 20 cold electronics
2215 (CE) boxes are installed at the top of the APA frame. Figure 72 indicates the location of the CE boxes
2216 on the APA and shows them being installed. These boxes are connected via matching electrical
2217 connectors on the FEMB. Mechanical fasteners affix the CE enclosure to brackets supported by
2218 the APA frame. Prior to their installation, the CE boxes undergo testing several times at room
2219 temperature for noise and channel response. Only those that are fully functional and have ENC
levels typical for room temperature operations, 1000 – 1500 e⁻, are installed on the APA.

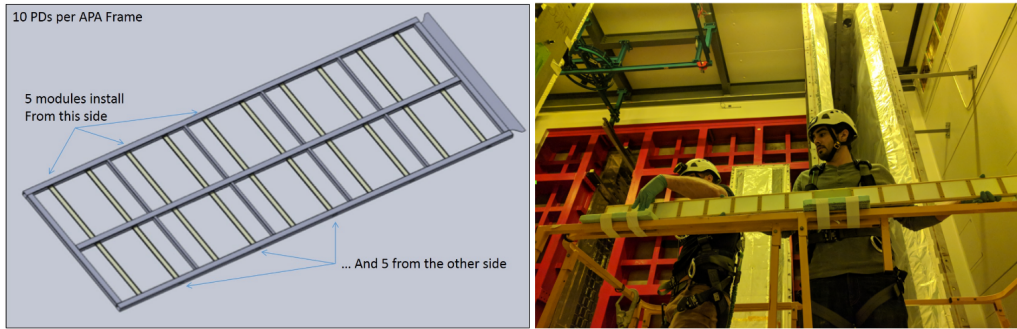


Figure 71: Left: PD slots (yellow) on the APA frame. Right: Installation of PDs on an APA.

2220 The details of the warm tests and their results can be found in [38]. In addition to the TPC
 2221 read-out electronics, each CE box includes a bundle of data and power cables that connect the
 2222 electronics to WIEC (warm interface electronics crate). Cable bundles were grouped together at
 2223 appropriate lengths for the WIEC connections, and secured on the cable trays.

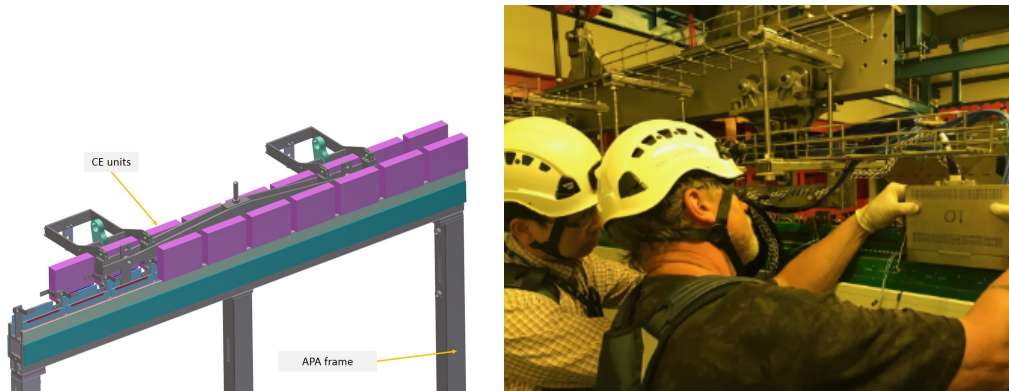


Figure 72: CE installation.

2224 At this point, the APA is moved via the rails to the integrated cold test stand where the warm
 2225 and cold tests are performed (see Section 5.3).

2226 After completing the cold test procedure the APA is slowly warmed up back to room tem-
 2227 perature. Then the cold box is opened, the cables are disconnected and secured, and the APA is
 2228 extracted from the box on the rail system, ready to be moved into the cryostat and positioned for the
 2229 final installation. Installation inside the cryostat is described later in this section.

2230 5.1.2 CPA, Field Cage Preparation and Integration

2231 Upon arrival at EHN1, each individual CPA module, weighing roughly 24 kg, is lifted out of its
 2232 shipping crate by hand.

2233 Three 1.16 m wide, 2 m tall CPA modules are placed on a flat table surface and screwed/pinned
 2234 together end-to-end to form a 6 m tall CPA column. Then a crane attaches at the top end of the CPA
 2235 column with appropriate lifting straps and shackles, and rotates it to vertical.

2236 As each successive CPA column is ready, it is affixed adjacent to the previous one lengthwise
2237 with 1 mm separation. Alignment is provided by two pins located on one side of each CPA that fit
2238 into a vertical slot on the adjoining side of the next CPA.

2239 Three basic elements comprise the FC: the top, bottom and end-wall FC assemblies. The top
2240 and bottom FC assemblies are effectively mirror assemblies that are hinged from the top and bottom
2241 of the CPAs, respectively. Figure 73 (upper left) is a schematic of a top/bottom FC assembly in
2242 which the ground plane covers one side of the field-shaping profiles. The upper right image in the
2243 figure illustrates a CPA pair with top and bottom FCs attached. The lower two images show units
2244 constructed inside the NP04 clean room.

2245 An end-wall FC assembly includes four stacked end-wall FC modules, stacked via the overhead
2246 hoist near the TCO. Figure 74 shows two images of an end-wall module, the design model and an
2247 assembled unit hanging on the rail system inside the clean room. Each of these assemblies was
2248 moved into the cryostat via the rails and positioned on the appropriate beam in the detector support
2249 system (DSS). The end-wall FC is supported by a spreader bar (hung from the same beam) that can
2250 swivel about the support point in order to allow proper positioning with respect to the APA and
2251 CPA.

2252 5.2 Detector Installation

2253 The detector installation steps as performed for ProtoDUNE-SP are outlined below.

- 2254 • Each of the six instrumented and tested APAs was moved into the cryostat through the TCO
2255 and transferred onto the appropriate rail in the DSS . They were then assembled into the two
2256 anode planes (Salève (south) side and Jura (north) side), of three APAs each.
- 2257 • Signal cables from the TPC read-out electronics boards and from the PD modules were routed
2258 up to the cryostat roof and connected to the CE and PD flanges on the cryostat. Figure 75
2259 shows three Salève-side APAs hung next to the TCO opening, connected and ready to be
2260 pushed into their final installation position.
- 2261 • After the first row of APAs was in place on the Salève side, the bridge beam holding the
2262 APAs was bolted into place. Then the two end walls for the Salève-side drift volume were
2263 constructed and moved inside the cryostat, supported by another bridge beam. The left image
2264 in Figure 76 shows the two end-wall units in the cryostat ready for final installation.
- 2265 • Each assembled FC and CPA column was then moved into the cryostat, supported by its
2266 own bridge beam. Figure 76 shows the three CPA/FC units ready to be installed inside the
2267 cryostat.
- 2268 • Once the CPA/FC beam was bolted into position, the end-walls were mounted on the end-
2269 wall hangers and the spreader bars that were used to manipulate and move end-walls were
2270 removed.
- 2271 • The FC units in the Salève-side drift volume were deployed as shown in Figure 77.
- 2272 • After the Jura-side row of APAs were installed, the two end-walls for the Jura-side drift
2273 volume were constructed and moved inside the cryostat, supported by their own bridge beam.

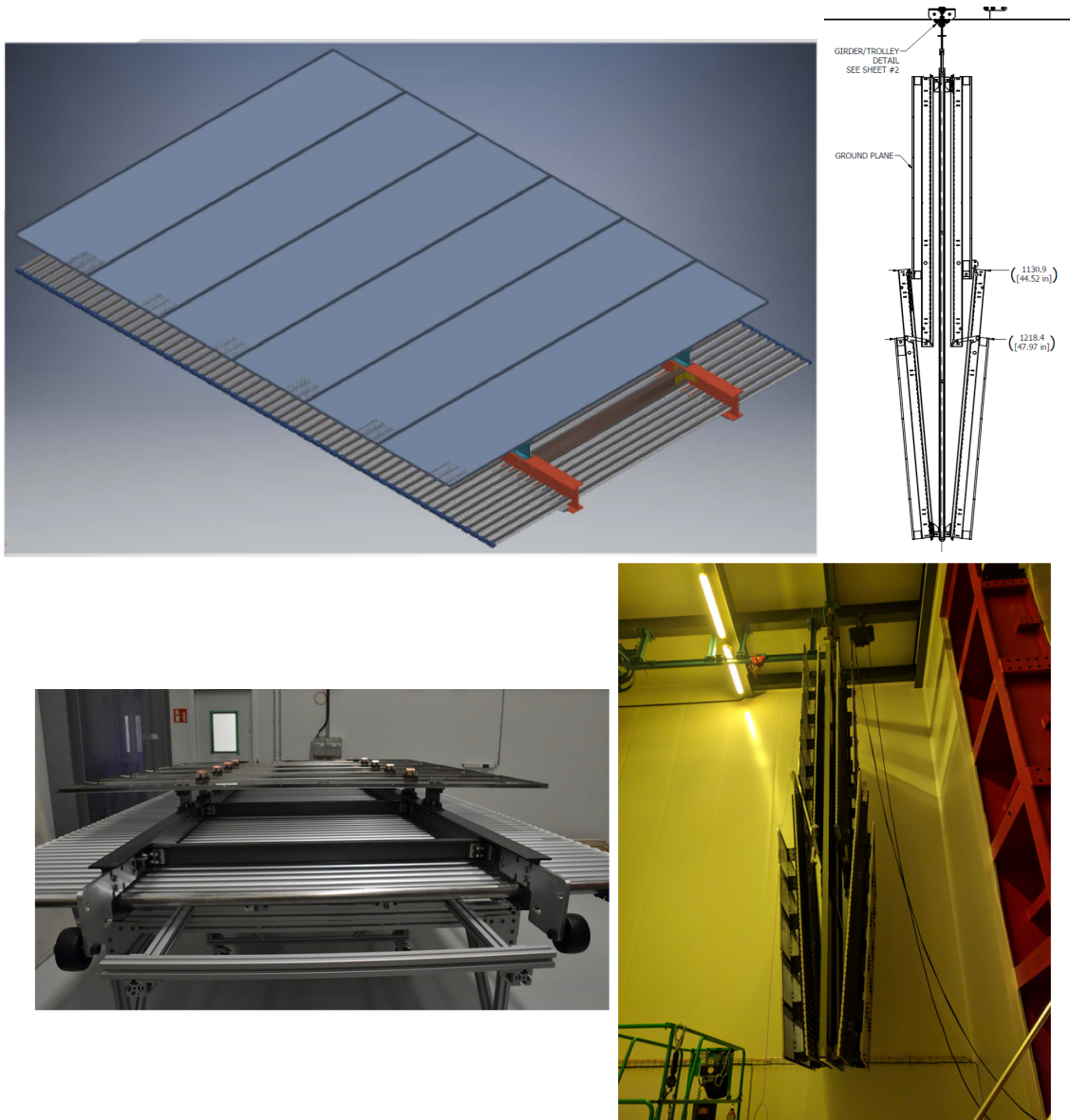


Figure 73: Top Left: top or bottom FC assembly (they are symmetrical). Top Right: side view of a CPA pair with four FC assemblies (two top and two bottom) attached. Bottom: Photographs of an assembled pair of CPA columns with its four FC assemblies.

- 2274
- At this point all the TPC components were inside the cryostat and the TCO was closed.
- 2275
- Then the end wall in the Jura-side drift volume were placed into position on their hangers
- 2276
- and the FC units were deployed.

2277 **5.3 Cold Box Tests**

2278 The cold box is a large insulated container that provides electrical isolation, light tightness, and
 2279 an environment for conducting CE and PD tests on a single instrumented APA at both room and

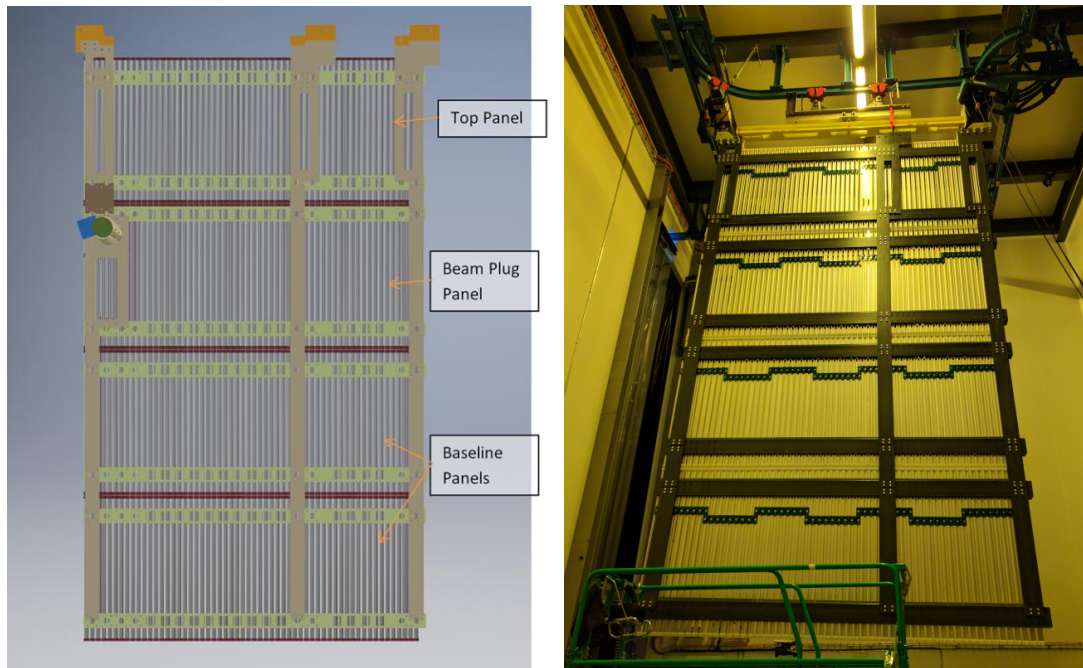


Figure 74: Left: Design model of the FC end wall panel. Right: Finalized assembly of one of the FC end wall panels.

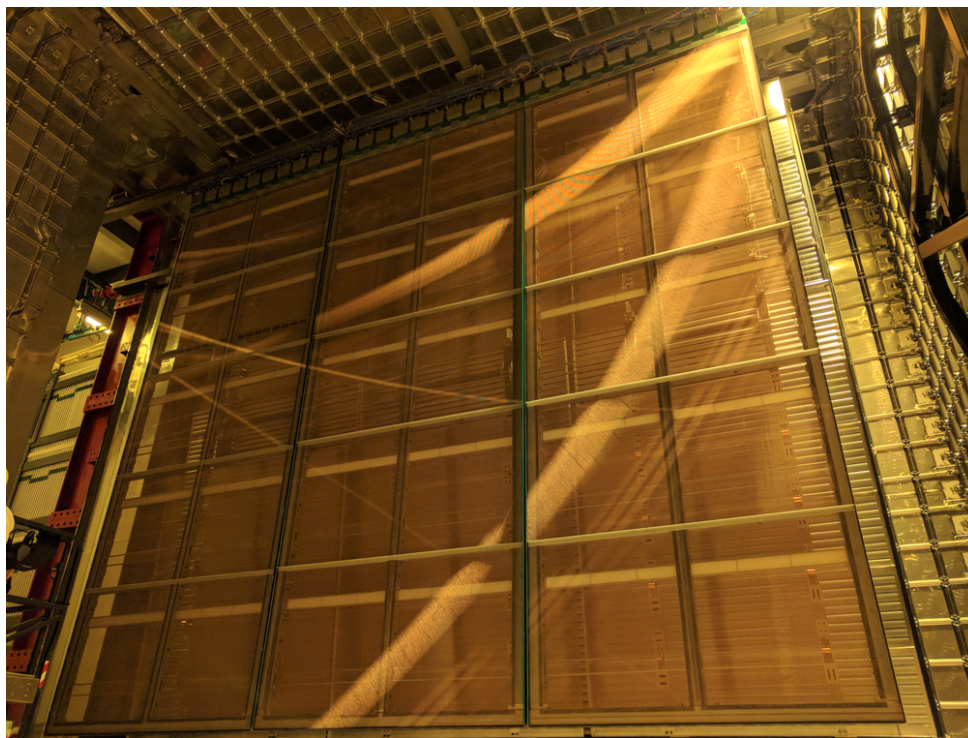


Figure 75: Three APAs installed and mechanically connected inside the cryostat.



Figure 76: . Left: Salève-side drift FC end-walls are ready to be deployed inside the cryostat. Right: CPA and FC assemblies inside the cryostat ready to be pushed to their final position.



Figure 77: Field cages deployed in the Salève-side drift volume.

2280 cryogenic temperatures. Figure 78 shows a model and photographs of the cold box with an APA. At
 2281 the top of the box, a crossing tube with a ConFlat fitting, similar to those in the cryostat, connects
 2282 to the warm-cold interface flange for the PD and CE cable connections. Once the cables are routed
 2283 and connected to their flanges, and an APA is moved inside, the end cap that completes the Faraday
 2284 cage is put in place, closing the box.

2285 The cooling system is designed to first purge the cold box with dry gas then cool the volume
 2286 slowly to 150 K using cold nitrogen gas, and maintain the inner volume at that temperature for
 2287 approximately 48 hours. The cool-down rate, the same as that used for the cryostat, was less than
 2288 10 K/hr.

2289 The first set of tests on each APA in the cold box was performed at room temperature to evaluate

2290 the ENC performance of each channel with different gain and shaping times. After cool-down, a
2291 full set of tests was performed on each APA at low temperature to assess functionality and electronic
2292 noise. Upon completion, the system slowly warmed the cold box volume back to room temperature.
2293 At this point, the cold box was opened, the cables were disconnected, and the APA was extracted
2294 from the box onto the rail system, and assuming it passed the tests, into the cryostat for installation.

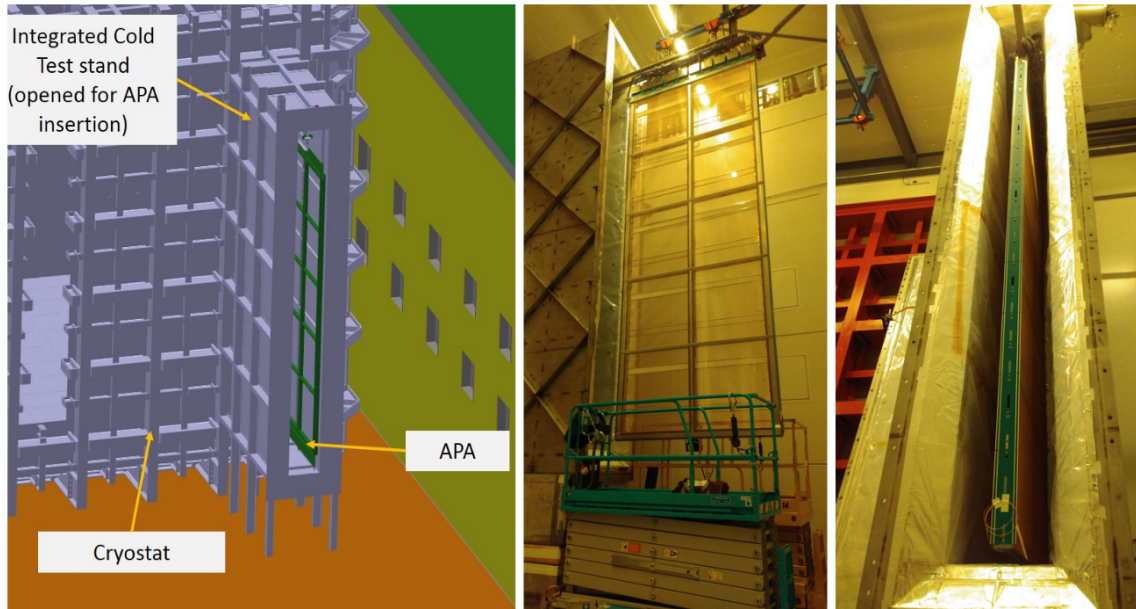


Figure 78: Left: A model of the cold box in the ProtoDUNE-SP clean room. Middle: An APA in front of the cold box ready to be inserted for testing. Right: An APA inserted into the open cold box.

2295 The measured temperature dependence of the ENC noise is shown in Figure 79. The measured
2296 ENC was 1100 e at room temperature for the collection plane and it dropped to 400 e at
2297 cryogenic temperatures [38]. This agrees with the values measured in standalone tests.

2298 **5.4 Grounding and Shielding**

2299 To ensure adequate sensitivity of the ProtoDUNE-SP detector, two distinct grounding systems,
2300 a detector ground and a building ground, were put in place to isolate it from all other electrical
2301 systems and equipment, and to minimise the influence of inductive and capacitive coupling and
2302 ground loops.

2303 The detector ground consists of the steel cryostat outer vessel, the cryostat inner membrane, and
2304 all metal structures attached to or supported by the cryostat. The building ground encompasses the
2305 network of grounding bus bars and interconnected rebar previously installed in ENH1. A 1 mm
2306 thick sheet of G10 is installed between the concrete floor and the bottom of the cryostat to provide
2307 an insulating barrier and to minimise low-frequency ground and noise currents between the detector
2308 and building grounds.

2309 Detector readout racks are placed on or near the top of the cryostat to put them on the common
2310 detector ground and minimise the cable runs. All cryogenics and gas piping is connected to the

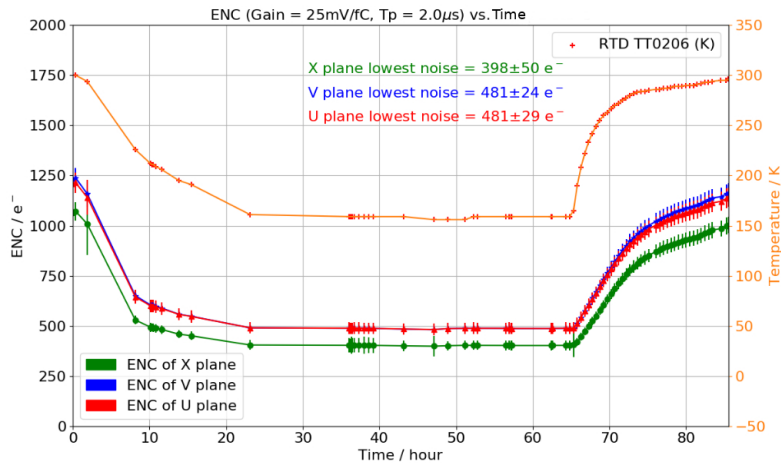


Figure 79: ENC performance in electrons of the APA+CE as a function of time during the cold box test; red/blue are the induction (U/V) wire planes, and green is the collection (X) wire plane. The orange curve shows the temperature measurements taken nearest the CE Boxes.

2311 building ground at regular intervals. Dielectric breaks are installed on these pipes near the top of
 2312 the cryostat.

2313 To avoid structural ground loops inside the cryostat, the APA frames are insulated from each
 2314 other. Each frame is electrically connected to the cryostat at a single point on the CE feedthrough
 2315 board in the signal flange where the cables exit the cryostat. Mechanical suspension of the APAs is
 2316 accomplished using insulated supports.

2317 The analog portion of each FEMB contains eight front-end (FE) ASICs configured as 16-
 2318 channel digitising charge amplifiers. The ground terminals on the ASICs' input amplifiers are
 2319 connected to the APA frame. All power-return leads and cable shields are connected to both the
 2320 ground plane of the FEMB and to the signal flange.

2321 Filtering circuits for the APA wire-bias voltages are locally referenced to the ground plane of
 2322 the FEMBs through low-impedance electrical connections. This approach ensures a ground-return
 2323 path in close proximity to the bias-voltage and signal paths. The close proximity of the current
 2324 paths minimises the size of potential loops to further suppress noise pickup.

2325 PD signals are carried directly on shielded, twisted-pair cables to the signal flange. The cable
 2326 shields are connected to the cryostat at a second feedthrough, the PDS feedthrough, and to the PCB
 2327 shield layer on the PDs. There is no electrical connection between the cable shields and the APA
 2328 frame except at the signal flange.

2329 The frequency domain of the TPC wire and PD signals are separate. The wire readout digitises
 2330 at 2 MHz with 500 kHz bandwidth at 1 sec peaking time, while the PD readout operates at
 2331 150 MHz with 10 MHz bandwidth. They are separated from the clock frequency (50 MHz)
 2332 and common noise frequencies through the FE ASIC and cabling designs. All clock signals are
 2333 transmitted separately with individual shields to avoid interference from power lines.

2334 **6 Detector Readout and Control**

2335 **6.1 Data Acquisition**

2336 The function of the DAQ System is to orchestrate the physics data taking. It collects data from the
2337 sub-detectors and the Cosmic Ray Tagger (CRT), and conveys the event data files and metadata to
2338 the offline computing system. An important aspect of the DAQ is its triggering system. The Central
2339 Trigger Board (CTB) receives signals from the Photon Detector readout electronics, the CRT and
2340 the beam instrumentation detectors, and forms trigger candidates. The timing system receives
2341 those trigger candidates, applies dead-time rules, and forms a global trigger signal associated with
2342 a unique timestamp. It then distributes the trigger to the detector electronics and to other DAQ
2343 components in such a way that all recorded data corresponding to a fixed time-window around
2344 the trigger timestamp can be captured. Dedicated software applications take care of acquiring the
2345 data from the readout electronics and packaging it appropriately into files that are kept in a local
2346 temporary storage (in the DAQ cluster) awaiting their transfer to permanent storage, which is at
2347 both CERN and at Fermilab.

2348 The DAQ software is also responsible for other functions, including the delivery of configuration
2349 parameters to the front-end electronics, the overall Run Control and the real-time monitoring of
2350 the data quality and performance of the DAQ system. Figure 80 illustrates the DAQ system and its
2351 interconnections.

2352 Due to the extremely tight construction and commissioning schedule of ProtoDUNE-SP, the
2353 DAQ has been designed to use commercial off-the-shelf (COTS) components and readily available
2354 electronics boards: the notable exceptions are the CTB and the timing system, which were custom
2355 developed for ProtoDUNE-SP. Most of the implemented solutions for the firmware and software
2356 are based on existing frameworks and generic technologies.

2357 The DAQ system design is driven by the need to support both the TPC and PDS front-end
2358 electronics, which have very different behaviors. TPC data are streamed out at 2 MHz without zero
2359 suppression. This allows for the acquisition of an unbiased dataset to be used offline to study data
2360 reduction methods for DUNE-SP. The photon detector electronics, on the other hand, applies a
2361 local threshold to the signals and sends to the DAQ only waveform data that are either above this
2362 threshold or that match an external trigger timestamp.

2363 The DAQ design is also constrained by the amount of data that can be transferred to the offline
2364 computing system for permanent storage. To down-scale the acquired data volume, the trigger
2365 system supports selection of data using inputs from the beam instrumentation detectors and the
2366 CRT.

2367 Finally, the DAQ system is designed to support partitioning so that detector components can
2368 operate independently; this is particularly relevant for dedicated commissioning and calibration
2369 runs.

2370 **Data rate**

2371 At 430 Gb/s, the TPC electronics data dominates the data volume. For the six APAs, data pass
2372 through a set of 30 Warm Interface Boards (WIBs), located on the cryostat flanges, on their way to
2373 the DAQ.

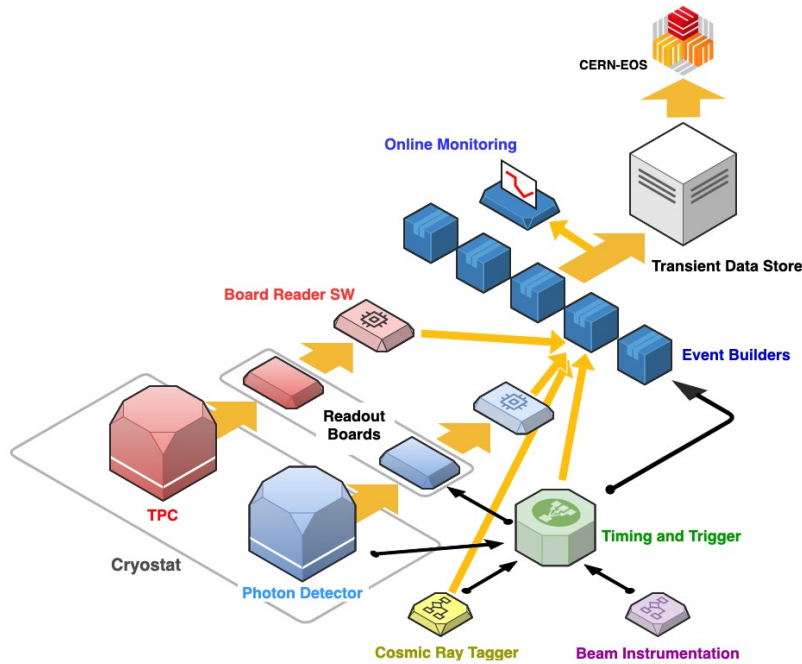


Figure 80: Overview of the DAQ system illustrating its interconnections, data flow, timing and trigger signals, and the interfaces to the front-end electronics and offline computing systems. The TPC readout systems (RCE and FELIX) receive data from the WIBs, which are then compressed and selected based on trigger information. Triggered data are then sent to the event-building farm and subsequently stored to disk. In parallel, a sample is prepared for online monitoring. Triggers are formed using inputs from the beam instrumentation, the PDS, and the CRT.

2374 PDS data is collected by an array of 24 SSPs, and consists of a combination of externally
 2375 triggered events and self-triggered events. The self-triggered data rate is tuned through the bias
 2376 voltage settings to aim for a data rate into the DAQ of 3 Gb/s. The externally triggered data
 2377 contribute much less than 1 Gb/s.

2378 The DAQ was set up for a target trigger rate of 25 Hz for the beam run, with a readout window
 2379 of up to 5 ms. These values were chosen to ensure that the bandwidth would stay well within
 2380 the maximum of 20 Gb/s for data transfer from the ProtoDUNE-SP online system to CERN's
 2381 OpenSource Storage (EOS) [39]. Using data compression, the typical beam data DAQ output
 2382 bandwidth in ProtoDUNE-SP was on the order of 5 – 8 Gb/s.

2383 The Timing System

2384 The timing system provides a stable and phase-aligned master clock for all the DAQ components.
 2385 In ProtoDUNE-SP, a GPS-disciplined oscillator sends high-quality clock signals to an FPGA-based
 2386 master unit, and the trigger system and SPS accelerator send external signals to it. The master
 2387 unit multiplexes the synchronisation and trigger commands into a single encoded data stream. This
 2388 stream gets broadcast to all timing endpoints (the WIBs, the SSPs and the DAQ components) that
 2389 require it, and is decoded into separate clock and data signals, ultimately providing synchronous
 2390 triggers and timing signals to all endpoints.

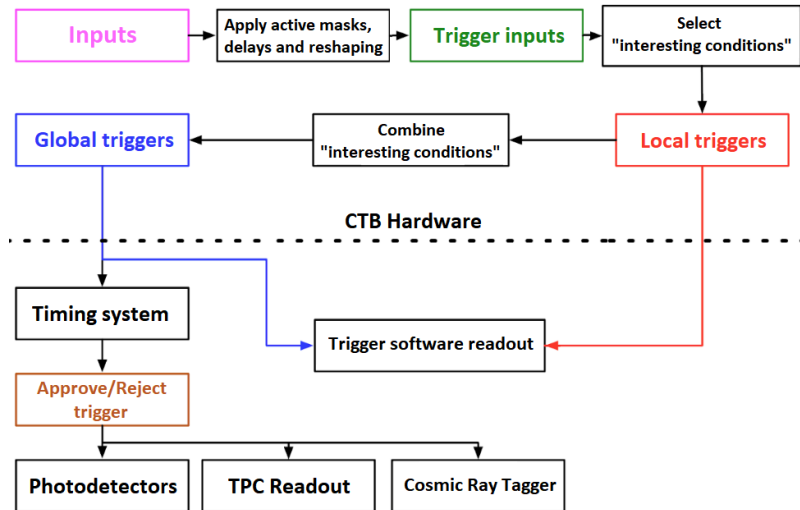


Figure 81: The Central Trigger Board (CTB) is designed to receive triggers from various subsystems and combine them into a global trigger based on a configurable input mask (or more sophisticated algorithm, if desired). The CTB provides functionality to time-stamp triggers globally, keep event counts, and provide information such as trigger type and error conditions.

2391 Trigger system

2392 Figure 81 illustrates the trigger system logic. The Central Trigger Board (CTB) receives information
 2393 from the beam instrumentation, photon detectors, and the cosmic ray tagger (CRT), and forms
 2394 trigger candidates that are passed on to the timing system. Due to the high rate of cosmic rays, the
 2395 photon detector trigger inputs were not used in the trigger logic for ProtoDUNE-SP. After applying
 2396 any dead-time conditions, the timing system generates a global trigger signal and distributes it
 2397 to the WIBs, the SSPs, and to the DAQ components, as needed. A simple dead-time logic was
 2398 implemented for ProtoDUNE-SP that kept triggers at least 10 ms apart from each other to ensure
 2399 that the readout windows of two consecutive triggers would never overlap and to avoid rate spikes
 2400 above 100 Hz.

2401 The CTB is designed around the MicroZed System-on-Chip (SoC) board, equipped with a
 2402 Xilinx Zynq7020. The motherboard implements the hardware interface to the various systems, the
 2403 FPGA implements trigger logic and interfaces with the timing, and the CPU and software elements
 2404 manage the FPGA configuration and the communication with DAQ software. This solution supports
 2405 up to 100 separate inputs that can be combined into a global trigger based on a configurable input
 2406 mask (or more sophisticated algorithm, if desired). The firmware is designed to be suitably flexible
 2407 such that the exact trigger selection can be decided at configuration time. Regardless of the trigger
 2408 configuration, the decision is made in under 1 μ s.

2409 Readout systems

2410 ProtoDUNE-SP is equipped with three readout systems, two for the TPC and one for the PDS.
 2411 The two TPC solutions, ATCA-based RCE and PCIe-based FELIX, are implemented for testing
 2412 purposes.

2413 The Reconfigurable Cluster Elements (RCE) [40] based readout, developed by the SLAC
2414 National Accelerator Laboratory, is a full meshed distributed architecture, based on networked
2415 SoC elements on the ATCA platform. The RCE was chosen as the baseline readout solution
2416 for ProtoDUNE-SP since it had already been successfully used in the 35 ton prototype [41], and
2417 during ProtoDUNE-SP's beam run it read out five of the six APAs (12,800 channels). RCE-
2418 based readout focuses on early data processing, with tightly coupled custom firmware and software
2419 implementations. The ProtoDUNE-SP version of the RCE accepts digitized raw data from the WIBs
2420 over optical fibre. The primary processing functions of the RCEs are compression and buffering
2421 of the raw data. The RCEs send the data to the back-end upon receipt of an external trigger. An
2422 output data rate of 1 Gb/s per RCE can be sustained and a compression factor of four has been
2423 achieved [42].

2424 The Front-End LIInk eXchange (FELIX) readout system, a project initially developed within
2425 the ATLAS Collaboration at CERN [43], is centered around Peripheral Component Interconnect
2426 Express (PCIe) technology. The FELIX design aims to minimise the need for custom hardware
2427 and firmware development and rely instead on commodity servers, networking, and software. The
2428 FELIX PCIe card streams data arriving from the detector front-ends into a circular memory buffer
2429 in a host PC using a continuous direct memory access (DMA) transfer (with fixed 4 kB block size).
2430 From this stage onward, all data processing is done by software executed on networked servers. Data
2431 compression can be offloaded from the CPUs through embedded hardware acceleration modules
2432 (Intel QuickAssist (QAT) [44]) in order to achieve the required processing performance. Due to the
2433 potential of FELIX technology as a flexible and modular solution for DUNE, it was decided to use
2434 it to read out at least one APA in ProtoDUNE-SP as a proof of concept. A picture of the FELIX
2435 PCIe card is shown in Figure 82.

2436 The PDS electronics 4.3.5 is based on a Silicon Photomultiplier (SiPM) Signal Processor (SSP)
2437 prototype module, which is a high-speed waveform digitizer with 12 channels per module. Each
2438 channel contains a fully differential voltage amplifier and a 14-bit, 150 megasamples-per-second
2439 (MSPS) analogue-to-digital converter (ADC) with 2.1 Gbps data output. The timing is obtained by
2440 applying signal processing techniques to the leading edge of the SiPM signal, using the on-board
2441 Artix FPGA. It has deep data buffering (13), and operates with no dead-time up to 30 KHz per
2442 channel. A total of 24 SSPs serve to read out the PDS modules in all six APAs. The DAQ receives
2443 data from the SSPs over 24 1 Gb/s fibers: TCP/IP is used as communication protocol, thus the
2444 PDS readout is fully software-based from a DAQ point of view.

2445 For all readout systems, software-based applications called Board Readers read data from the
2446 TPC and PDS electronics to prepare event fragments corresponding to triggered time windows and
2447 send them to the event-building system. Within the event-building system, several applications
2448 run in parallel. The Routing Master application assigns a specific event builder to each trigger
2449 and distributes this information to the Board Readers. The Event Builders receive event fragments
2450 from the Board Readers, assemble them by timestamp into complete events, and store them into
2451 files, ready to be transferred to the offline computing. Another important function of the Routing
2452 Master is the handling of back-pressure from the downstream parts of the DAQ. If no event-builder
2453 application is ready to accept new events to build, the Routing Master informs the timing system,
2454 which starts vetoing triggers.



Figure 82: The FELIX BNL-711 PCIe card.

2455 **The DAQ software**

2456 The DAQ software depends in large part on existing solutions and frameworks. Its role is to manage
2457 and monitor the data-flow, and provide a run control service and online monitoring [45] processes.

2458 The primary responsibility of the DAQ data-flow software is to pack and transport the data
2459 from the detector electronics acquisition (WIB and SSPs) to the temporary storage on the DAQ
2460 transient store.

2461 This software is based on artdaq [46], a data acquisition toolkit developed at Fermilab. Use
2462 of artdaq also gives the software functionality to deliver configuration parameters to the front-end
2463 electronics and to perform a real-time monitoring of the data quality ($O(10)$ seconds) and of the
2464 DAQ system.

2465 The Run Control is based on the Joint COntrols Project (JCOP) [47] extension for the WinCC-
2466 OA supervisory control framework by Siemens[®]. It is in common use at the LHC experiments and
2467 is officially supported by CERN. The system provides a number of services: it provides the operator
2468 interface for launching, executing, and terminating DAQ applications, it is used for selecting the
2469 desired data-taking configuration, and it provides visualization of operational monitoring data and
2470 alerts the operator if any monitored values go out of range.

2471 **Towards the DUNE Far Detector**

2472 In addition to its being an important component for operating and validating the prototype as
2473 a whole, the ProtoDUNE-SP DAQ has served as a sandbox for validating data acquisition and
2474 triggering strategies for DUNE.

2475 The FELIX-based readout has been chosen as the baseline readout system for both the TPC
2476 and PDS in DUNE, and the ATCA-based RCE in ProtoDUNE-SP has now been replaced so that
2477 the TPC readout is all FELIX-based. The DUNE system will be enhanced, adding the capability to
2478 carry out some data processing in the firmware (e.g., the extraction of trigger primitives from the
2479 detector's data stream).

2480 The design of the timing system has also been confirmed. The hardware will be re-engineered
2481 for the DUNE far detector single phase module (DUNE-SP), retaining most of the features and the
2482 signalling protocol.

2483 Besides the scale of the system (ProtoDUNE-SP is 4% of one DUNE module) and the different
2484 requirements on resilience, fault tolerance, and DAQ uptime, the the ProtoDUNE-SP and DUNE-SP

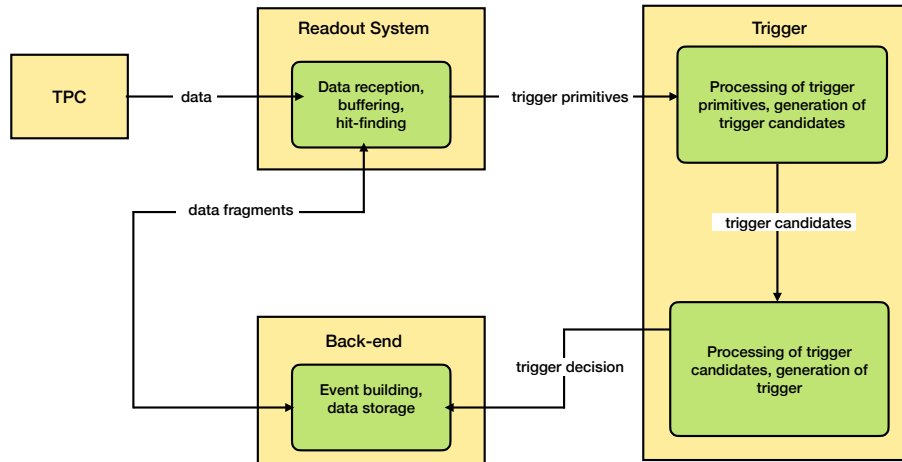


Figure 83: The flow of data in ProtoDUNE-SP in the self-triggering scenario.

2485 DAQs differ mainly in how they are triggered. In DUNE-SP, the activity in the TPC and PDS, rather
 2486 external signals, will provide the triggers. This requires that the DAQ be able to self-trigger based
 2487 on the data received from the TPC and the PDS.

2488 During the 2019 run, ProtoDUNE-SP achieved an important milestone demonstrating the
 2489 feasibility of the proposed trigger approach for DUNE-SP. In this approach, raw waveforms from
 2490 the TPC wires are sent to the FELIX system and buffered in the memory of high-end servers [48]. A
 2491 highly-optimised software runs on the CPUs of those servers and performs a hit-finding routine on
 2492 each of the 2560 wires of an APA. These hits, called “trigger primitives,” are then processed to form
 2493 “trigger candidates” for each APA. Trigger candidates are consumed in turn by the “module-level
 2494 trigger” that issues trigger commands for the whole detector, for ProtoDUNE-SP, all six APAs.

2495 Once a trigger is issued, the back-end system collects the data corresponding to a window
 2496 around the trigger timestamp and stores the data. The flow of data in the self-triggering scenario is
 2497 shown in Figure 83.

2498 A single server can handle data reception, buffering, and hit-finding for a complete APA. To
 2499 increase the capacity to two APAs in order to minimise space and power consumption for DUNE,
 2500 further software bench-marking and optimisations are ongoing. Using an FPGA for hit-finding and
 2501 trigger-primitive formation is also under study, as is the inclusion of PDS data into the self-triggering
 2502 chain.

2503 6.2 Detector Control System

2504 The ProtoDUNE-SP Detector Control System (DCS) (known historically as slow control) encom-
 2505 passes the hardware and software elements that ensure the safe and coherent operation of the
 2506 detector. The DCS monitors all the incoming signals from the detector and provides a uniform
 2507 interface for access and information exchange to all the detector subsystems. An alarm system
 2508 is configured to report any abnormal conditions to the operators. Depending on the severity of

2509 the alarm, the DCS can alert designated experts via email or SMS and take assisted or automatic
2510 corrective actions, e.g., if it detects a dangerous situation it can fire hardwired interlocks to protect
2511 the detector and its subsystems.

2512 Since ProtoDUNE-SP must thoroughly validate the detector design and performance, the DCS
2513 monitors and archives data for online and offline analysis at a much higher granularity and rate than
2514 would a conventional DCS system. It archives the sensor data as well as the power supply voltage,
2515 current, and temperature variations.

2516 **6.2.1 DCS Overview**

2517 The tight ProtoDUNE-SP schedule imposed a requirement that the DCS implement a proven and
2518 reliable solution. The commercial Supervisory Control And Data Acquisition (SCADA) WinCC-
2519 OA [49] from Siemens, widely used at CERN, was selected as the basis. The ProtoDUNE-SP DCS
2520 implements two CERN frameworks on top of WinCC-OA: the Joint Controls Project (JCOP) [50]
2521 and the Unified Industrial Control System (UNICOS) [51]. These frameworks provide guidelines,
2522 components, and tools designed to facilitate the implementation of a homogeneous control system.
2523 Their most salient features are:

- 2524 • automatic Programmable Logic Control (PLC) project generation;
- 2525 • a number of sets of predefined widget tools, faceplates, a Finite State Machine (FSM) toolkit,
2526 and a generic configurable Human Machine Interface (HMI);
- 2527 • an alarm and alert configuration system with automatic mail and SMS notifications, derived
2528 from the system used by the LHC experiments;
- 2529 • an access control component providing detailed authorisation schemes to assign specific
2530 privileges to different user groups;
- 2531 • a run-time database, accessible for processing, visualisation, etc., in which to store the data
2532 coming from the devices;
- 2533 • an archiver for long-term storage of the runtime database and offline use of that data;
- 2534 • a C-compatible scripting language with a very large library of functions that can be used to
2535 implement all WinCC-OA functionality;
- 2536 • standard libraries for commonly used hardware (e.g., CAEN and Wiener power supplies)
2537 that allow for centralised configuration of the implemented functions and parameters such as
2538 alarms, archiving parameters, operational values, and default panels, all at the crate, board,
2539 or channel level;
- 2540 • support of a wide range of drivers and communication protocols such as Siemens S7, MOD-
2541 BUS, OPC DA, OPC UA, the CERN Distributed Information (DIM)[52], and Data Inter-
2542 change Protocol (DIP)[53].

2543 To minimise the risk of unintended operator actions and maximise the stability of the system,
2544 the DCS interface presents panels that are designed to be as simple and straightforward as possible.
2545 The interface relies on standard color coding (see Figure 84) and is based on two main concepts:

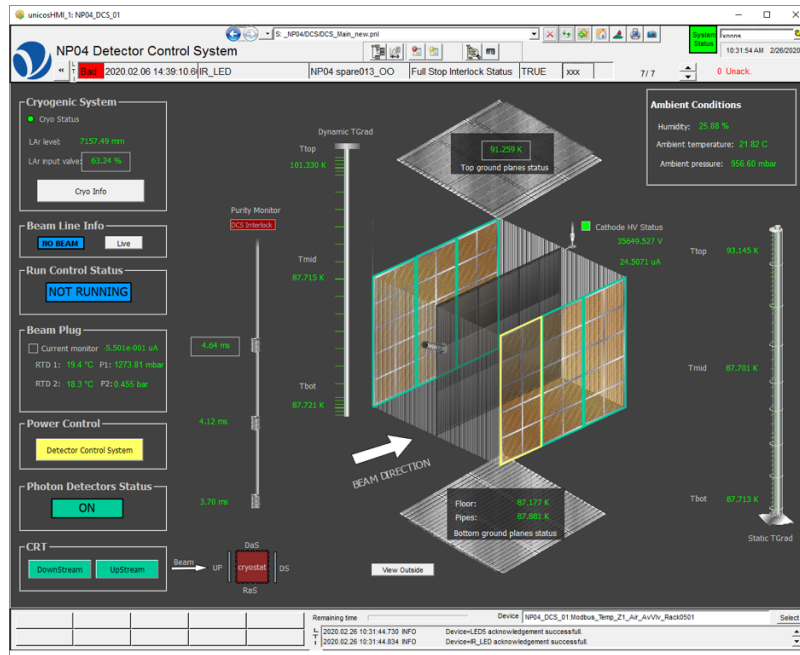


Figure 84: The DCS overview display, showing the color-coded status of the detector components, the average temperatures on the two T-gradient rods, and the most recent electron lifetime measurements.

- 2546 • dynamic graphical objects that allow the operator to navigate to dedicated panels for each
2547 detector subsystem, and
- 2548 • data widgets, objects displayed as data values that allow operations to be performed on them,
2549 such as plotting historical values or checking status.

2550 For basic control operations, the DCS uses the Finite State Machine (FSM) component from
2551 JCOP [54]. The FSM acts as an abstraction layer that simplifies control of the detector. Based on a
2552 well defined set of states and transitions, each part of the detector can be controlled hierarchically.
2553 Once the topology of the detector is defined, the FSM component is responsible for propagating
2554 the actions sent to the different parts of the detector and obtaining, as a result of these actions or
2555 asynchronous incidents, their corresponding states. An example of the FSM used for the detector
2556 power control is shown in Figure 85. Access Control, implemented in the FSM, ensures the safe
2557 operation of the detector.

2558 For advanced detector operations, specific and more detailed panels have been designed. Rather
2559 than using an FSM for putting the detector – or any of its components – in a preset state, the advanced
2560 panels allow users with appropriate authorisation full control over all parts of the detector. The
2561 advanced panels control the lowest-level architecture of the detector, allowing the authorised experts
2562 to modify operational parameters, load pre-set configurations from files, set limits for alerts, and/or
2563 directly control critical devices beyond the scope of the FSM.

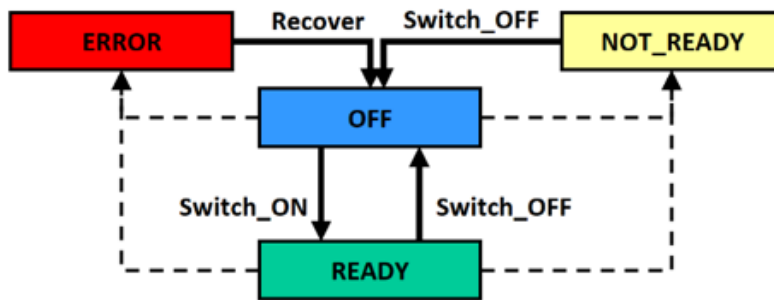


Figure 85: FSM flow diagram for turning ON/OFF a detector component.

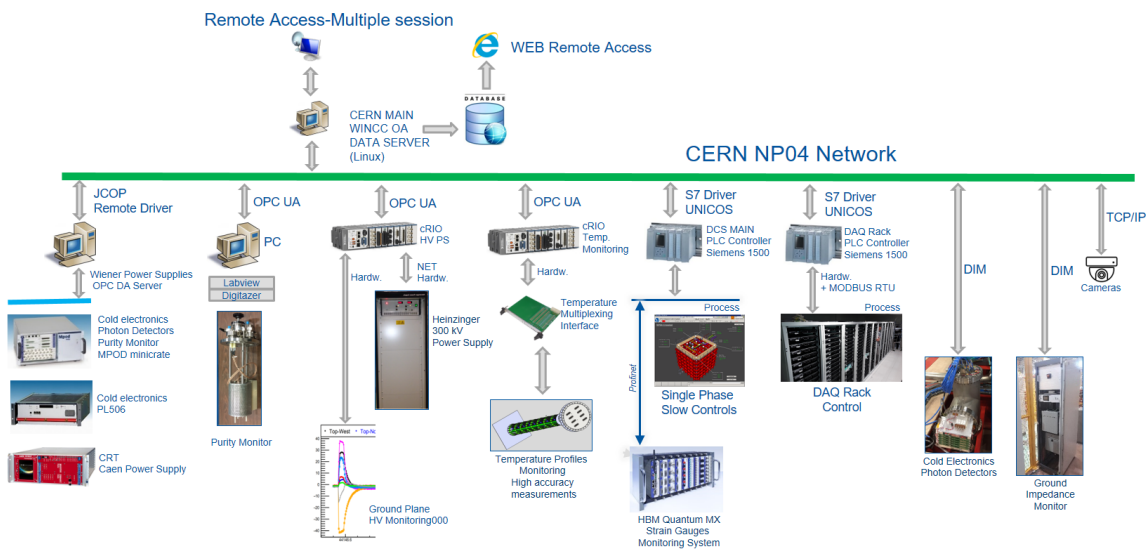


Figure 86: DCS architecture and communication protocols.

2564 6.2.2 DCS Architecture

2565 The DCS subsystems are connected to a dedicated ProtoDUNE-SP detector network, known as
 2566 the NP04 network. The DCS can communicate with the individual subsystems using a variety
 2567 of communication protocols, indicated by the white arrows in Figure 86. Furthermore, the DCS
 2568 is accessible over the Internet using a remote connection protocol, and the most relevant data are
 2569 published to a web server for real-time off-site monitoring. A brief description of the different
 2570 subsystems, and how the DCS manages them, is given below.

- 2571 • *The Detector Power Control (DPC)*: The DPC is a set of power supplies that provide power
 2572 to the different parts of the detector, including the cold electronics, the PDS, the HV for the
 2573 field cage, and the CRT. These power supplies are connected to the main DCS application by
 2574 means of the OPC DA driver [55]. The JCOP mass configuration tool is used to set all the
 2575 power supply parameters, e.g., operating values, addresses, and archiving parameters, and to
 2576 populate the default control panels.

- 2577 • *TPC cold electronics (CE)*: To assess their status, the DCS continuously monitors the main
2578 parameters of the CE crates, WIBs, and FEMBs through the detector network by means of
2579 the DIM protocol. A hardware interlock between the CE cooling fans and the CE low-voltage
2580 power is in place to prevent powering on of the CE in case of fan failure.

 - 2581 • *Photon Detector system (PDS)*: The DCS provides an interface with the PDS for monitoring its
2582 working conditions and tuning its configuration for accurate operation. These configurations
2583 can be stored in a file and imported by the DCS. The interface is based on the DIM protocol.
2584 Critical interlocks have been implemented in the DCS to prevent any potential damage to the
2585 PDS when the purity monitors' xenon lamp flashes or the cryostat LEDs are turned on.

 - 2586 • *HV system*: The DCS for the HV system is composed of two tightly correlated components:
2587 the controls of the Heinzinger power supply [56] that provides HV to the TPC cathode, and the
2588 current monitors on the ground planes and beam plug. A dedicated National Instruments cRIO
2589 FPGA [57] performs the HV control process through a high-resolution analogue interface.
2590 A novel feature, called Recovery Mode, was developed to resolve streamer events (extended
2591 discharges, see Section 4.1.4), which are characterised by high current draw. Recovery mode
2592 automatically lowers the HV setpoint while continuously monitoring the current draw at the
2593 power supply until the current draw is below the current limit. It then restores the HV setpoint
2594 to its nominal value.
- 2595 An example of an automatic streamer recovery is given in Figure 26. The current signals
2596 from the 12 ground planes and the beam plug are connected to the same HV control system.
2597 In the case of a 'stream' or discharge event, the DCS records the main HV parameters at 20
2598 kHz for 5 seconds with a pre-trigger of one second into a fast-acquisition file that it sends to
2599 the DAQ system for off-line analysis.
- 2600 • *Purity monitors*: The purity monitor system is controlled locally by a PCIe Alazartech
2601 ATS310 digitiser installed in a computer dedicated to this task. The local user interface
2602 was developed in LabVIEW software, which includes an OPC UA server, communicating
2603 with the main DCS as a client. The DCS provides a dedicated user panel for monitoring
2604 its status and setting the configuration for operation. The DCS can select different internal
2605 digitiser working modes and choose the appropriate HV configuration. Once configured,
2606 the DCS supports automatically running the purity monitor DAQ with one click, after which
2607 it displays all the relevant information. As previously mentioned, to protect the PDS, the
2608 DCS implements an interlock system to prevent the purity monitors from operating during
2609 data-taking runs.

 - 2610 • *Gradient Temperature sensors*: Temperature sensors (PT100) are installed in the ProtoDUNE-
2611 SP cryostat to monitor the temperature gradient of the liquid with high precision ($\sim 2\text{mK}$)
2612 (see Section 4.5.2). A customised electronic interface developed by the collaboration is
2613 connected to a National Instruments cRIO FPGA that publishes all temperature values to the
2614 main DCS database through an OPC UA server. The same interface controls the position of
2615 the dynamic gradient sensor. The data stored in the database is used for off-line calculations
2616 and simulations. The DCS also publishes the maximum and minimum temperatures of

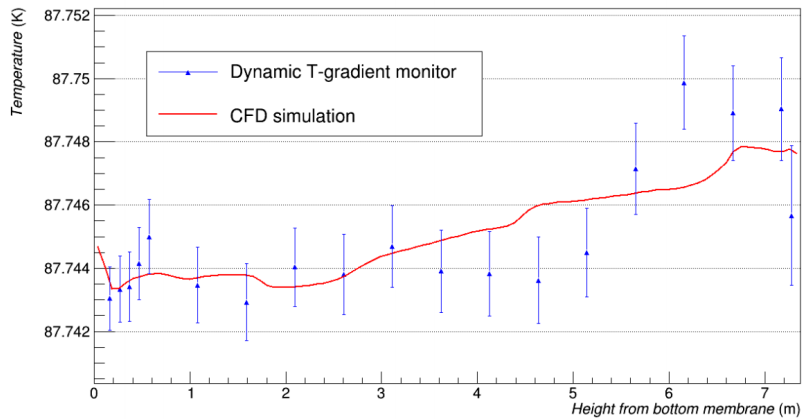


Figure 87: Temperature measurement and predicted value as a function of the height of cryostat.

2617 the static gradient via DIP; these are used by the cryogenics system for alarm reporting.
 2618 Figure 87 shows an example of a liquid argon temperature measurement taken during standard
 2619 operations. A comparison with the predicted values from the Computational Fluid Dynamics
 2620 (CFD) simulation is also shown.

2621 • *Ground Impedance Monitor:* As described in Section 5.4 the detector ground is isolated
 2622 from the building ground, and the DCS monitors the ground decoupling through a Ground
 2623 Impedance Monitor (Zmon). This device is connected to the main DCS by means of a DIM
 2624 protocol. If a grounding problem is detected, the ground impedance monitor sounds an alarm.
 2625 The DCS alerts operators and records incoming data.

2626 • *Multi-purpose PLC:* A S7-1500 Siemens PLC connected to the main DCS application by
 2627 means of the S7 driver[58] performs several tasks using the CERN UNICOS framework:

- 2628 – controls and monitors the electrical network and ambient parameters (temperature,
 2629 atmospheric pressure, humidity);
- 2630 – performs the interlock logic of the CE LV power supply according to the cooling crate
 2631 status;
- 2632 – reads the relative and absolute pressures inside the cryostat;
- 2633 – performs the control and interlock logic of the LED light installed inside the cryostat;
- 2634 – operates the cameras and the associated heaters;
- 2635 – controls heaters on the CE and PDS flanges to dry out water condensation; and
- 2636 – ensures the connection to the HBM system that reads the cryostat instrumentation gauges
 2637 (see Section 3.2.2) and publishes the values for each sensor to the DCS.

2638 • *DAQ environment control:* Monitoring the racks where the DAQ system is installed is also
 2639 critical for ensuring the correct recording of the ProtoDUNE-SP data. One Siemens S7-1500
 2640 PLC controls and supervises the environmental conditions and the main electrical and cooling

parameters. In case of a fault, this PLC turns off all DAQ rack power to avoid overheating. A second Siemens S7-1500 PLC is connected to all internal DAQ rack door controls by means of a MODBUS network that acquires the individual rack door statuses and configuration parameters. Both PLCs are integrated in the main DCS through a Siemens S7 driver. They were developed using the CERN UNICOS framework.

- *Cryogenics system:* The DCS and cryogenics systems continuously exchange information; any incorrect cryogenic condition may affect the detector's operation. As the cryogenics control system is installed in a different network, the data exchange is performed by means of a DIP protocol that only allows data subscription by an external system.

7 Conclusions

The ProtoDUNE-SP detector with a total LAr mass of 0.77 kt is the largest LArTPC operated to date. In the span of five years, from the time of approval in June 2015 to the end of data taking in July 2020, DUNE collaborators designed, constructed, commissioned, and operated ProtoDUNE-SP. In successfully validating the technologies planned for DUNE-SP, developing the logistics and installation procedures that will be needed, demonstrating operational stability, developing calibration strategies and techniques, and establishing operational parameters, DUNE has reached every goal it set forth for this prototype detector, an experiment in its own right.

The ProtoDUNE-SP cryostat implements for the first time in a 1 kt scale detector, a technology previously used only in liquid cryogen industrial settings and transport, known as membrane technology. The membrane cryostat was assembled with no problems and it was validated through several test campaigns. A sophisticated cryogenics and purification infrastructure ensured successful operation at the desired temperature and pressure. The flexibility of the system allowed for the implementation of alternative solutions during detector operations when needed while still ensuring the same high-quality LAr and control of the various detector operation stages. Each of the full-scale detector components underwent a rigorous process of design, manufacture, quality assurance, handling, packaging, transport, assembly, and installation. This experience has provided valuable input for optimising these procedures for the first DUNE single phase far detector module. In addition to the detector components immersed in the LAr, the detector readout and control system demonstrated excellent performance.

The DUNE collaboration gained immeasurable experience with each of the detector components during the period of ProtoDUNE-SP operations. The same is true for the CERN and LBNF team that provided the cryogenics infrastructure. Beyond its role in validating designs, procedures, and strategies planned for DUNE-SP, ProtoDUNE-SP provided an excellent test stand for additional large-scale detector R&D, e.g., doping the LAr with xenon, which will allow for further improvements in LArTPC technology.

In summary, ProtoDUNE-SP has successfully implemented this mature LArTPC technology in a scalable design, demonstrating its suitability for an APA-based single-phase DUNE far detector module. Its completion in the extremely tight schedule attests to the efficiency and reliability of the design and construction techniques. ProtoDUNE-SP data exhibits superb detector performance and signal-to-noise ratio, as described in the ProtoDUNE-SP performance paper [3]. The achievement

2681 of ProtoDUNE-SP represents a major milestone for DUNE. Further, the knowledge obtained and
2682 processes developed during its design, construction, and operation are sure to carry forward well
2683 beyond this experiment, benefiting other future experiments as well.

2684 **Acknowledgements**

2685 The ProtoDUNE-SP detector was constructed and operated on the CERN Neutrino Platform.
2686 We gratefully acknowledge the support of the CERN management, and the CERN EP, BE, TE,
2687 EN and IT Departments for NP04/ProtoDUNE-SP. This document was prepared by the DUNE
2688 collaboration using the resources of the Fermi National Accelerator Laboratory (Fermilab), a U.S.
2689 Department of Energy, Office of Science, HEP User Facility. Fermilab is managed by Fermi
2690 Research Alliance, LLC (FRA), acting under Contract No. DE-AC02-07CH11359. This work was
2691 supported by CNPq, FAPERJ, FAPEG and FAPESP, Brazil; CFI, IPP and NSERC, Canada; CERN;
2692 MŠMT, Czech Republic; ERDF, H2020-EU and MSCA, European Union; CNRS/IN2P3 and CEA,
2693 France; INFN, Italy; FCT, Portugal; NRF, South Korea; CAM, Fundación “La Caixa”, Junta de
2694 Andalucía-FEDER, and MICINN, Spain; SERI and SNSF, Switzerland; TÜBİTAK, Turkey; The
2695 Royal Society and UKRI/STFC, United Kingdom; DOE and NSF, United States of America. This
2696 research used resources of the National Energy Research Scientific Computing Center (NERSC), a
2697 U.S. Department of Energy Office of Science User Facility operated under Contract No. DE-AC02-
2698 05CH11231.

2699 References

- 2700 [1] DUNE collaboration, B. Abi et al., *Proposal for a Full-Scale Prototype Single-Phase Liquid Argon*
2701 *Time Projection Chamber and Detector Beam Test at CERN*, Tech. Rep. CERN-SPSC-2015-020.
2702 SPSC-P-351, CERN, Geneva, 2015.
- 2703 [2] DUNE collaboration, B. Abi et al., *The Single-Phase ProtoDUNE Technical Design Report*,
2704 [[1706.07081](#)].
- 2705 [3] DUNE collaboration, B. Abi et al., *First Results on ProtoDUNE-SP Liquid Argon Time Projection*
2706 *Chamber Performance from a Beam Test at the CERN Neutrino Platform*, *JINST* **15** (2020) P12004,
2707 [[2007.06722](#)].
- 2708 [4] *The European Strategy for Particle Physics Update 2013*, Tech. Rep. CERN-Council-S-0106, CERN,
2709 Geneva, 2013.
- 2710 [5] N. Charitonidis and I. Efthymiopoulos, *Low energy tertiary beam line design for the cern neutrino*
2711 *platform project*, *Phys. Rev. Accel. Beams* **20** (2017) 111001.
- 2712 [6] A. C. Booth, N. Charitonidis, P. Chatzidaki, Y. Karyotakis, E. Nowak, I. Ortega-Ruiz et al., *Particle*
2713 *production, transport, and identification in the regime of 1–7 GeV*, *Phys. Rev. Accel. Beams* **22**
2714 (2019) 061003.
- 2715 [7] J. Calcutt, *Measurement of Argon Absorption and Charge Exchange Interactions using*
2716 *ProtoDUNE-SP*. PhD thesis, Michigan State University (US), 2021. [Thesis in preparation].
- 2717 [8] BSI Corporate, “BS EN 10025-4:2004 Hot rolled products of structural steels..”
2718 <https://shop.bsigroup.com/ProductDetail?pid=000000000030027418>.
- 2719 [9] Gaztransport & Technigaz SA (GTT), “GTT membrane technologies.”
2720 <https://www.gtt-training.co.uk/gtt-membrane-technologies>.
- 2721 [10] The European Union, “European standard for design of steel structures.”
2722 <https://www.phd.eng.br/wp-content/uploads/2015/12/en.1993.1.4.2006.pdf>.
- 2723 [11] National Instruments, “Measuring strain with strain gages - white paper.” [https://www.ni.com/](https://www.ni.com/fr-fr/innovations/white-papers/07/measuring-strain-with-strain-gages.html)
2724 [fr-fr/innovations/white-papers/07/measuring-strain-with-strain-gages.html](https://www.ni.com/fr-fr/innovations/white-papers/07/measuring-strain-with-strain-gages.html).
- 2725 [12] M. Adamowski, B. Carls, E. Dvorak, A. Hahn, W. Jaskierny, C. Johnson et al., *The liquid argon purity*
2726 *demonstrator*, *JINST* **9** (2014) P07005–P07005.
- 2727 [13] M. Pezzetti, C. Fluder and R. Orlandi, *CERN Neutrino Cryogenic Control System Technology: From*
2728 *the WA105 Test Facility to the NP04 and NP02 Platforms.*, in *ICALEPCS’19*, no. 17 in International
2729 Conference on Accelerator and Large Experimental Physics Control Systems, pp. 1209–1213, JACoW
2730 Publishing, Geneva, Switzerland, 2020. 10.18429/JACoW-ICALEPCS2019-WEPHA049.
- 2731 [14] UNICOS-CPC, “UNICOS Continuous Process Control.”
2732 <https://readthedocs.web.cern.ch/display/UCPC15/UNICOS-CPC>.
- 2733 [15] DuPont Specialty Products USA, LLC, “D11261075 Kapton polyimide film 100XC10E7.”
2734 [https://www.dupont.com/content/dam/dupont/amer/us/en/products/](https://www.dupont.com/content/dam/dupont/amer/us/en/products/ei-transformation/documents/EI-10142-Kapton-Summary-of-Properties.pdf)
2735 [ei-transformation/documents/EI-10142-Kapton-Summary-of-Properties.pdf](https://www.dupont.com/content/dam/dupont/amer/us/en/products/ei-transformation/documents/EI-10142-Kapton-Summary-of-Properties.pdf), 2017.
- 2736 [16] ICARUS collaboration, S. Amerio et al., *Design, Construction and Tests of the ICARUS T600*
2737 *Detector*, *Nucl. Instrum. Meth.* **A527** (2004) 329–410.
- 2738 [17] F. A. Stocker, *Measurement of the Pion Absorption Cross Section with the ProtoDUNE Experiment*.
2739 PhD thesis, University of Bern (CH), 2021. [Thesis in preparation].

- 2740 [18] K. R. Wood, *A Bayesian Analysis of T2K's Data from 3.6 $\times 10^{21}$ POT for the Measurement of Neutrino*
2741 *Oscillation Parameters*. PhD thesis, Stony Brook University (US), 2021. [Thesis in preparation].
- 2742 [19] C. Bromberg, B. Carls, D. Edmunds, A. Hahn, W. Jaskierny, H. Jostlein et al., *Design and operation*
2743 *of LongBo: a 2 m long drift liquid argon TPC*, *JINST* **10** (2015) P07015–P07015.
- 2744 [20] M. Babicz et al., *Experimental Study of the Propagation of Scintillation Light in Liquid Argon*, *Nucl.*
2745 *Instrum. Meth.* **936** (2019) 178–179.
- 2746 [21] M. Babicz et al., *A measurement of the Group Velocity of Scintillation Light in Liquid Argon*, *JINST*
2747 **15** (2020) P09009, [2002.09346].
- 2748 [22] T. Heindl, T. Dandl, A. Fedenev et al., *Table-top setup for investigating the scintillation properties of*
2749 *liquid argon*, *Journal of Instrumentation* **6** (2011) P02011, [1511.07720].
- 2750 [23] Z. Moss, J. Moon, L. Bugel, J. Conrad, K. Sachdev, M. Touns et al., *A Factor of Four Increase in*
2751 *Attenuation Length of Dipped Lightguides for Liquid Argon TPCs Through Improved Coating*,
2752 [1604.03103].
- 2753 [24] B. Howard, S. Mufson, D. Whittington, B. Adams, B. Baugh, J. Jordan et al., *A Novel Use of Light*
2754 *Guides and Wavelength Shifting Plates for the Detection of Scintillation Photons in Large Liquid*
2755 *Argon Detectors*, *Nucl. Instrum. Meth.* **907** (2018) 9–21, [1710.11233].
- 2756 [25] B. L. Howard Jr., *Toward A Precision Era Of Neutrino Oscillation Physics: Liquid Argon*
2757 *Scintillation Detector Development for DUNE and Neutrino Oscillation Studies with NOvA*. PhD
2758 thesis, Indiana University (US), 2019. 10.2172/1599305.
- 2759 [26] C. T. Macias, *Scintillation Photon Detection in a Large-Volume Liquid Argon Time Projection*
2760 *Chamber Exposed to a Multi-GeV Charged Particle Beam*. PhD thesis, Indiana University (US),
2761 2021. [Thesis in preparation].
- 2762 [27] A. Machado and E. Segreto, *ARAPUCA a new device for liquid argon scintillation light detection*,
2763 *JINST* **11** (2016) C02004–C02004.
- 2764 [28] E. Segreto et al., *Liquid Argon Test of the ARAPUCA Device*, *JINST* **13** (2018) P08021,
2765 [1805.00382].
- 2766 [29] THE DOUBLE CHOOZ collaboration, Y. Abe, J. C. dos Anjos et al., *Improved measurements of the*
2767 *neutrino mixing angle θ_{13} with the double chooz detector*, *Journal of High Energy Physics* **2014** (Oct,
2768 2014) 86.
- 2769 [30] A. Bettini, A. Braggiotti, F. Casagrande, P. Casoli, P. Cennini, S. Centro et al., *A study of the factors*
2770 *affecting the electron lifetime in ultra-pure liquid argon*, *Nuclear Instruments and Methods in Physics*
2771 *Research Section A: Accelerators, Spectrometers, Detectors and Associated Equipment* **305** (1991)
2772 177–186.
- 2773 [31] R. Diurba, *Evaluating the ProtoDUNE-SP Detector Performance to Measure a 6 GeV Kaon Inelastic*
2774 *Cross Section on Argon*. PhD thesis, University of Minnesota (US), 2021. [Thesis in preparation].
- 2775 [32] G. Chambers-Wall, “Charge Response and Energy Calibration of ProtoDUNE-SP.”
2776 <https://indico.fnal.gov/event/23109/contributions/193490>, 2020.
- 2777 [33] D. M. et al., *Performance and results of the lbne 35 ton membrane cryostat prototype*, *Physics*
2778 *Procedia* **67** (2015) 308–313.
- 2779 [34] M. A. Garcia-Peris, *ProtoDUNE T-Gradient Development and Calibration*, Master's thesis,
2780 University of Valencia (ES), 2018. 10.2172/1780813.

- 2781 [35] Delaquis, S. C. and Gornea, R. and Janos, S. and Lüthi, M. and Rudolf von Rohr, C. and Schenk, M.
2782 and Vuilleumier, J. -L., *Development of a Camera Casing Suited for Cryogenic and Vacuum*
2783 *Applications*, *JINST* **8** (2013) T12001, [[1310.6601](#)].
- 2784 [36] Auger, M. and Blatter, A. and Ereditato, A. and Goeldi, D. and Janos, S. and Kreslo, I. and Lüthi, M.
2785 and Rudolf von Rohr, C. and Strauss, T. and Weber, M. S., *On the Electric Breakdown in Liquid*
2786 *Argon at Centimeter Scale*, *JINST* **11** (2016) P03017, [[1512.05968](#)].
- 2787 [37] “LUXEON C Color Line (datasheet).” <https://www.lumileds.com/uploads/571/DS144-pdf>.
- 2788 [38] D. Adams, M. Bass, M. Bishai, C. Bromberg, J. Calcutt, H. Chen, J. Fried, I. Furic, S. Gao, D.
2789 Gastler, J. Hugon, J. Joshi, B. Kirby, F. Liu, K. Mahn, M. Mooney, C. Morris, C. Pereyra, X. Pons, V.
2790 Radeka, E. Raguzin, D. Shooltz, M. Spanu, A. Timilsina, S. Tufanli, M. Tzanov, B. Viren, W. Gu, Z.
2791 Williams, K. Wood, E. Worcester, M. Worcester, G. Yang, J. Zhan, *The ProtoDUNE-SP LArTPC*
2792 *Electronics Production, Commissioning, and Performance*, *JINST* **15** (2020) P06017, [[2002.01782](#)].
- 2793 [39] A. Peters, E. Sindrilaru and G. Adde, *EOS as the present and future solution for data storage at*
2794 *CERN*, *Journal of Physics: Conference Series* **664** (2015) 042042.
- 2795 [40] R. Herbst, R. Claus, M. Freytag, G. Haller, M. Huffer, S. Maldonado et al., *Design of the slac rce*
2796 *platform: A general purpose atca based data acquisition system*, in *IEEE Nuclear Science Symposium*
2797 *and Medical Imaging Conference (NSS/MIC)*, pp. 1–4, 2014. 10.1109/NSSMIC.2014.7431254.
- 2798 [41] D. Adams, M. Baird, G. Barr, N. Barros, A. Blake, E. Blaufuss et al., *Design and performance of a*
2799 *35-ton liquid argon time projection chamber as a prototype for future very large detectors*, *JINST* **15**
2800 (2020) P03035–P03035.
- 2801 [42] K. V. Tsang, M. Convery, M. Graham, R. Herbst and J. Russell, *The SLAC RCE Platform for*
2802 *ProtoDUNE*, in *European Physical Journal Web of Conferences*, vol. 214 of *European Physical*
2803 *Journal Web of Conferences*, 2019. 10.1051/epjconf/201921401025.
- 2804 [43] J. Anderson, K. Bauer, A. Borga, H. Boterenbrood, H. Chen, K. Chen et al., *FELIX: a PCIe based*
2805 *high-throughput approach for interfacing front-end and trigger electronics in the ATLAS upgrade*
2806 *framework*, *JINST* **11** (2016) C12023–C12023.
- 2807 [44] Intel, “Intel QuickAssist Technology (Intel QAT) and OpenSSL-1.1.0: Performance - White paper.”
2808 [https://01.org/sites/default/files/downloads/intelr-quickassist-technology/](https://01.org/sites/default/files/downloads/intelr-quickassist-technology/337003-001-intelquickassisttechnologyandopenssl-110.pdf)
2809 [337003-001-intelquickassisttechnologyandopenssl-110.pdf](https://01.org/sites/default/files/downloads/intelr-quickassist-technology/337003-001-intelquickassisttechnologyandopenssl-110.pdf).
- 2810 [45] A. Reynolds, *Evaluating the low-energy response of the ProtoDUNE-SP detector using Michel*
2811 *electrons*. PhD thesis, University of Oxford (UK), 2020.
- 2812 [46] K. Biery, C. Green, J. Kowalkowski, M. Paterno and R. Rechenmacher, *artdaq: An Event-Building,*
2813 *Filtering, and Processing Framework*, *IEEE Trans. Nucl. Sci.* **60** (2013) 3764 – 3771.
- 2814 [47] CERN, “The Joint COntrols Project (JCOP) framework.” <https://jcop.web.cern.ch>.
- 2815 [48] M. A. Vermeulen, *A Blessing in Disguise: Characterisations of ProtoDUNE photon showers for*
2816 *neutrino measurements in DUNE*. PhD thesis, NIKHEF (NL), 2021. [Thesis in preparation].
- 2817 [49] Siemens AG, “SIMATIC WinCC Open Architecture.”
2818 <http://www.siemens.com/wincc-open-architecture>.
- 2819 [50] O. Holme, S. Schmeling, M. González-Berges and P. Golonka, *The JCOP Framework*, tech. rep.,
2820 CERN, Geneva, 2005.
- 2821 [51] H. Milcent, E. Blanco, F. Bernard and P. Gayet, *UNICOS: An open framework*, in *ICALEPCS*

- 2822 (<https://accelconf.web.cern.ch/icalepcs2009/papers/thd003.pdf>, ed.), p. THD003,
2823 2009.
- 2824 [52] C. Gaspar, M. Dönszelmann and P. Charpentier, *DIM, a Portable, Light Weight Package for*
2825 *Information Publishing, Data Transfer and Inter-process Communication*, *Computer Physics*
2826 *Communications* **140** (2001) 102–109.
- 2827 [53] B. Copy, I. Prieto Barreiro, F. Varela and E. Mandilara, *Monitoring of CERN’s Data Interchange*
2828 *Protocol (DIP) system*, 2018. 10.18429/JACOW-ICALEPCS2017-THPHA162.
- 2829 [54] C. Gaspar and B. Franek, *Tools for the Automation of Large Distributed Control Systems*, *IEEE*
2830 *Transactions on Nuclear Science* **53** (2006) 974–979.
- 2831 [55] OPC Foundation, “OPC Classic specifications.”
2832 <https://opcfoundation.org/about/opc-technologies/opc-classic/>.
- 2833 [56] Heinzinger electronic GmbH, “Heinzinger.” <https://www.heinzinger.com/>.
- 2834 [57] National Instruments, “CompactRIO Systems.”
2835 <http://www.ni.com/en-us/shop/compactrio.html>.
- 2836 [58] Siemens AG, “SIMATIC Controllers - Industrial Automation Systems.” [https://www.siemens.](https://www.siemens.com/global/en/home/products/automation/systems/industrial/plc.html)
2837 [com/global/en/home/products/automation/systems/industrial/plc.html](https://www.siemens.com/global/en/home/products/automation/systems/industrial/plc.html).